Recent progress on the additive manufacturing of aluminum alloys and aluminum matrix composites: microstructure, properties, and applications

Zhiguang Zhu[a,b,*], Zhiheng Hu[a], Hang Li Seet[a], Tingting Liu[b], Wenhe Liao[b], Upadrasta Ramamurty[c,d], Sharon Mui Ling Nai[a,**]

[a] Singapore Institute of Manufacturing Technology (SIMTech), Agency for Science, Technology and Research (A*STAR), 5 Cleantech Loop, 636732, Singapore

[b] School of Mechanical Engineering, Nanjing University of Science and Technology, Nanjing 210094, PR China

[c] School of Mechanical and Aerospace Engineering, Nanyang Technological University, Singapore, Singapore

[d] Institute of Materials Research and Engineering, Agency for Science, Technology and Research (A*STAR), Singapore, Singapore

* Corresponding author.

** Corresponding author.

E-mail address: zhuzg@njust.edu.cn (Zhiguang Zhu), hu_zhiheng@simtech.a-star.edu.sg (Zhiheng Hu), liutingting@mail.njust.edu.cn (Tingting Liu), cnwho@mail.njust.edu.cn (Wenhe Liao), uram@ntu.edu.sg (Upadrasta Ramamurty), seet_hang_li@simtech.a-star.edu.sg (Hang Li Seet), mlnai@simtech.a-star.edu.sg (Sharon Mui Ling Nai)

Abstract

Whilst the adoption of additive manufacturing (AM) of aluminum alloys is relatively slower compared with that of steels and titanium alloys, it has undergone a flourishing trend in the past 15 years. Significant progress, such as the development of novel processes, novel alloys, novel heat treatment profiles, and applications, has been made through the combined efforts from academic and industry fields. This state-of-the-art review presents a detailed overview of the process technology, microstructure, and properties of different aluminum alloys and aluminum matrix composites fabricated using various additive manufacturing technologies, including laser powder bed fusion, electron beam powder bed fusion, laser powder direct energy deposition, wire arc additive manufacturing, binder jetting, and additive friction stir deposition. The pros and cons of each technology in fabricating aluminum alloys are evaluated. As the dominant additive manufacturing technology for aluminum alloys, an emphasis is put on the laser powder bed fusion technology by reviewing the effect of various factors, such as post-heat treatment, powder feedstock, oxidation, and element evaporation, on the microstructure and properties. We close the review with the outlook listing the remaining challenges associated with the additive manufacturing of aluminum alloys.

Keywords: Additive manufacturing; Aluminum alloys; Aluminum matrix composite; Microstructure; Mechanical property; Applications.

Abbreviations

3D	Three-Dimensional	**ILB**	Inter Layer Boundary
AA	Artificial Aging	**IPF**	Inverse Pole Figure
AFSD	Additive Friction Stir Deposition	**LC**	Laser Cladding
AM	Additive Manufacturing	**LP-DED**	Laser Powder Direct Energy Deposition
APT	Atom Probe Tomography		
BD	Build Direction	**L-PBF**	Laser Powder Bed Fusion
BJ	Binder Jetting	**LOC**	Low Oxygen Concentration
BSE	Backscattered Electron	**ME**	Metal Extrusion
CAD	Computer-Aided Design	**PB-EBM**	Powder Bed Electron Beam Melting
COD	Crack Opening Displacement		
CS	Cold Spray	**PBF**	Powder Bed Fusion
CTE	Columnar To Equiaxed	**PSD**	Particle Size Distribution
DA	Direct Aging	**SEM**	Scanning Electron Microscope
EBFF	Electron Beam Freeform Fabrication	**S-N**	Stress Range-Endurance curve
		SP	Screen or Stencil Printing
EB-PBF	Electron Beam Powder Bed Fusion	**ST**	Solution Treatment
		STA	Solution Treatment and Aging
EBSD	Electron Backscattered Diffraction	**STEM**	Scanning Transmission Electron Microscopy
EDS	Energy Dispersive Spectrum	**TEM**	Transmission Electron Microscope
ETC	Equiaxed To Columnar		
FCC	Face-Centered Cubic	**TWI**	The Welding Institute
FFT	Fast Fourier Transform	**UAM**	Ultrasonic Additive Manufacturing
FSW	Friction Stir Welding		
GBS	Grain Boundary Sliding	**VED**	Volume Energy Density
GRF	Grain Growth Factor	σ_{UTS}	Ultimate Tensile Strength
HAADF	High Angle Annular Dark Field	**WAAM**	Wire Arc Additive Manufacturing
HCF	High Cycle Fatigue		
HIP	Hot Isostatic Pressing	**WEBM**	Wire Electron Beam Melting
HOC	High Oxygen Concentration	**WLAM**	Wire Laser Additive Manufacturing
HRTEM	High-Resolution Transmission Electron Microscope		
		σ_y	Yield Strength
HT	Heat Treatable or Heat Treatment	ε_f	Elongation To Fracture

1. Introduction

Additive manufacturing (AM) technology can be utilized to incrementally construct, layer-by-layer, the three-dimensional (3D) parts controlled by a computer-aided design (CAD) file [1]. Since its inception, AM is widely regarded as a new paradigm for producing high-performance structural components thanks to the fabrication advantages it offers, such as near-net-shape forming, design freedom, shorter lead times, lower buy-to-fly ratio, and minimum post-processing steps [1]. As a result, it promises to redefine the manufacturing industry with broad application potential in the aerospace fields [2]. Consequently, it attracts considerable interest, as evidenced by the increasing number of publications on AM during the last 15 years [3-6]. The metallic AM process can be regarded as a multiple-welding process, and thus, the procedures used during welding may also be applied for it [7]. Similar to the welding process, these technologies can be divided into melt-based AM and solid-state AM, depending on whether the feedstock materials undergo melting during joining of the adjacent layers [8]. For melt-based AM, the feedstock materials experience melting and solidification with the heat sources provided either by a laser beam, an electron beam, or an arc. Comparatively, solid-state-based AM joins the adjacent layers through sintering or mechanical bonding. The detailed classification of these two categories of AM methods will be described in *Section 2*.

As the second most used structural alloys after steels, aluminum (Al) alloys have played a significant role in the aerospace industry, the initial adopter of AM technology, due to their low density and excellent combination of properties [9,10]. Up to now, both melt-based and solid-state AM technologies have been employed to fabricate Al alloys. As for the melt-based AM technology, the adoption of Al alloys is relatively slow due to the following perspectives: (1) Al alloys are easy to cast into complex-shaped components via conventional casting or produced using wrought methods, unlike Ti alloys and nickel-based superalloys, which are associated with poor formability [11];

(2) the inherent disadvantages of Al powders, such as the formation of surface oxide, poor spreadability, and moisture absorption make them ill-matched for melt-based AM [11,12]; (3) the poor weldability for some high-strength Al alloys makes them not ideally suited for melt-based AM, as hot cracks form during AM [10]. Taking the typical melt-based AM technology, laser powder bed fusion (L-PBF), for example, the number of publications on Al alloys is fewer compared with those on Ti alloys and steels [13].The total publications on L-PBF steels, Ti alloys, and Al alloys are 1305, 1154, and 822, respectively, from 2009 to 2019 [13]. For sintering-based solid-state AM, the processing of Al alloys is challenging since a controlled atmosphere with low oxygen and vapour partial pressure is needed for preventing oxidation and enhancing the atomic diffusion during sintering [8]. Comparatively, mechanical deformation-based solid-state AM is more frequently adopted to process Al alloys due to their ductile characteristics [8].

Even with the abovementioned drawbacks, the AM of Al alloys has attracted increased interest from the industry due to the excellent properties that Al alloys provide and the fabrication advantages that AM offers. It has now evolved from prototyping to production technology, and production is predicted to overtake prototyping around 2027 (Fig. 1a) [14]. Likewise, the demand for AM-specific aluminum alloys is predicted to overtake that of the die-cast aluminum alloy by 2028 (Fig. 1b) [14].

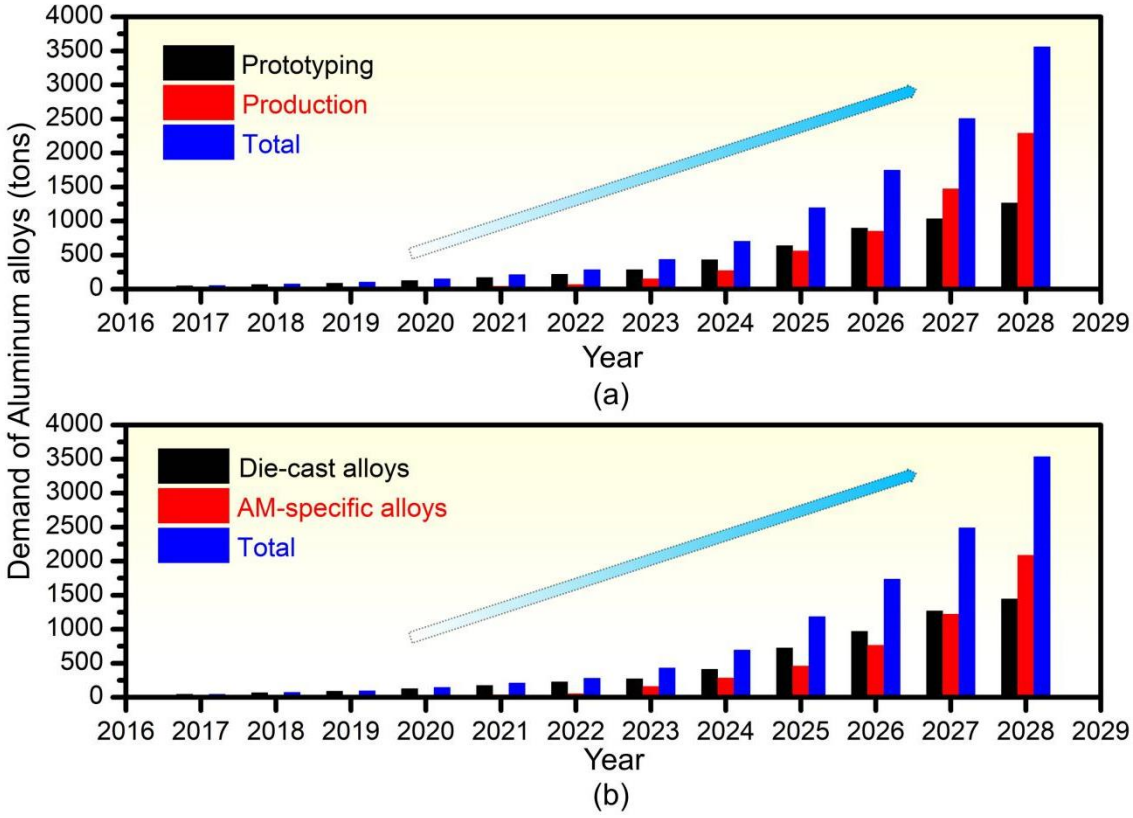

Fig. 1. Demand for aluminum alloys with year from 2017 to 2028 [14]**.** (a) Aluminum alloys for additive manufacturing (AM) part prototyping and additive manufacturing part production. (b) Die-cast and AM-specific Al alloys.

This review focuses on the AM of Al alloys and Al matrix composites (AMCs) via six different AM technologies, including fusion-based L-PBF, wire-arc additive manufacturing (WAAM), electron beam powder bed fusion (EB-PBF), laser powder direct energy deposition (LP-DED), sintering-based binder jetting (BJ), and solid-state-based additive friction stir deposition (AFSD). The pros and cons of each technology are presented in *Section 2*. Fig. 2(a) shows the statistical number of publications on the AM of Al and Al alloys based on L-PBF, WAAM, LP-DED, EB-PBF, and AFSD according to a survey of a total of about 2200 publications from 2006 to 2022. Since there is only one publication on the BJ of Al [15], it is not included in Fig. 2. There is an increasing trend of publications, especially after the year 2016, signifying the booming research in this field over the past five years. Among the various AM technologies, the L-PBF of unalloyed Al and Al alloys constitutes the largest portion,

while the processing of unalloyed Al and Al alloys via WAAM, EB-PBF, LP-DED, BJ, and AFSD is limited. The dominant role of L-PBF is also reflected by its high market share in the metal AM market. The revenue market share of L-PBF is 85% among the metal AM share in 2019 [16]. In terms of the Al alloy systems, the AM of Al–Si alloys takes the largest portion at 57.47% (Fig. 2b).

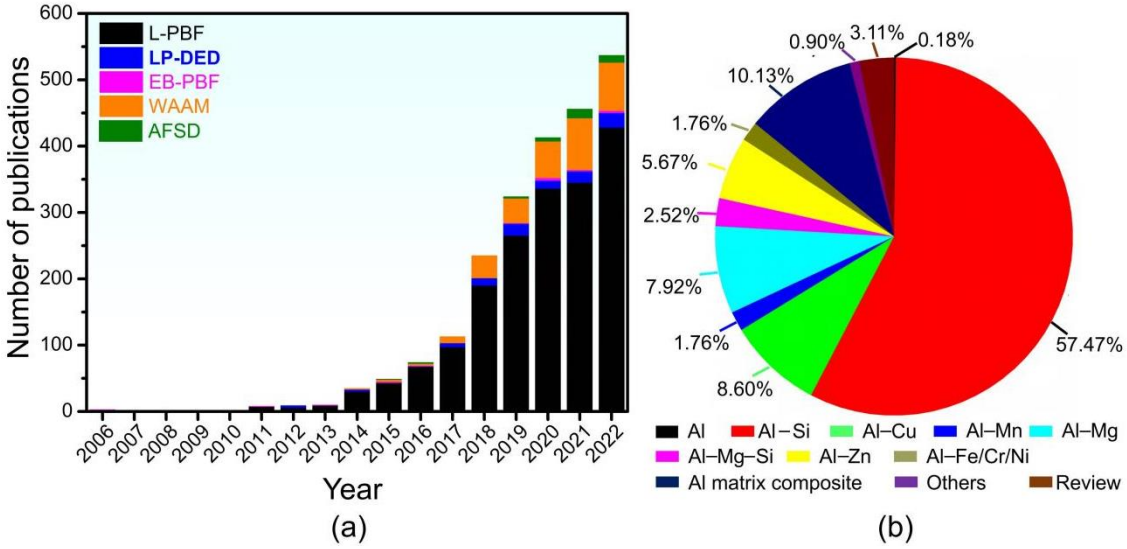

Fig. 2. Evolution trend and pie chart of publications on additive manufacturing aluminum alloys from year 2006 to 2022. (a) Number of publications on aluminum and aluminum alloys fabricated via additive manufacturing, including laser powder bed fusion (L-PBF), electron beam powder bed fusion (EB-PBF), laser powder direct energy deposition (LP-DED), wire-arc additive manufacturing (WAAM), and additive friction stir deposition (AFSD). (b) Research publications on additive manufacturing of various aluminum materials, including Al, Al–Si, Al–Cu, Al–Mn, Al–Mg, Al–Mg–Si, Al–Zn, and Al matrix composites (AMCs). The data is based on research publications from Web of Science, ScienceDirect, and Springer.

Since the AM of Al alloys is a fast-evolving field with flourishing interest, especially considering the growing demand and trend towards larger batches of industrial production [14], it is necessary to assess our understanding and recent progress regarding the AM of Al alloys. As a result, a number of review papers discussing the progress of the AM of Al alloys have been published since 2015 and some of these are

listed in Table A. 1 in the Appendix. However, these reviews generally focused on a specific AM technology, especially L-PBF, while fabrication of Al alloys via other AM methods, such as EB-PBF [17], LP-DED [18], WAAM [19], BJ [15], and AFSD [20], are seldom mentioned. The present review article discusses the abovementioned six technologies from the following perspectives that should be of interest to AM specialists and metallurgists, and especially to researchers on the AM of Al alloys. Firstly, six different AM technologies instead of a specific technology are covered. The pros and cons of each technology, as well as the challenges, are discussed. Secondly, since the AM of Al alloys is undergoing a fast evolution in both academic and industrial fields, it is necessary to review current developments. Recent progress from industrial fields, such as the novel AM-specific Al compositions and industrial components, is reviewed, which is seldom mentioned in other reviews. After presenting the classification of AM technologies (*Section 2*) and Al alloys (*Section 3*), *Sections 4* and *5* review the recent progress in the AM of Al alloys in detail. The microstructure and properties of unalloyed Al and Al alloys fabricated via each technology are described and inter-compared. Emphasis is put on L-PBF unalloyed Al and Al alloys, since this technology comprises the largest portion (*Section 4*). *Section 5* presents the recent progress of fabricating unalloyed Al and Al alloys via other AM technologies, including LP-DED, EB-PBF, WAAM, BJ, and AFSD. As an important supplement to the unalloyed Al and Al alloys, *Section 6* updates the fabrication of AMCs via AM. The AM-fabricated Al products are listed in *Section 7*. Finally, the conclusion of the review paper and the outlook for developing Al alloys via AM technology are presented in *Sections 8* and *9*, respectively.

2. Process description of additive manufacturing technologies

2.1 Classification

Metal AM techniques can be categorized into melt-based and solid-state-based ones (Fig. 3) depending on the layer bonding method and consolidation mechanism [8]. The

melt-based methods rely on material bonding by local melting while the materials remain solid during the solid-state AM process even though some fraction of liquid-phase formation occurs during the consolidation stage. The melt-based AM processes include PBF, LP-DED, and WAAM techniques [8,21]. Depending on the primary heat source, PBF can be further divided into L-PBF and EB-PBF [1]. These four melt-based AM technologies for fabricating Al alloys and Al matrix composites will be reviewed here. Solid-state AM techniques can be categorized into sintering-based and mechanical deformation-based ones. Sintering-based solid-state AM provides the driving force for material bonding through thermal energy, which can be categorized into three methods, BJ [22], metal extrusion (ME) [23], and screen or stencil printing (SP) [24]. Up to now, sintering-based AM has been adopted to fabricate steel, Inconel alloy, Cu, and ceramic components [25], yet the fabrication of Al alloys using this method is relatively unexplored [8]. This is due to the extremely low oxygen content and water vapour partial pressure required for sintering highly reactive Al alloys. However, ExOne and the Ford Motor Co. recently successfully printed an Al6061 alloy with high densification and comparable mechanical properties relative to those fabricated via traditional methods [26]. This breakthrough indicates that the BJ can potentially fabricate Al alloys for industrial applications in the future. Therefore, it is briefly reviewed in the present paper even though there is presently only one publication on this method. Compared with sintering-based solid-state AM, mechanical deformation-based AM employs kinetic energy to facilitate the bonding between layers. Depending on the method employed for the kinetic energy delivery, the mechanical deformation-based AM can be divided into ultrasonic AM (UAM) [27], AFSD [28], and cold spray (CS) [29] techniques. UAM and CS technologies only involve deformation around the interface or particles contact regions, while AFSD involves deformation of every voxel of the feed materials [28]. Furthermore, CS technology often results in porosity and micro-cracks due to incomplete bonded interfaces, which deteriorates the mechanical performance [30]. While these three solid-state deformation-based technologies have been used to fabricate Al alloy components, prior investigations have indicated that AFSD is the only AM technology that could result in components with mechanical

performance comparable to that of wrought counterparts [28]. Hence, we only focus on AFSD here.

Metal AM			
Melt-based AM		Solid-state-based AM	
Powder bed fusion	Direct energy deposition	Sinter-based AM	Mechanical-deformation-based AM
L-PBF	EBFF	BJ	UAM
EB-PBF	WLAM	ME	AFSD
	LP-DED	SP	CS
	WAAM		
L-PBF: Laser powder bed fusion **EB-PBF:** Electron beam powder bed fusion **EBFF:** Electron beam freeform fabrication **WLAM:** Wire laser additive manufacturing **LP-DED:** Laser powder direct energy deposition **WAAM:** Wire-arc additive manufacturing		**BJ:** Binder jetting **ME:** Metal extrusion **SP:** Screen or stencil printing **UAM:** Ultrasonic additive manufacturing **AFSD:** Additive friction stir deposition **CS:** Cold spray	

Fig. 3. Classification of additive manufacturing processes based on material bonding methods [8]**.** This review only covers laser powder bed fusion (L-PBF), electron beam powder bed fusion (EB-PBF), laser powder direct energy deposition (LP-DED), wire-arc additive manufacturing (WAAM), binder jetting (BJ), and additive friction stir deposition (AFSD).

2.2 Characteristics of additive manufacturing technologies

This section describes the basic principles of the L-PBF, EB-PBF, LP-DED, WAAM, BJ, and AFSD technologies. Schematic diagrams illustrating the principles of each technology and processing characteristics, including the advantages and limitations, are presented in Fig. 4.

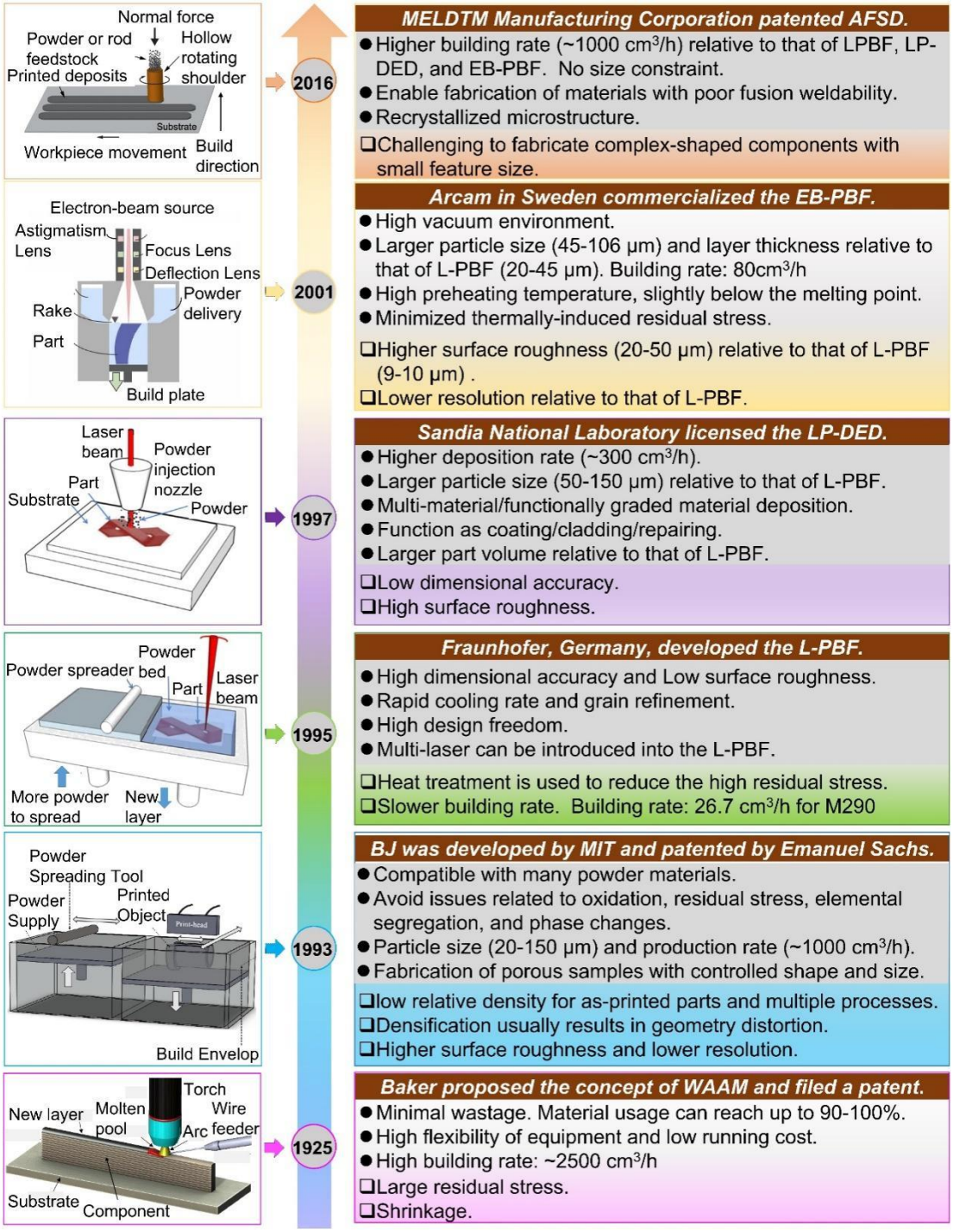

Fig. 4. Schematic graph and processing characteristics of the additive manufacturing (AM) technologies. Wire-arc additive manufacturing (WAAM) [31,32], binder jetting (BJ) [22,33-35], laser powder bed fusion (L-PBF) [1,32,36,37], laser powder direct energy deposition (LP-DED) [1,38,39], electron beam powder bed fusion (EB-PBF) [37,40-42], and additive friction stir deposition (AFSD) [8,43].

The inception of WAAM can be traced back to 1925 when the first patent was filed [44]. During the WAAM process, the following subsystems are involved [45]: (1) a torch to deposit the wire based on the heat input; (2) a positioning system to follow the path of geometry; (3) a teach pendant to control the positioning system; (4) a wire feeder to control the deposition of material. (5) an ancillary equipment to supply the shielding gas. The advantages of WAAM include: (1) low capital investment and the components of a WAAM can be derived from open-source equipment [46]; (2) a high deposition rate. The deposition rate of WAAM can reach up to 2500 cm^3/h [32], which is much higher than that of LP-DED (~300 cm^3/h) [38].

BJ, developed by MIT and patented by Emanuel Sachs [22], normally includes several processing steps: (1) A layer of powder is spread and joined into the desired shape with the binder. The printed area is lowered by the pre-set Z value, and the subsequent layer is uniformly spread. The process is repeated till the part is printed. (2) The powder bed is cured at about 200 °C to strengthen the printed green part. (3) The printed green part is transferred to a furnace to remove the binder, and a high-temperature sintering process under controlled conditions is used to obtain the final parts. The advantages of BJ include the following: (1) Since it does not involve fusion, virtually any powder material may be sintered. It can potentially have the widest selection of materials of all AM processes [47]. (2) Printing is conducted at room temperature and atmospheric pressure, thus, oxidation, residual stress, and elemental segregation are minimized. (3) Higher production rates and larger volume can be achieved relative to those of other AM technologies. (4) BJ can be utilized to fabricate porous structures. However, BJ also has some of the following disadvantages: (1) post-processing is needed to densify the samples, (2) Densification normally leads to the distortion of the geometry, and (3) Higher surface roughness and lower dimensional accuracy relative to those of PBF counterparts.

L-PBF technology, developed in 1995 in Fraunhofer [48], selectively melts the spread powders pass-by-pass and layer-by-layer using a laser as the heat source in an inert

chamber [1]. As the most versatile form of metal printing technology, L-PBF boasts the merits of high resolution, printing fine feature sizes, and almost no limitation on design freedom [49]. However, it also suffers from a slower building rate.

LP-DED, invented by the Sandia National Laboratories [50], relies on the feeding of powders into the melt path created by a laser beam to fabricate the material layer-by-layer. Shielding gas is normally adopted to protect the molten metal from oxidation. The advantages of LP-DED include the following: (1) higher deposition rates and enabling larger components relative to L-PBF; (2) coarser powders can be used relative to L-PBF, which can provide cost and safety advantages; (3) more capable of repairing relative to L-PBF; and (4) the capability to fabricate components with multi-materials or functionally-graded-materials (FGM). The limitations of LP-DED include lower dimensional accuracy and higher surface roughness relative to L-PBF. To pave the way for applications when larger components are needed, the LP-DED of Al alloys is reviewed in the present work. It should be noted that wire-based DED-WLAM has also been applied to fabricate Al alloys when the feedstock materials are in the form of wires [51]. Here, we only focus on LP-DED with powder as the feedstock material.

The working principle of EB-PBF, commercialized in 2001 by Arcam [52], is similar to that of L-PBF, except that an electron beam is used as the heat source to selectively melt the powders within a vacuum chamber [53]. The substrate is normally preheated during EB-PBF, which can effectively reduce the build-up of residual stresses in the fabricated part. Furthermore, EB-PBF is performed under vacuum conditions, which can reduce the oxidation of the alloy. This feature is especially beneficial for oxygen-sensitive materials, such as Al and Ti alloys. Finally, the powder size and layer thickness used for EB-PBF are larger than those in L-PBF, resulting in a higher deposition rate. However, the surface roughness of EB-PBF printed parts is generally higher than that of L-PBF parts.

AFSD technology was patented by the US-based MELD^{TM} Manufacturing Corporation

[54]. The notion of AFSD arises from friction stir welding (FSW) developed at The Welding Institute (TWI) in the UK as a solid-state joining technique [55]. The solid-state AFSD relies on forcing a feedstock material, either in the form of a rod or powders, through a hollow, non-consumable rotating tool against a substrate [56]. The friction generated by the rotation between the forced feedstock and the tool generates sufficient heat to soften the feedstock to accommodate the high shear and severe plastic deformation to metallurgically bond the substrate and the subsequently deposited layers [56]. The advantages of AFSD include: (1) compared with the L-PBF, EB-PBF, and LP-DED techniques, AFSD allows for a higher deposition rate, which can reach 1000 cm^3/h for the Al alloys [43]; and (2) the volume of the built part is not size-limited, since no vacuum or environment is needed for the printing process. In contrast, AFSD technology shows the limitations of building complex parts with small feature sizes.

3. Classification of aluminum alloys

According to the ASTM standards, Al alloys can be divided into two major groups, namely wrought alloys and cast alloys, depending on the manufacturing methods used [9]. Different nomenclatures have been employed to identify them. A four-digit notation is used to describe wrought alloys while a three-digit notation followed by a decimal value is adopted to describe cast Al alloys. Up to now, ~ 80% of the Al alloys adopted as structural materials have been wrought ones [57]. Furthermore, Al alloys can be labelled as heat-treatable or non-heat-treatable alloys, depending on the primary mechanism of property development. Heat-treatable Al alloys rely on thermal treatment to strengthen the alloy, while non-heat-treatable Al alloys depend on work hardening. Finally, Al alloys can be classified into various families based on their constituents. For example, the Al5xx.x (cast) and Al5xxx (wrought) alloys rely on Mg as the principal alloying element. The detailed classification of various cast and wrought Al alloys, including the strengthening mechanisms (Fig. 5a) and ultimate tensile strength range (Fig. 5b,c), is presented in Fig. 5. However, since the fabrication route of AM is different from that of conventional casting and wrought methods, the composition of

AM-specified Al alloys also undergoes modification, which makes it inappropriate to classify the AM-specified alloys into particular series of Al alloys. Furthermore, the novel composition and AM processing characteristics may alter the "heat-treatable" characteristics. A typical example is the Al–Mg-based alloy, which is work-hardenable based on conventional processing methods. However, the addition of Sc and Zr in conjunction with the non-equilibrium processing manner make the L-PBF Al–Mg–Sc–Zr alloy heat treatable [11]. Thus, the traditional classification of Al alloys based on heat treatability does not work well for AM Al alloys. As a result, the Al alloy series are classified based on the major constituents in the present review, which include Al, Al–Cu, Al–Mn, Al–Si, Al–Mg, Al–Mg–Si, Al–Zn, Al–Fe, Al–Li, and Al–Sn.

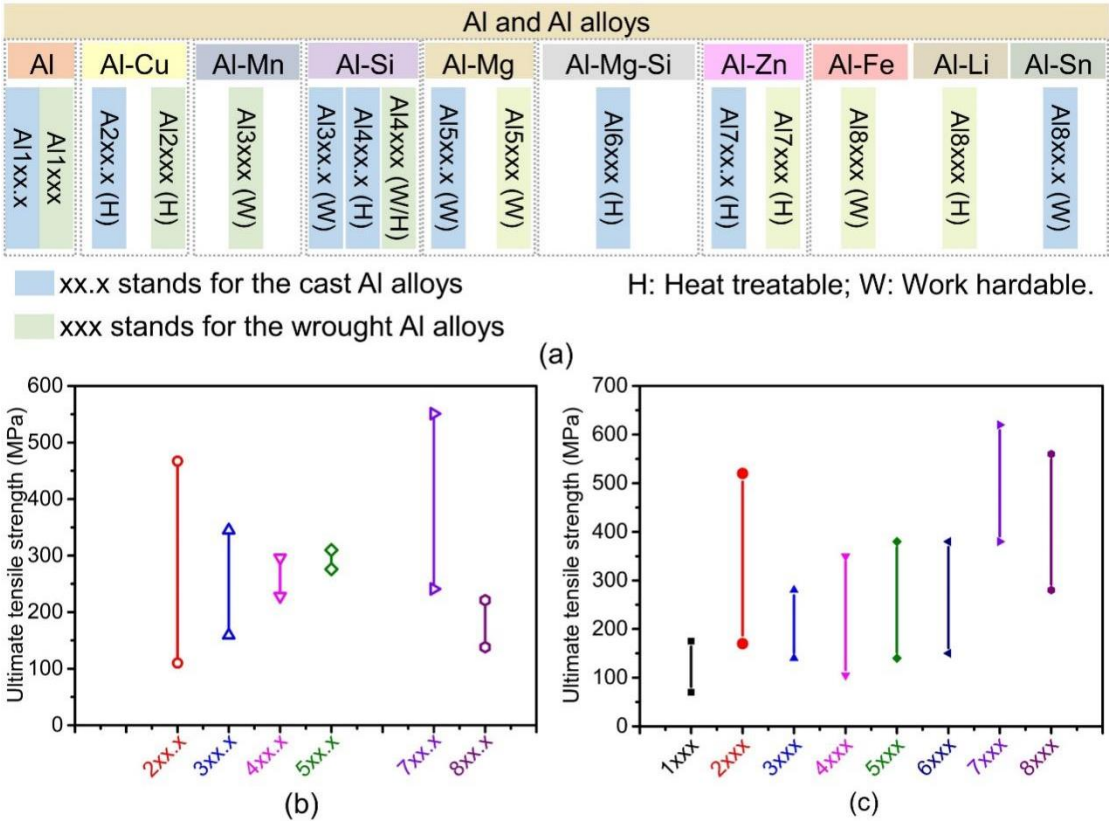

Fig. 5. Classification of various classes of aluminum alloys. (a) Classification of aluminum alloys and their strengthening mechanism. (b) Ultimate tensile strength of various cast and wrought aluminum alloys. The information was based on Ref. [9,58-60].

4. Fabrication of aluminum and aluminum alloys via laser powder bed fusion

The fabrication of Al alloys via L-PBF constitutes the largest portion among the six different AM technologies discussed, and the number of publications on the L-PBF of Al alloys is increasing rapidly (Fig. 2). This signifies the extensive research interest driven by scientific issues as well as pushing the technology forward towards practical applications. This chapter begins with the introduction of defect control and microstructure of L-PBF Al alloys (*Section 4.1*). Subsequently, post-heat treatment procedures and their effect on the microstructure evolution (*Section 4.2*), mechanical properties (*Section 4.3*), and corrosion properties (*Section 4.4*) of L-PBF unalloyed Al and Al alloys are reviewed. In *Section 4.5*, the recent trends for developing high-temperature Al alloys are reviewed. Then, the effect of powder feedstock and degradation on the microstructure and mechanical properties (*Section 4.6*), and oxidation and element evaporation (*Section 4.7*) for the L-PBF Al alloys are reviewed. Finally, the advantages and limitations of fabricating Al alloys via L-PBF are discussed (*Section 4.8*). The recent progress, limitations, and outlook are presented in both a qualitative and quantitative way.

4.1 Defect control and microstructure

This section reviews the microstructure of as-built unalloyed Al and Al alloys, including Al–Si alloys, and moderate- and high-strength Al alloys (Al–Cu, Al–Mn, Al–Mg, Al–Mg–Si, and Al–Zn). For the unalloyed Al and Al–Si alloys, microstructure analysis is the focus. For the moderate- and high-strength Al alloys, the strategies to overcome the cracks and corresponding microstructure are described.

4.1.1 Unalloyed Al

The unalloyed Al, viz. Al1xx.x and Al1xxx, contain 99.00% or higher purity Al. They are utilized in industry extensively due to their excellent corrosion resistance, and high

thermal and electrical conductivities. However, investigation on the AM of unalloyed Al is not actively pursued due to their low mechanical strength. To the best of the author's knowledge, there are few papers reporting the microstructure of L-PBF unalloyed Al [61,62]. The as-built sample exhibits columnar grains along the build direction. Elementum 3d [63] and m4p material solution GmbH [64] have commercialized the L-PBF unalloyed Al powders. Al parts with a relative density higher than 99.5% can be fabricated.

4.1.2 Pore formation and elimination of laser powder bed fusion Al alloys

Due to their low freezing range and high fluidity, Al-Si alloys exhibit excellent L-PBF printability. However, inappropriate printing parameters can engender porosity as well, which can influence the yield strength, ultimate tensile strength, and especially, elongation [65]. Thus, it is critical to understand the pore formation mechanism and, in turn, to eliminate the pores to achieve high performance. To understand the pore formation mechanism, the conventional route is based on the post-analysis of spatial distribution and the morphology of pores for the as-printed samples and their relationship with the printing parameters [66].

Recently, with the aid of state-of-the-art in-situ X-ray imaging, the interaction between the laser and powders is recorded, from which the formation processes of pores and spattering were probed in real time [67-69]. Based on the in-situ X-ray imaging, six pore formation mechanisms were reported, namely the pore formation from feedstock, keyhole-induced pores, pore formation arising from the volatile substance or expansion from tiny trapped gas, pore trapped by surface fluctuation, pore formation due to depression zone fluctuation, and pore formation from a crack. Based on the in-situ x-ray imaging of AlSi10Mg powders, three different domains, namely, the melt pool-laser interaction domain, the circulation domain, and the transition domain, were identified. In the laser interaction domain, the pores are eliminated by escaping from the melt pool. In the circulation domain, the pores circulate in the melt pool. In the transition domain, the movement of pores is irregular. Hojjatzadeh et al. [66] have proposed that the

thermocapillary force induced by the high-temperature gradient is the driving force for pore elimination. The online monitoring of pore formation can shed light on fabricating pore-free samples via L-PBF.

4.1.3. Hierarchical microstructure of laser powder bed fusion Al–Si alloys

Among the various Al–Si alloys [70], Al–12Si, AlSi10Mg, and AlSi7Mg0.6 (A357) alloys are the most extensively investigated due to their excellent fluidity, high thermal conductivity, and excellent printability. The eutectic composition of the Al-*x*Si alloy system consists of about 12.6 wt.% Si [71] with a eutectic temperature of 578.8 °C. Up to now, the hypoeutectic, eutectic, and hypereutectic Al–Si alloys have been processed with L-PBF [71]. The L-PBF hypoeutectic Al–Si alloys (Al−12Si [72], AlSi10Mg [73], and A357 alloys [74]) exhibited a hierarchical microstructure spanning a multi-length scale. At the macron-scale, micron-sized coarse columnar grains grow epitaxially with a <001> fibre texture along the build direction, and some equiaxed grains were observed in the melt pool boundary for L-PBF AlSi10Mg alloy [73] (Fig. 6a). At the sub-micron-scale, cellular structures with the boundary rich in Si were observed inside the coarse columnar grains (Fig. 6b-d) [75]. At the nanoscale, the Si particles formed in the interior of cellular structures (Fig. 6e) [76]. Moreover, the hierarchical microstructure is tuneable via modifying the printing parameters, such as the scanning speed, hatch spacing, and layer thickness. Lower scanning speeds engender larger cell sizes due to a faster cooling rate [77], while a smaller hatch spacing generates a high fraction of melt pool boundaries [78]. With an increase of layer thickness, the solidification morphology of the cellular structure and texture are altered due to the varied thermal gradient [79].

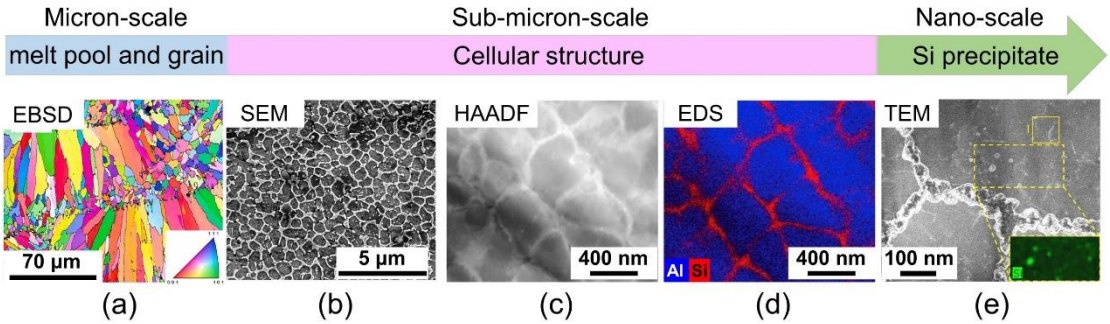

Fig. 6. Hierarchical microstructure of as-built laser powder bed fusion AlSi10Mg alloy. (a) Electron backscattered diffraction and (b) Scanning electron microscopy image showing the cellular structure of the as-built AlSi10Mg alloys [73]. (c) High angle annular dark field scanning transmission electron microscopy (HAADF-STEM) and (d) Energy dispersive spectrum (EDS) mapping of the cellular structure [75]. (e) High angle annular dark field (HAADF)/Energy dispersive spectrum (EDS) maps showing the nano-sized Si particles in the as-built AlSi10Mg alloy [76].

Apart from the above three most studied Al–Si alloys, the microstructure and mechanical properties can be further tailored via composition modification. Si content plays a significant role in the printability, microstructure, and mechanical properties of L-PBF Al–*x*Si alloys (x = 0.5, 1.0, 2.0, 4.0, 12.6, and 16.0) [71]. Crack-free Al–Si samples were achieved for the Al–0.5Si, Al–4.0Si, and Al–12.6Si samples while Al–1.0Si and Al–2.0Si samples exhibited cracks, which was explained by the hot crack susceptibility index. Si partitioning occurred for all the as-printed Al–*x*Si samples (Fig. 7a-f), yet cellular structure with well-defined boundaries formed only when the Si content increased to 12.6% (Fig. 7e) and 16.0% (Fig. 7f). Furthermore, the average cell size decreases with increasing scanning speed due to a faster cooling rate at a constant laser power. Apart from Si content, novel AM specific Al–Si alloys by tailoring Mg content were designed driven by high mechanical performance. Geng et al. [80] have developed an AlSi8.1Mg1.4 alloy with a higher Mg content relative to that of conventional casting alloys (Mg < 0.75 wt.%). The increased Mg content is mainly used to enhance the solid solution strengthening and trigger the formation of β" phase after direct aging instead of the nano-sized Si particles for the AlSi10Mg alloys. The L-PBF AlSi8.1Mg1.4 sample exhibited a hierarchical microstructure consisting of fine grains along the melt boundary and coarse grains towards the centre of the melt pools (Fig. 7g). The Guinier Preston (GP) formed in the cell interior of fine grains (Fig. 7h). Additionally, Si particles with sizes of 3–7 nm were observed (Fig. 7i). The above results indicate that the hierarchical microstructure of L-PBF Al alloys can be tailored in a broad range by modifying the process parameters and chemical composition.

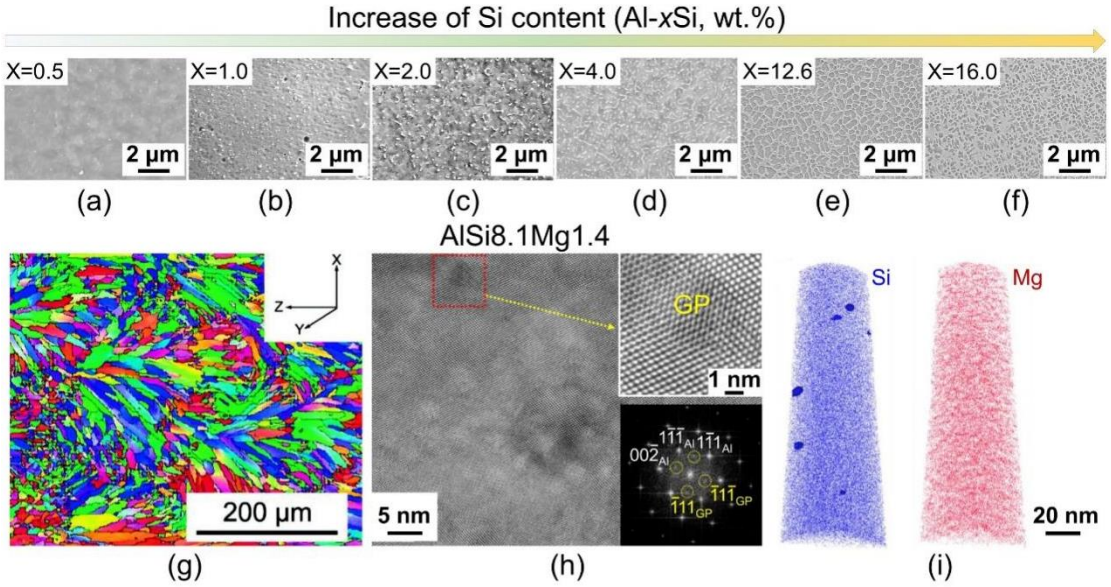

Fig. 7. Microstructure of the laser powder bed fusion Al–Si alloys. (a-f) Scanning electron microscopy (SEM) images of Al–0.5Si, Al–1.0Si, Al–2.0Si, Al–4.0Si, Al–12.6Si, and Al–16.0Si, respectively [71]. (g) Electron backscattered diffraction (EBSD) map of the as-built AlSi8.1Mg1.4 alloy [80]. (h) High-resolution lattice image and fast Fourier transform (FFT) image (inset) show the formation of nanosized Guinier-Preston (GP) zone [80]. (i) Atom probe tomography (APT) characterization of the distribution of Si and Mg in the as-built AlSi8.1Mg1.4 alloy [80].

4.1.4 Crack formation of the laser powder bed fusion moderate- and high-strength Al alloys

(i) Crack formation mechanism

The L-PBF processing of moderate- (Al-Mg) and high-strength (Al–Cu, Al–Mg–Si, and Al–Zn) Al alloys remains challenging due to the formation of troublesome cracks [81], yet it has gained significant interest in recent years due to its applications in the aerospace industry. The crack phenomenon during L-PBF of moderate- and high-strength Al alloys is usually associated with solidification shrinkage [82] and a relatively large freezing range [83]. The cracks include both hot cracks and cold cracks [84]. Hot cracking is thought to arise from shrinkage during solidification. At the final stage of solidification, the unstable and undercooled solute enriched melt produces interdendritic channels with a thin layer of liquid [83]. The hot cracks are usually

located along the grain boundary, while cold cracks arise from the propagation of hot cracks along vertical grain boundaries. To eliminate the cracks, extensive efforts have been made by tailoring the printing parameters [85], printing conditions (such as baseplate preheating) [86], composition modification [87], and inoculation treatment [10].

(ii) Process parameter optimization and the associated microstructure

Printing parameter tailoring, such as the scanning speed and hatching space, was naturally the first solution proposed to heal cracks. Fig. 8 shows some examples of printing optimization for L-PBF moderate- and high-strength Al alloys via modifying scanning speeds while fixing other printing parameters. As for Al–Cu–Mg [88] (Fig. 8a) and Al5083 alloys [83] (Fig. 8b), the density and fraction of cracks decrease with lower scanning speeds. Crack-free samples were obtained at lower scanning speeds for Al–Cu–Mg (5 m/min and 8 m/min) and Al5083 alloy (100 mm/s). However, the lowest scanning speed associated with excessive energy density leads to the formation of keyhole mode and large pores (Fig. 8b). The increased densification and crack healing with lower scanning speeds are due to the following mechanisms. Firstly, the relatively higher energy density with lower scanning speeds decreases the surface tension and improves the wettability of liquid metal. Furthermore, the higher laser energy density triggers the formation of liquid with low viscosity, which promotes liquid spreading. Finally, the longer dwelling time due to a lower scanning speed ensures fluidity to backfill the dendrite shrinkages [88]. For the L-PBF Al6061 (Fig. 8c), cracks formed irrespective of the scanning speeds, and spherical porosity evolved into irregular porosity with increasing scanning speeds [89]. For the L-PBF Al7075, the crack density decreases when lowering the scanning speed, yet the cracks cannot be eliminated (Fig. 8d) [90], similar to that of Al6061. The crack healing with lowering scanning speeds is ascribed to the more significant evaporation of Mg and Zn, resulting in a lower crack susceptibility. Recently, crack-free Al–3.6Zn–0.6Mg alloy was fabricated via higher laser power and lower scanning speed [91], which is caused by the reduced pressure drop between two adjacent grains at lower scanning speeds. However, the composition

of as-printed samples is not given in their work, and the crack susceptibility of printed samples is unknown. Apart from the scanning speeds, hatching space was also adopted to tailor the printability of L-PBF high-strength Al alloys [81]. A smaller hatching space is beneficial for healing the cracks for the L-PBF Al–Cu alloys, since the cracks initiated during previous scanning may be eliminated.

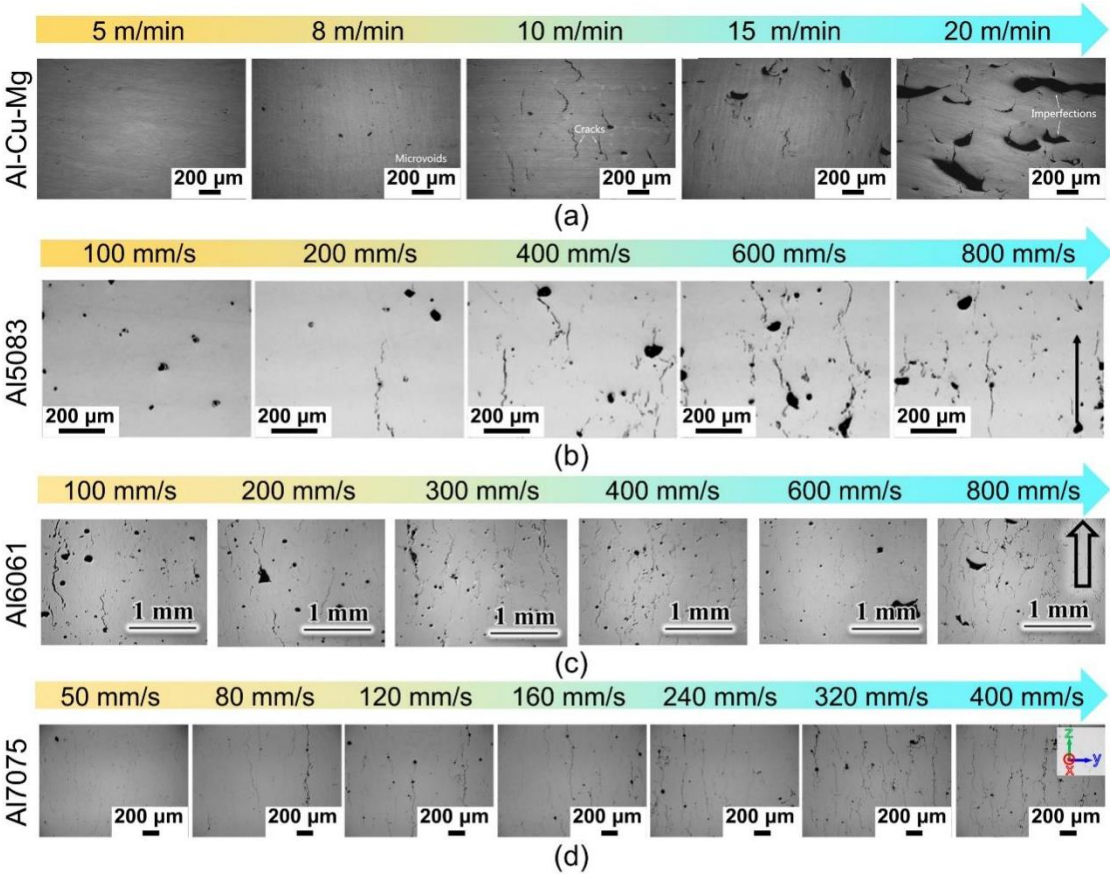

Fig. 8. Optical micrographs of the laser powder bed fusion Al–Cu, Al–Mg, Al–Mg–Si, and Al–Zn alloys. (a) Al–Cu–Mg alloy [88]. (b) Al5083 alloy [83]. (c) Al6061 alloy [89]. (d) Al7075 alloy under different printing parameters [90].

Apart from tailoring printing parameters, baseplate preheating is another method to improve the printability of the "difficult-to-print" alloys, taking advantage of reduced solidification undercooling and thermal gradient [86,92]. Crack-free Al6061 samples were printed via L-PBF when the powder bed temperature reaches 500 °C (Fig. 9a,b) [86], which is associated with reduced solidification undercooling. Preheating the baseplate can alleviate the cracks in L-PBF Al7075 (Fig. 9c,d) through decreasing the thermal gradient [92]. However, baseplate preheating is not universal for eliminating

cracks and cracks could not be eliminated for the Al7075 alloy [92]. In some cases, the baseplate heating could even deteriorate the printing quality by introducing longer cracks across the specimen and more porosity compared to those of counterparts without baseplate heating, such as for the L-PBF EN AW-2024 [93]. The higher fraction of porosity is ascribed to overheating. The formation of longer cracks is due to the fact that once a crack forms, it serves as a local stress accumulator to induce crack propagation [93].

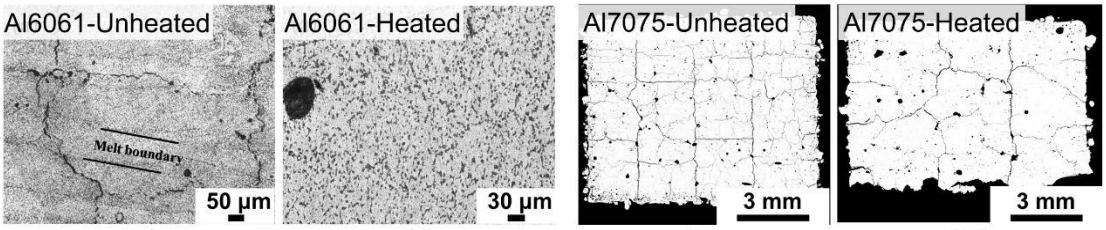

Fig. 9. Optical micrographs of laser powder bed fusion Al6061 and Al7075 samples. (a,b) Al6061 specimens fabricated on unheated powder bed and heated powder bed [86]. (c,d) Al7075 specimens fabricated without baseplate heating and with baseplate heating [92].

(iii) Crack elimination via composition modification

Relative to tailoring process parameters, composition modification is more frequently adopted to eliminate cracks. The purpose of composition modification is to decrease solidification crack susceptibility, enhance fluidity, or refine grains. The addition of Y particles can heal the cracks of L-PBF Al2024 due to the reduction of the brittle temperature range [87], which is the main reason for the decreased crack susceptibility [84]. The addition of Si has been well demonstrated to heal cracks of L-PBF Al7075 alloy (Fig. 10a) due to enhanced fluidity [94]. On one hand, the addition of Si to the L-PBF Al7075 alloy can refine the grains (Fig. 10b). On the other hand, the microalloying of Si reduces the melting temperature (enhancing the fluidity) and crack sensitivity by forming a low melting point eutectic phase for this alloy [94].

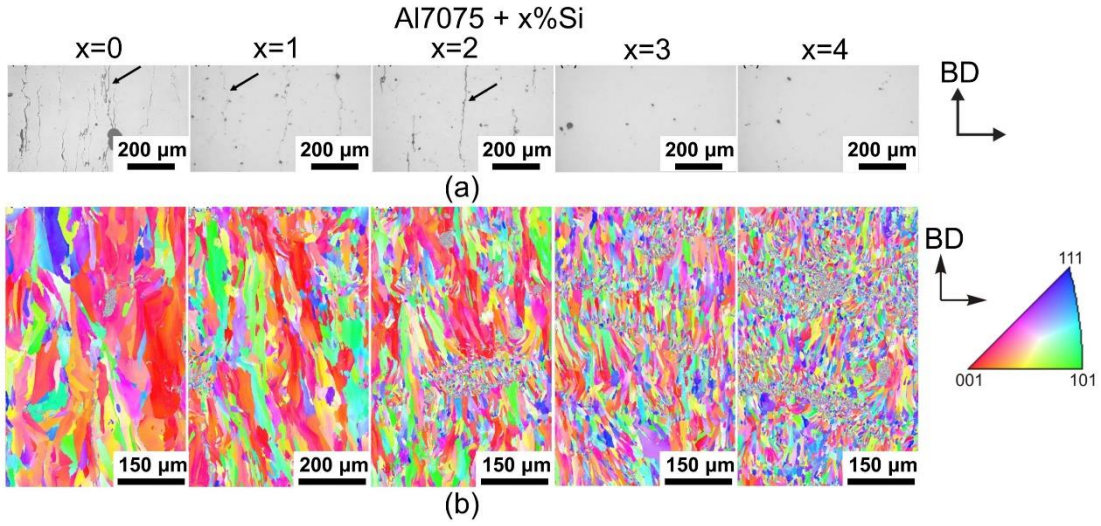

Fig. 10. Crack elimination of laser powder bed fusion Al–Zn alloys. (a) Optical micrographs and (b) Electron backscattered diffraction images of the Al7075 and Si-modified Al7075 alloys [94].

Apart from decreasing solidification crack susceptibility and enhancing fluidity, the grain refinement triggered via inoculation treatment is a more popular way to heal cracks [95-102]. The basic design concept of inoculation treatment is to introduce secondary particles, Al_3X (X = Zr, Sc, Ti, and Nb), coherent with the Al matrix to refine the grains, which can prevent crack formation/propagation and enhance grain boundary strengthening. Compared with coarse columnar grains, fine equiaxed grains are beneficial for eliminating cracks for multiple reasons. The fine equiaxed grains made the crack propagation more tortuous as compared with the columnar grains. In addition, the fine equiaxed grains could increase the critical stress for hot-cracking and delay the onset of coherence of dendrites [96]. Fig. 11 shows representative examples of high-strength Al alloy inoculation treated with additives, including Al2024 modified with Ti (Fig. 11a_1,a_2) [97], Al5083 modified with Zr (Fig. 11b_1,b_2), Al6061 modified with YSZ (Fig. 11c_1,c_2) [95], and Al7075 modified with Nb (Fig. 11d_1,d_2) [90]. Though the macroscopic grain refinement was observed for all the samples, the grain refinement efficiency is different. For the Ti (Fig. 11a_1,a_2) and Nb (Fig. 11d_1,d_2) inoculation-treated Al2024 and Al7075 alloys, they manifest full decoration of fine equiaxed grains. In contrast, the Zr- (Fig. 11b_1,b_2) modified Al5083 [83] and YSZ- (Fig. 11c_1,c_2) modified

Al6061 [95] consist of multi-modal grain size distribution, including coarse columnar grains and ultrafine equiaxed grains.

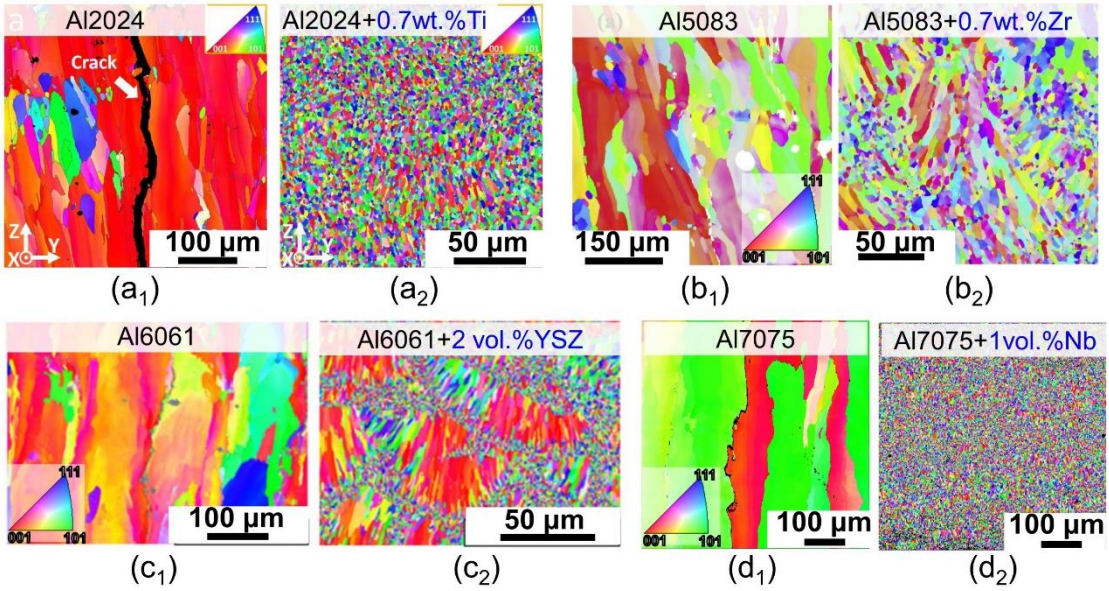

Fig. 11. Grain refinement of laser powder bed fusion moderate- and high-strength aluminum alloys. Electron backscattered diffraction images of: (a_1,a_2) Al2024 and Al2024 + 0.7 wt. % Ti [97]. (b_1,b_2) Al5083 and Al5083 + 0.7 wt.% [83]. (c_1,c_2) Al6061 and Al6061 + YSZ [95]. (d_1,d_2) Al7075 and Al7075 + Nb [90].

As for grain refinement efficiency, Martin et al. [62] have proposed that the lattice match between the inoculants and Al matrix plays a significant role in influencing the grain refinement efficiency based on a series of inoculants, such as TiB_2, α-Al_2O_3, Al_3Ti, Al_3Nb, and Al_3Ta particles. The findings revealed that a lower lattice mismatch engenders a better grain refinement efficiency. The coherency between Al_3Ti and Al matrix is shown in Fig. 12a,b_1,b_2. Apart from lattice mismatch, the grain refinement efficiency is also dependent on the fraction of inoculation-treated powders. A higher fraction of inoculation-treated powders provides richer nucleation sites for the heterogeneous nucleation of Al. A higher fraction of equiaxed grains formed with increasing YSZ content for the Al6061 alloy [95] and Nb content for the Al7075 alloy [90].

Specific to the heterogeneous microstructure with periodic columnar-to-equiaxed (CTE)

and equiaxed-to-columnar (ETC) transition, this is rationalized via heterogeneous solidification dynamics [101]. Along the melt pool boundaries, the relatively lower solidification front velocity can allow for the precipitation of Al_3Zr particles, which trigger the formation of primary Al_3Zr particles. However, when the solidification proceeds to the interior of the melt pools, the faster solidification front velocity leads to the solute trap of Zr into the matrix and inhibits the formation of Al_3Zr particles. Without the primary Al_3Zr particles in the interior of the melt pools, the columnar grains grow epitaxially. This theory has also been used to explain the multi-modal grain size distribution for the L-PBF Al–Mg–Zr alloy (Addalloy®) [11] and AlZnMgCuScZr alloy [102]. For the L-PBF Al–Mg–Zr alloy [11], the existence of Al_3Zr particles in the equiaxed grains and the disappearance of Al_3Zr particles in the columnar grains (Fig. 12c,d) support the explanation. Based on the multi-modal grain size formation mechanism, the factors that could influence the nucleation and growth of nucleates can affect the multi-modal grain size distribution. For instance, baseplate preheating [98], decreasing the hatch spacing [99], and laser remelting [100] can effectively lead to a higher area fraction of equiaxed grains. The enhanced volume fraction of equiaxed grains with baseplate heating is attributed to the reduced thermal gradient [98]. While the increased volume fraction of equiaxed grains associated with the decrease of hatch spacing [99] and laser remelting [100] is attributed to an increased remelting zone.

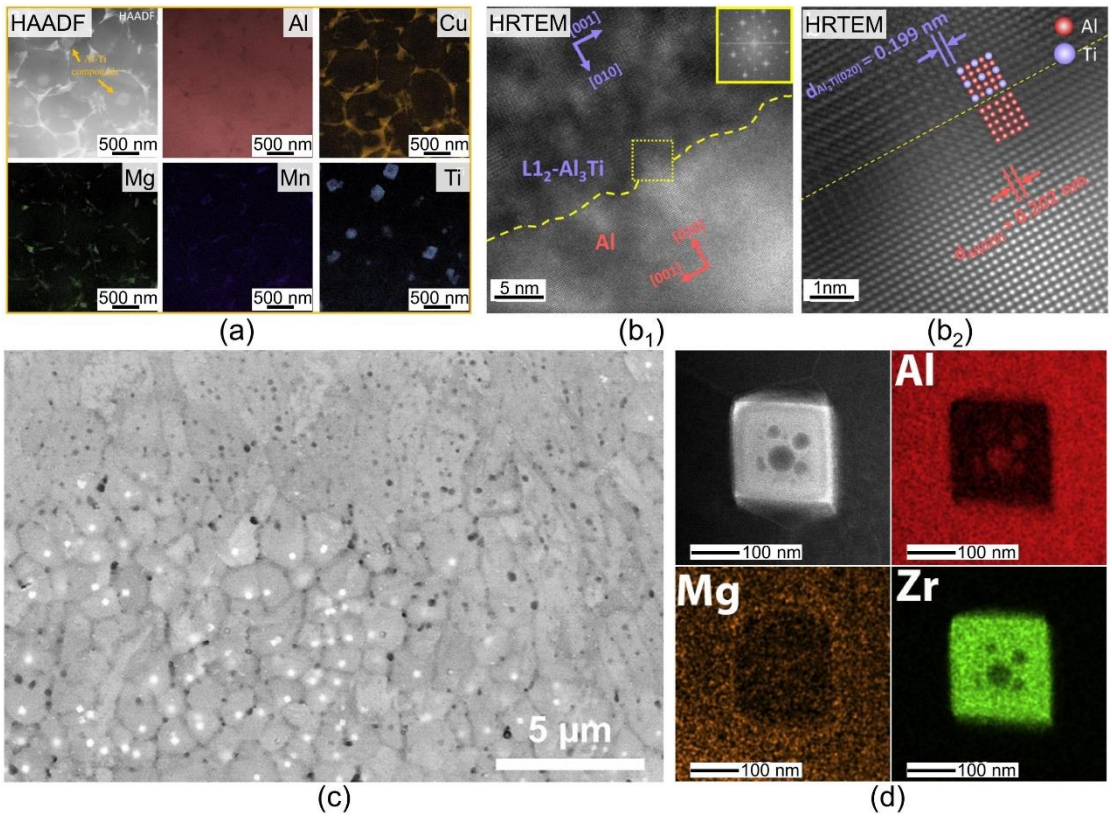

Fig. 12. Microstructure of laser powder bed fusion Al–Mg–Zr and Ti-modified Al2024 alloy. (a) High angle annular dark field scanning transmission electron microscopy (HAADF-STEM) image presenting the microstructure of the laser powder bed fusion Ti-modified Al2024 alloy and the corresponding energy dispersive spectrum (EDS) maps of the constituent elements [97]. (b_1,b_2) High resolution transmission electron microscopy (HRTEM) image showing the interface and coincidence between the Al matrix and $L1_2$-Al_3Ti particles. The inset shows the corresponding fast Fourier transform (FFT) pattern of the marked area [97]. (c) Scanning electron microscopy (SEM) image of the laser powder fusion Al–Mg–Zr alloy showing the nonuniform distribution of white-contrasted particles [11]. (d) Scanning transmission electron microscopy-energy dispersive spectrum (STEM-EDS) chemical maps of the precipitate in the fine-grain region [11].

Due to the universal ability to eliminate cracks by grain refinement, the inoculation treatment design philosophy has induced the rapid development of novel AM-specific alloys, some of which have matured for industrial applications. Industrial AM-specific

Al alloys include the A20x (Al–4.5Cu–0.3Mg–0.7Ag–3.5Ti) alloy developed by the Aeromet [103], the Addalloy® [11], and A7A77.60 alloy [104] developed by the HRL laboratory. The most well-known alloy system is the Scalmalloy® (Al–Mg–Sc–Zr) developed by AP works [105]. However, the evaporation of Mg and the formation of spatters occurred during L-PBF of Scalmalloy®. To overcome this issue, variants of Scalmalloy® have been developed by replacing Mg with Cr or Ti, including the Scancromal® alloy (Al–Cr–Sc–Zr), Scantital® (Al–Ti–Sc–Zr), and Zicromal® (Al–Cr–Zr–Mn) alloys [106,107]. The surface of the as-printed Zicromal® alloy and Scancromal® alloy looks shiny, while the as-printed Scalmalloy® generated a black surface due to the evaporation of Mg and formation of magnesium oxide (MgO) (Fig. 13a) [106]. Due to the different grain growth factor, Q (GRF), and a mismatch between the solute and Al matrix, the as-fabricated alloys exhibit different microstructures. For the Scalmalloy®, the high GRF (16.3 K) and formation of $Al_3(Sc_x,Zr_{1-x})$ particles exhibiting little mismatch with the Al matrix engenders a bimodal microstructure consisting of coarse grains and ultrafine grains (Fig. 13b). However, with the addition of Cr, the GRF (2.0 K) together with the formation of $Al_{11}Cr_2$ or $Al_{13}Cr_2/Al_7Cr$ highly mismatched with the Al matrix for the Scancromal® alloy resulted in epitaxial grain growth (Fig. 13b). For the Scantital®, the high GRF value (18.4 K) and the formation of Al_3Ti/Al_3 (Sc,Zr,Ti) particles coherent with the Al matrix contribute to the formation of uniform equiaxed grains without preferred texture (Fig. 13b).

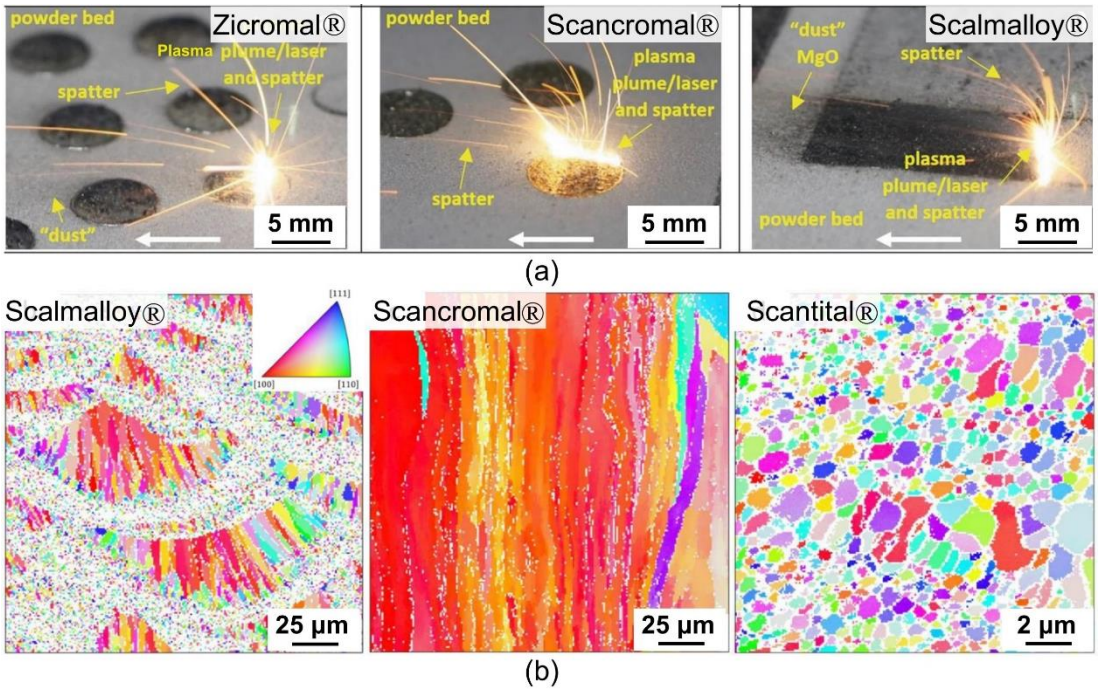

Fig. 13. Reflex camera image during laser powder bed fusion and electron backscattered scanning diffraction of laser powder bed fusion aluminum alloys. The reflex camera captured images during laser powder bed fusion process of (a) Zicromal®, Scancromal®, and Scalmalloy® alloys [106]. The arrows show the flow direction of argon. (b) show the electron backscattered scanning diffraction images of the laser powder bed fusion Scalmally®, Scancromal®, and Scantital® alloys [107].

4.2 Post-heat treatment and microstructure evolution

Due to the non-equilibrium processing characteristics during L-PBF, such as the extremely high cooling rate and thermal cycling, the L-PBF Al alloys normally tend to form a supersaturated solid solution with a hierarchical microstructure and generate residual stress. Thus, the post-heat treatment profiles need to be specifically designed for the L-PBF Al alloys instead of the conventional heat treatment profiles designed for cast or wrought Al alloys [108]. The heat treatment profiles normally consist of stress relief (SR) annealing [109], direct aging (DA) [110], and solution treatment (ST) followed by artificial aging (AA) in terms of STA [111]. The experimental procedures of SR and DA are similar, including maintaining the sample at a certain temperature for some time followed by cooling. The difference between the approaches is the

temperature. The SR of L-PBF Al alloys is usually conducted at about 300 °C for a couple of hours to release the huge residual stress [112], while DA is performed at a relatively lower temperature to induce precipitation by consuming the supersaturated solvent elements [113]. In consideration of the relaxed boundary between DA and SR, the single-step annealing is designated as DA. In contrast, the STA includes two steps, where ST is mainly used to dissolve the precipitates or intermetallics and artificial aging is used to induce the formation of finer dispersed particles. Some representative examples of the heat treatment effect on the microstructure evolution of L-PBF Al alloys are listed in Table A. 2 and are reviewed in detail.

4.2.1 Al–Si alloys

For the Al–12Si, AlSi10Mg, or Al–7Si–0.6Mg alloys, the conventional heat treatment profile includes two steps: ST followed by AA [108]. Extending this to the L-PBF Al–Si alloys, Li et al. [111] have found that the precipitation and coalescence of Si particles occur during ST of the L-PBF Al–12Si alloy (Fig. 14a). The Si content of about 7 wt.% in the as-built state drops to about 2 wt.% quickly (5 min) and then to an equilibrium content of about 1.6 wt.% when further solution treated (30 min, 2 h and 4 h) (Fig. 14a). Meanwhile, the Si particles grow most probably through Ostwald ripening and the coalescence of adjacent small Si particles (Fig. 14a). For the L-PBF AlSi10Mg alloy, the cellular structures disappear and the solute trapped Si elements run out to form Si particles, which got coarsened when STA (ST: 520 ˚C/2 h + AA: 180 ˚C/6 h) is adopted (Fig. 14b_1-b_3). The above two examples on L-PBF Al–12Si and AlSi10Mg indicate that the ST does not effectively dissolve the Si into the Al matrix, and triggered the precipitation of Si that is supersaturated in the matrix instead. To avoid the precipitation of coarsened Si particles, DA is shown to maintain the cellular structure (Fig.14b_1,b_4) [114], and the nano-sized Si particles (shown as red arrows) in the form of spherical shape and rod shape precipitate (Fig. 14b_5), which are semi-coherent with Al matrix (Fig. 14b_6) [115]. Moreover, due to the different microstructure relative to that of cast counterparts, the precipitation pathway might be different between cast and L-PBF Al–Si samples [110]. The dominant precipitates are B’ precipitates for the peak-aged A357

after STA [110] while β'' phase is the dominant precipitate in the peak-aged condition for as-cast A357 after STA. This unusual precipitation for the L-PBF Al Al–Si sample is due to the uniaxial strain in the sample.

In conclusion, for the L-PBF Al–Si alloys, DA generates the nano-sized precipitates by consuming the solute trapped elements [73,114], while STA engenders the removal of cellular structure, the reduction of Si content in the matrix, and the coarsening of Si particles [73,114]. In addition, the precipitation pathway is different for L-PBF and as-cast samples due to different starting microstructures [73], indicating novel heat treatment profiles need to be designed for high performance.

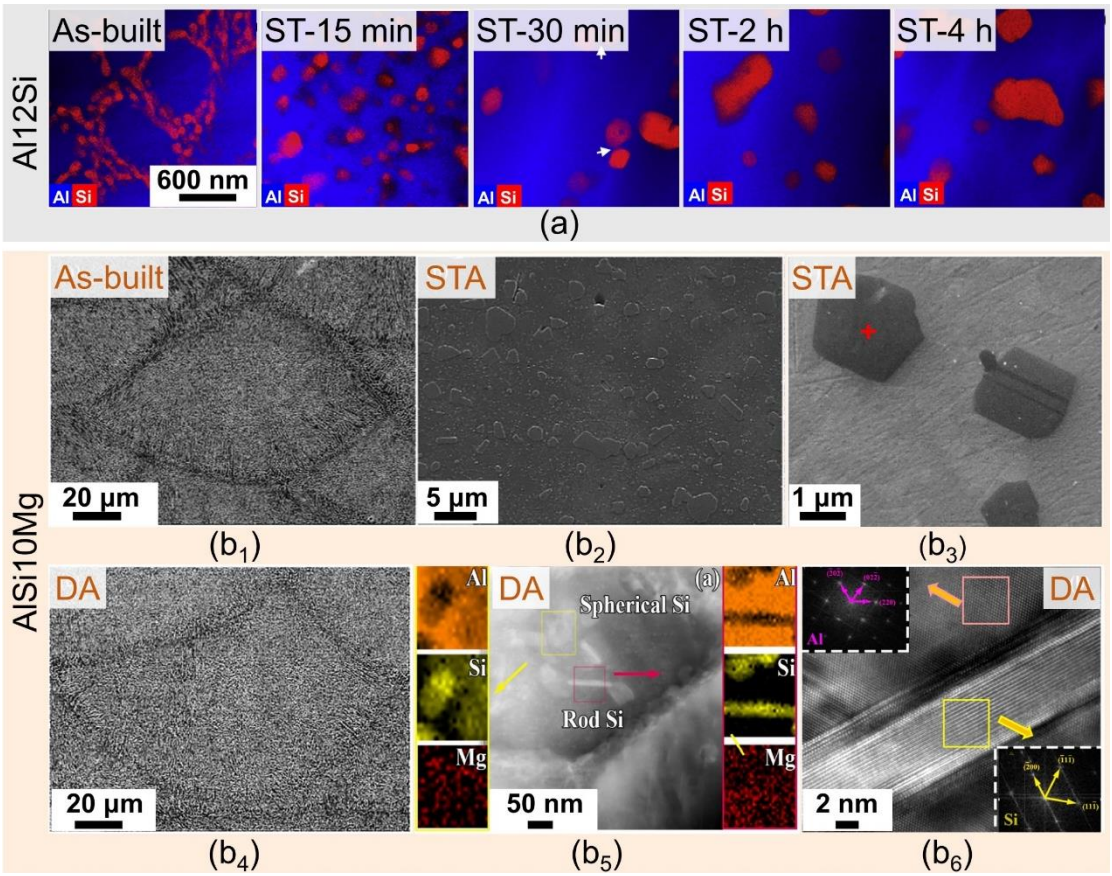

Fig. 14. Microstructure evolution of laser powder bed fusion Al–Si–(Mg) alloy under various heat treatment conditions. (a) Scanning transmission electron microscope-energy dispersive X-ray (STEM-EDX) maps of the Al and Si distribution in the Al−12Si alloy in the as-built and solution treatment conditions [111]. (b_1-b_3) Scanning electron microscopy images of AlSi10Mg in the as-built and solution treatment and aging (STA) conditions [114]. (b_4) Scanning electron microscopy image

showing coarse Si particles after direct aging [114]. (b_5) Formation of spherical and rod-shaped Si nano-precipitates after direct aging [115]. (b_6) The semi-coherent interface between the nano-sized precipitates and Al matrix [115].

4.2.2 Moderate- and high-strength Al alloys

L-PBF moderate- and high-strength Al alloys can be classified into two categories depending on whether the grains are refined. One kind is the alloys with sound printability whereby crack-free samples can be printed without composition modification, which are mainly Al–Cu [88,116] and Al–Mg [83] alloys. The other kind of alloys are assisted by grain refinement via inoculation treatment to heal the cracks. For the former, the alloys contain coarse columnar grains, while the latter usually exhibit multi-modal grain size distribution, including the coarse columnar grains and ultrafine equiaxed grains [90] or the complete formation of equiaxed grains [102].

For the former group without inoculation treatment elements, T6 (STA) treatment is the most common manner to tailor the microstructure and mechanical performance. During the heat treatment with a relatively high temperature, the fine-granular microstructure got coarsened [117]. However, the coarsening of grains is not significant due to the large population of coarse grains [116]. Subsequent aging is used to manipulate the precipitation in the L-PBF unmodified moderate- and high-strength Al alloys, such as the formation of Al_2CuMg in the Al–Cu–Mg alloy [118]. However, aging temperature and time significantly influence the precipitation behaviour [116]. Furthermore, it is found that the conventional HT profiles do not work well for the L-PBF alloys due to the loss of Cd. Thus, the heat treatment profiles need to be re-designed mainly owing to the composition variation caused by the high energy of the laser and the non-equilibrium microstructure caused by the high cooling rate during the L-PBF process.

For the latter group of Al alloys with inoculation treatment elements, the heat treatment profiles need to be intricately designed to achieve high performance. The STA is performed to trigger the precipitation of nano-sized precipitates for conventionally-

fabricated heat treatable Al alloys, such as the θ'', θ', and θ for Al–Cu alloys [116], β'' and β' for Al–Mg–Si [119], and η' for Al–Zn alloys [102]. Extending the STA to L-PBF high-strength Al alloys, the samples undergo the following microstructural variations: (1) the intermetallics are dissolved into the Al matrix; (2) inducing the precipitation and coarsening of secondary Al_3X particle; and (iii) leading to grain coarsening. The balance of these microstructural variations is sensitive to the ST temperature and dwelling time. A higher ST temperature and longer dwelling time can induce more significant dissolution of intermetallics into the matrix, the precipitation of secondary Al_3(Sc,Zr) particles with a larger size, and a more significant grain coarsening [102]. To circumvent the coarsening of grains and secondary Al_3X (X = Ti, Zr, or Sc) particles, DA performed at relatively lower temperatures is implemented to tailor the microstructure and mechanical properties for L-PBF medium- and high-strength Al alloys. Compared with the STA inducing significant grain growth (Fig. 15a_1,a_3), DA engenders an unobvious grain growth (Fig. 15a_1,a_2), and the precipitation of secondary Al_3Zr particles is observed [120]. The different trends of microstructure evolution between DA and STA have also been verified for the Zr-modified Al6061 alloy [119]. The secondary Al_3Zr particles precipitated after DA while nano-β"-Mg_xSi_y is the dominant precipitate after STA. However, the appropriate choice of DA temperature plays a significant role in influencing the mechanical properties through the different extensions of precipitate coarsening. Higher DA temperature leads to more obvious coarsening of secondary Al_3Sc particles for the L-PBF AlMnSc when DA temperature is increased from 300 °C to 450 °C (Fig. 15b_1-b_3) [121].

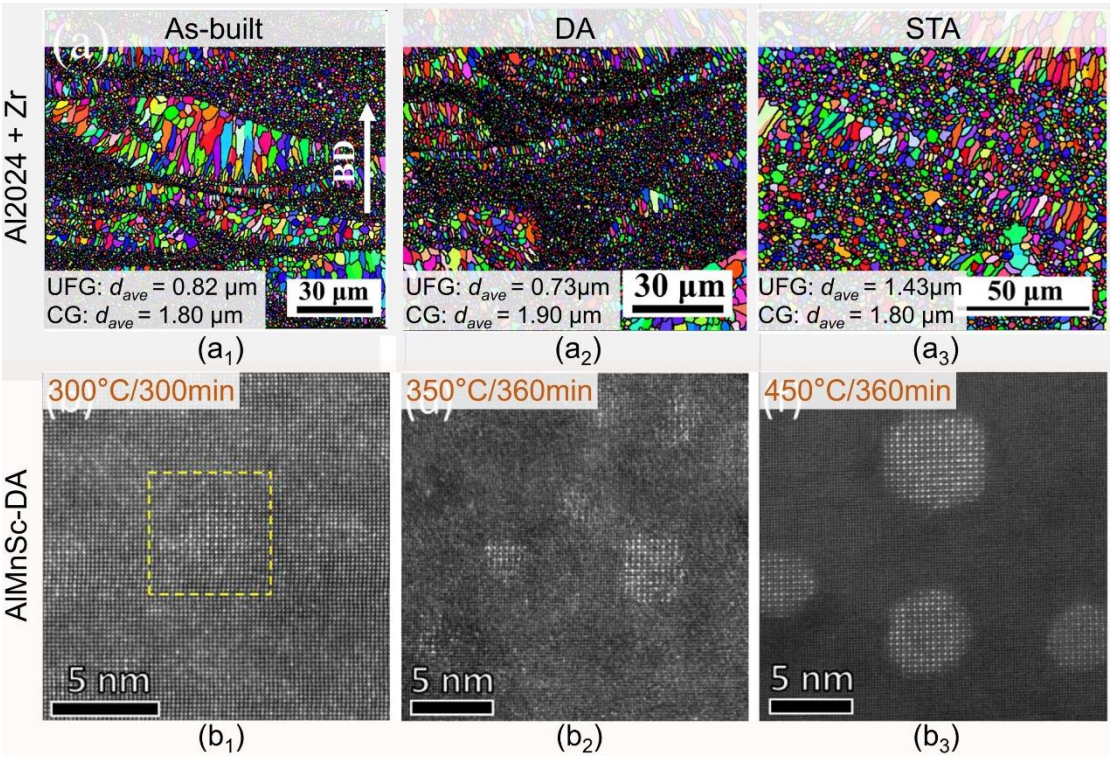

Fig. 15. Microstructure evolution of laser powder bed fusion high-strength aluminum alloys under various heat treatments. Electron backscattered diffraction (EBSD) map for the laser powder bed fusion Zr-modified AlCuMg alloy in the (a_1) as-built state, (a_2) direct aging (DA) state, and (a_3) solution treatment followed by aging (STA) state [120]. (b_1-b_3) High angle annular dark field scanning transmission electron microscopy (HAADF-STEM) images showing Al_3Sc particles [121]. The corresponding heat treatments are DA at (b_1) 300 °C for 300 min; (b_2) 350 °C for 360 min; (b_3) 450 °C for 360 min.

For the L-PBF moderate- and high-strength Al alloys with inoculation treatment particles, both DA and STA have been implemented to tailor the microstructure driven by high performance. DA is the mainstream method to tailor the microstructure of L-PBF Al–Mg–Si [119], Al–Cu [120], AlMnSc [121], and Scalmalloy® [122], where the secondary Al_3Sc is the major strengthening source. As for Al–Cu, Al–Mg–Si, and Al–Zn alloys, conventional STA engenders grain coarsening, the precipitation of secondary Al_3X particles, and strengthening phase [102]. A longer duration during the ST process on the one hand generates more dissolution of solute atoms into the matrix which is

beneficial for the subsequent aging process, but on the other hand coarsens the grains and secondary Al3X particles. The conflict arises and therefore the proper STA temperature and duration need to be studied. DA has also been used to process alloys to take advantage of precipitation from secondary Al_3X particles. As a result, the heat treatment profile needs to be intricately designed to achieve high performance.

4.3 Mechanical properties

4.3.1 Tensile property

(i) Unalloyed aluminum

As discussed in *Section 4.1.1*, work on the L-PBF unalloyed Al is relatively rare. The as-built unalloyed Al exhibits a low yield strength due to the lack of an effective strengthening path. Table A. 3 lists the tensile properties of L-PBF Al. The yield strength is about 75 MPa [64], which is higher than that of cast counterparts (about 50 MPa) [123], possibly arising from the refined microstructure of L-PBF sample.

(ii) Al–Si alloys

The Si plays an important role in the mechanical properties of L-PBF Al–Si alloys. The conventionally cast alloys normally exhibit limited ductility due to the localized shearing caused by the Si particles [124], contributing to the Orowan looping. The tensile properties of L-PBF Al–Si alloys in the as-built and heat-treated states are listed in Table A. 4. The tensile properties of L-PBF Al–Si alloys vary depending on a series of parameters, such as the printing parameters, printing strategy, printing conditions, heat treatment conditions, and testing directions.

As for the L-PBF Al–Si alloys, the strength is higher than that of cast counterparts due to the formation of refined Si phases. The yield strength of L-PBF AlSi10Mg is about 300 MPa, which shows an approximately 140% increment relative to that fabricated via spark plasma sintering and hot extrusion (Fig. 16a) [125]. The enhancement of yield strength also works well for the L-PBF Al−12Si alloy, with a yield strength of 186-300 MPa, which is higher than that of cast counterparts of about 104 MPa [126]. The

mechanical properties of L-PBF Al–Si alloys are affected by microstructure modification in terms of the fraction of melt pool boundaries, the size of the Si network and grains, and supersaturation and precipitation of Si particles. Decreasing the area fraction of melt pool boundaries via increasing hatch spacing effectively enhanced the tensile ductility from 7.2% to 9.8%, since melt pool boundaries have a higher tendency to form cracks and microvoids (Fig. 16b) [77]. Moreover, the samples printed with baseplate preheating exhibit a lower yield strength due to in-situ heat treatment (Fig. 16c), leading to the precipitation of supersaturated elements and a reduction of solid solution strengthening [127].

Composition modification, such as varying the stoichiometry or micro-alloying, is another frequently adopted approach to tailor the mechanical performance of L-PBF Al–Si alloys. Due to the tuneable printability and microstructure of L-PBF Al–*x*Si alloys (Fig. 7a-f) [71], Si plays a significant role in influencing mechanical properties. The Al–1.0Si and Al–2.0Si alloys fracture prematurely due to high crack density. The strength increased with Si content due to the better-defined web-like eutectic structure (Fig. 16d), which impedes the dislocation movement during deformation [71]. Apart from Si content, Mg content is another effective medium to tailor the mechanical performance of the alloy, due to its contribution of solid solution strengthening [80]. Through increasing content to 1.4 wt.%, the yield strength of L-PBF AlSi8.1Mg1.4 alloy is increased to 341 MPa, higher than that of AlSi10Mg (186-300 MPa) with a Mg content between 0.25-0.45 wt.%. Finally, the yield strength of L-PBF Al–Si alloy is tuneable via microalloying to trigger grain refinement and oversaturated solid solubility [128]. With the incorporation of Er into A357 alloy, the yield strength increases from 257 MPa (A357) to 296 MPa (AlSi7Mg0.6Er0.2) [128].

Due to the different thermal histories and formation of columnar grains along the build direction, the L-PBF Al–Si alloys show mechanical anisotropy [129]. The discrepancy exists for the mechanical anisotropy among different studies. Most studies (Table A. 4) indicated that the yield strength and ultimate tensile strength are higher for the

horizontal samples compared with those of vertical samples [129]. A typical example is L-PBF A357, where the yield strength in the horizontal direction (279.6 MPa) is higher than that in the vertical direction (232.2 MPa) for the substrate temperature of 35 °C (Fig. 16c) [127]. The anisotropy of tensile properties is attributed to the fraction of the melt pool boundary where the localization of pores, residual stress, and heat affected zone made it the weakest part. Horizontal samples with the lowest fraction of melt pool boundary exhibit higher strength. However, there are also some reports showing that the strength along the build direction is higher than that in the horizontal direction [130]. The higher yield strength of 300 MPa along the vertical direction relative to that of the horizontal direction (260 MPa) is ascribed to the nonuniform distribution of volume of eutectic microstructure and volumes with higher yield stress. The heat treatment is beneficial for microstructure homogenization and healing mechanical anisotropy.

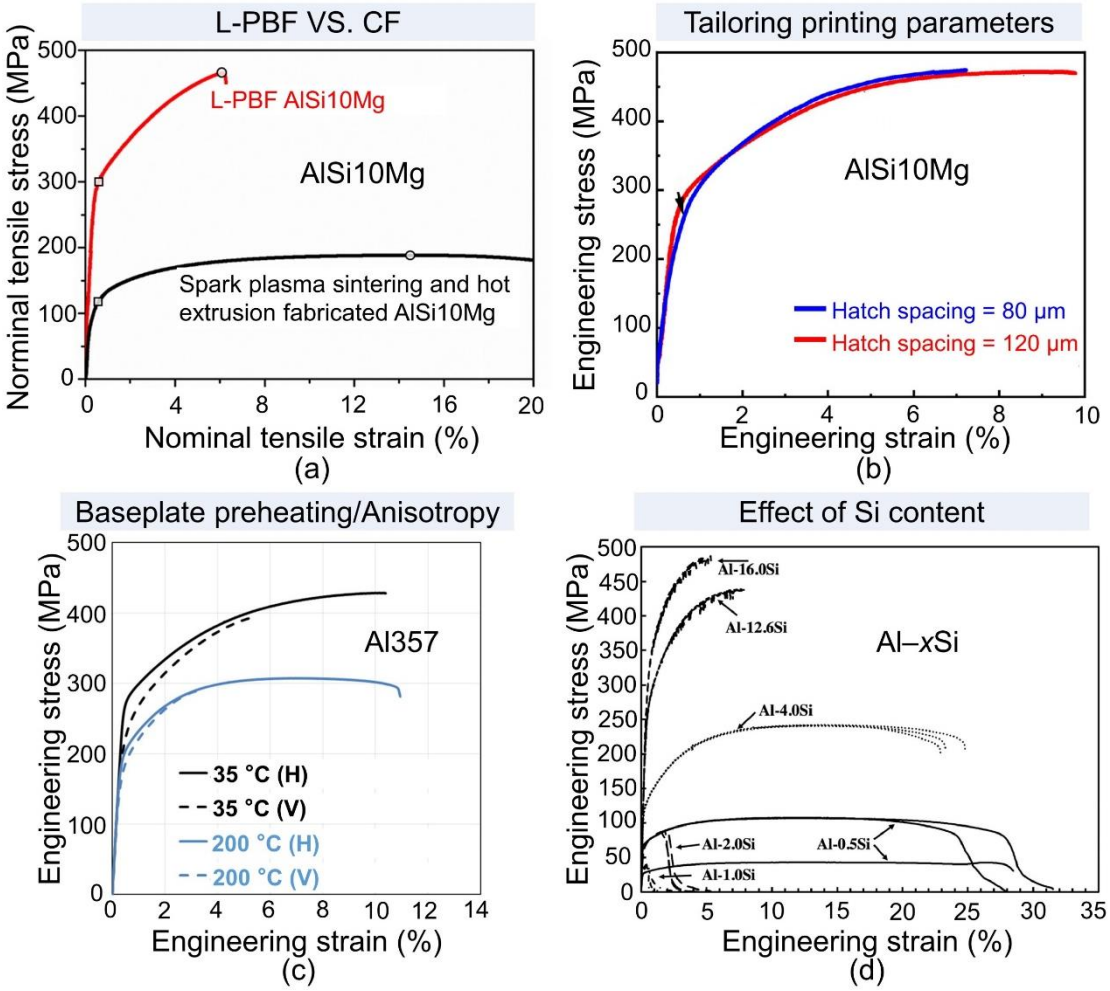

Fig. 16. Tensile properties of laser powder bed fusion Al–Si alloys. (a) Nominal

tensile stress-strain curves of the laser powder bed fusion and powder metallurgy fabricated AlSi10Mg alloy [125]. (b) AlSi10Mg alloys with different hatch spacing [78]. (c) A357 alloy under different baseplate temperatures and different directions (H: horizontal, V: vertical) [127]. (d) Al–*x*Si alloys [71].

As discussed in *Section 4.2*, the heat treatment profiles can significantly influence the microstructure evolution, which is directly associated with mechanical performance. The heat treatment effect on the mechanical properties of L-PBF Al–Si alloy is drawn as follows: (*i*) The direct aging (DA) temperature can tailor the mechanical performance in a broad range through controlling the size and volume fraction of precipitations, the cellular structures, and dislocation density. Geng et al. [80] reported that the yield strength increased after direct aging at 150 °C and 200 °C (Fig. 17a) due to the precipitation of β'' phase. However, when the DA temperature increased to 300 °C and 400 °C, the yield strength decreases and is lower than that of as-built counterparts (Fig. 17a) due to the disappearance of Si rich boundaries, the dissolution of Si and Mg, and a reduction of dislocation density. For L-PBF AlSi10Mg, the yield strength progressively decreased with increasing DA temperature due to decreased contribution from solid solution strengthening, dislocation strengthening, precipitation, and growth of Si particles [131]. In the meantime, the anisotropy of the tensile properties can effectively be alleviated via heat treatment due to a more homogenized microstructure after heat treatment arising from a more homogeneous microstructure. (ii) Compared with the broad tailoring of tensile properties, T6 heat treatment, including the solution treatment (ST) and artificial aging, leads to a disappearance of cellular structure, the coarsening of Si particles, and a reduction of dislocation density, generating a lower yield strength relative to that of as-built counterparts (Fig. 17b) [132].

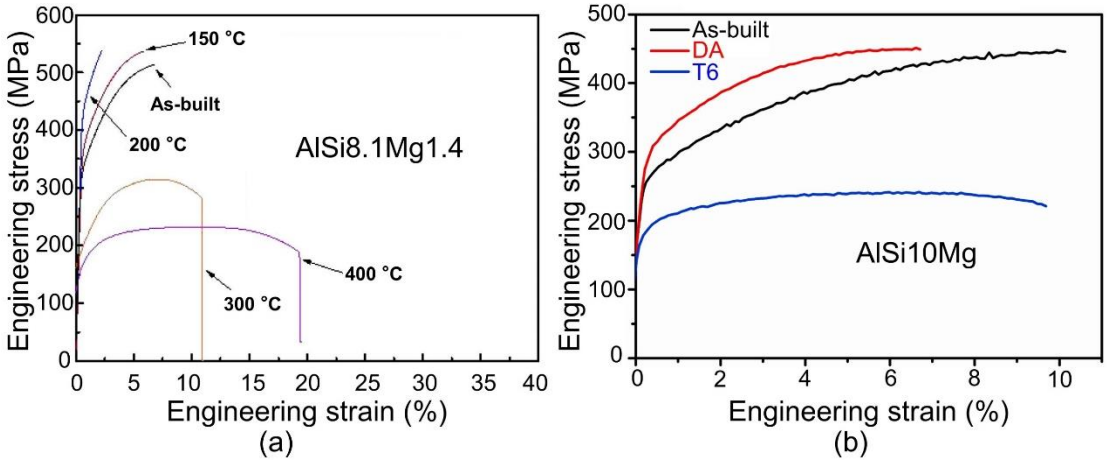

Fig. 17. Heat treatment effect on the tensile property of laser powder bed fusion Al–Si alloys. Effect of direct aging (DA) temperature on the tensile property of (a) AlSi8.1Mg1.4 alloy [80]; and (b) Effect of direct aging (DA) and T6 heat treatment on the tensile property of AlSi10Mg [132].

(iii) Moderate- and high-strength aluminum alloys

The mechanical property values for the L-PBF moderate- and high-strength Al alloys, including the Al–Cu, Al–Mn, Al–Mg, Al–Mg–Si, and Al–Zn alloys, are listed in Table A. 5. The tensile properties of L-PBF Al alloys are sensitive to the microstructure which is controlled by the printing parameters, tensile direction, detailed chemical composition, and heat treatment conditions. For the L-PBF moderate- and high-strength Al alloys, the inoculation treatment eliminates the crack on the one hand, and contributes to the strengthening and mechanical isotropy on the other hand.

As for moderate- and high-strength Al alloy with sound L-PBF printability, mainly the Al–Cu alloy [133], the L-PBF Al alloy exhibits higher yield strength relative to that of cast counterparts due to grain refinement, as manifested by the AlCu5MnCdVA [133]. For the inoculation-treated Al alloys with refined grains, the inoculation treatment elements also contribute to the strengthening apart from refining grains. Firstly, the yield strength is significantly enhanced contributed by grain boundary strengthening, as manifested by the L-PBF Al–4.47Cu–1.95Mg–0.55Mn alloy (Fig. 18a), whose yield strength increased from 253 MPa to 446 MPa with the addition of 2 wt.% Zr [134].

Secondly, the strength of L-PBF compositionally modified moderate- and high-strength is higher than that of cast or wrought counterparts due to grain refinements and precipitation strengthening, as manifested from L-PBF Al5083 [83] and Al6061 alloys [119]. Taking the L-PBF Al5083 alloy modified with 0.7 wt. % for example, the yield strength can reach 318.7 MPa, which is higher than that of Al5083-O (145 MPa) [83]. Furthermore, for the Sc- and Zr- modified moderate- and high-strength Al alloys, the Sc and Zr can contribute to the precipitation strengthening from secondary $Al_3(Sc,Zr)$ particles after heat treatment [135]. The yield strength of a Sc- and Zr- modified Al–Mn–Sc alloy increases to more than 550 MPa after direct aging from 438 MPa in the as-built state (Fig. 18b) [135]. The precipitation of secondary $Al_3(Sc,Zr)$ particles can make the conventionally non-heat treatable Al–Mg alloys become heat treat hardenable. The yield strength of L-PBF AlMgScZr alloy increased from 338 MPa to 512 MPa after direct aging [136].

Moreover, post heat treatment profiles play a significant role in influencing the microstructure and mechanical properties by influencing the coarsening of grains, size, and volume fraction of $Al_3(Sc,Zr)$ particles. For the DA heat treatment, higher DA temperature and longer dwelling time lead to coarsening of secondary $Al_3(Sc,Zr)$ particles, reducing the yield strength [121]. Opprecht et al. [119] have reported that the DA is more effective in enhancing the yield strength for the Zr-modified Al6061 alloy than conventional STA, since the grains and secondary $Al_3(Sc,Zr)$ particles undergo significant coarsening during STA. As for the STA heat treatment, a higher solution treatment temperature and longer dwelling time trigger more complete dissolution of intermetallics into the matrix in conjunction with coarsening of grains and $Al_3(Sc,Zr)$ particlesL-PBF AlZnMgCuScZr alloy for example [102]. Through the optimization of heat treatment profiles, the yield strength of L-PBF AlZnMgCuScZr alloy can reach more than 640 MPa [102]. The above results indicate that the heat treatment profiles need to be carefully designed to achieve high performance for the L-PBF moderate- and high-strength Al alloys.

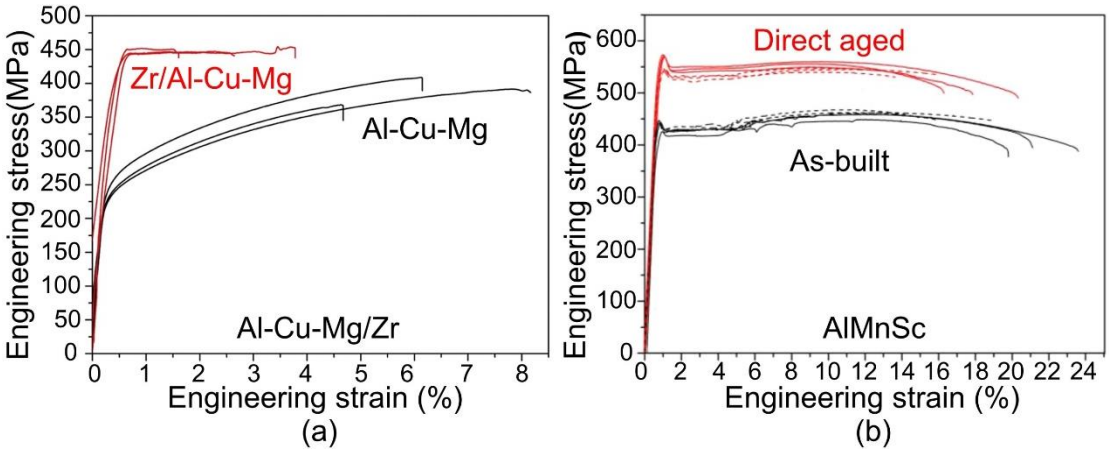

Fig. 18. Tensile properties of laser powder bed fusion moderate- and high-strength aluminum alloys. (a) AlCuMg/Zr alloy [134]. (b) AlMnSc alloy [135].

Apart from eliminating cracks and enhancing mechanical performance, the formation of equiaxed grains is also beneficial for mechanical isotropy, since there is no preferred grain orientation for the ultrafine equiaxed grains (Fig. 18b) [135]. In addition, the introduction of the ultrafine equiaxed grains contributes to enhancing the strength and altering the deformation behaviours [102,135,136], including the Lüders band as reflected by the deformation plateau after yielding in the stress-strain curves (Fig. 18a,b). The ultrafine grain boundaries serve as dislocation sinks and enhance dynamic recovery, triggering the formation of the Lüders band. The serrated flow was due to the dynamic strain aging caused by the interaction between the solute Mg atoms and mobile dislocations during the tensile test [102].

4.3.2 High cycle fatigue, fatigue crack growth, and fracture resistance

(i) Al–Si alloys

As the most prominent cause of structural failure in load-bearing components, fatigue properties, such as high cycle fatigue, fatigue crack growth, and fracture toughness, are critical for practical applications. The high cycle fatigue property of L-PBF Al–Si alloys is closely correlated with the test directions [137] and microstructures [132,138]. For L-PBF AlSi10Mg, the fatigue strength drops as the building angle increases. The 0° built specimens exhibit higher fatigue strength than those of 45° and 90° specimens due

to smaller defects and denser melting pool boundaries (Fig. 19a) [137]. Aside from the build direction, the microstructure variation induced by HT also effectively tailors the fatigue properties [132]. Similar to the tensile strength, the fatigue properties were affected by the morphology and size of Si particles. The DA sample exhibited superior fatigue properties due to the maintenance of the cellular structure and precipitation of fine Si particles. In contrast, the T6 sample exhibited the worst fatigue properties due to the disappearance of cellular structure and coarsening of Si particles. (Fig. 19b).

Fracture toughness, defining the damage tolerance of a material, is critical for industrial applications, yet is scarcely studied for L-PBF Al–Si alloys [77,139]. The fracture toughness of L-PBF Al–Si alloy normally lies in the range of 40–60 MPa$\sqrt{m}$, typically higher than that of cast Al–Si counterparts [77]. The fracture toughness is influenced by the printing parameters and strategy, such as varying the layer thickness, hatching space, scanning strategy, sample orientation, and crack direction of the C(T) samples [139]. The melt pool morphology and the mesostructure controlled by the scanning strategy dominated the fracture. The crack initiation toughness and crack propagation resistance are higher when the melt pool mesostructure makes the crack propagation more tortuous.

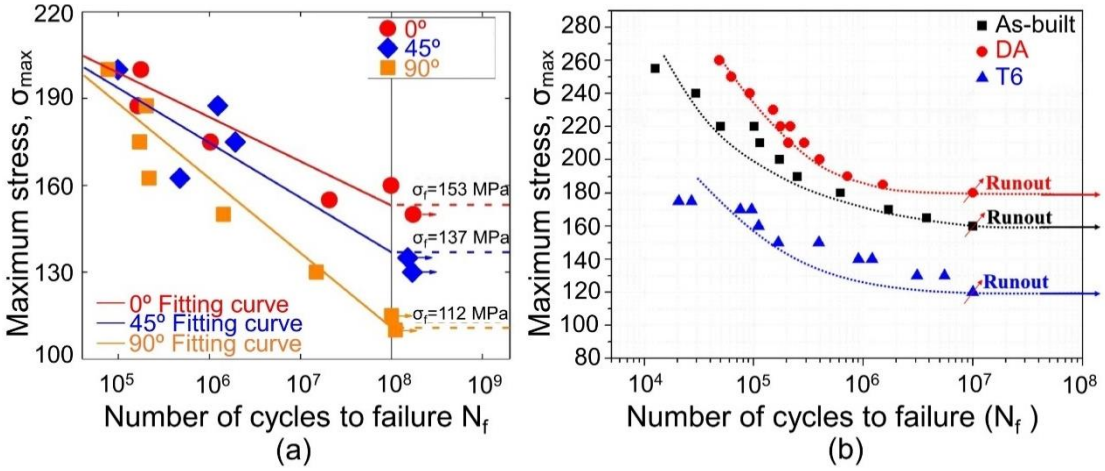

Fig. 19. Fatigue and fracture toughness of laser powder bed fusion Al–Si alloys. Stress amplitude-cycles to failure (S-N) curves of laser powder bed fusion AlSi10Mg samples (a) along the 0°, 45°, and 90° [137]. (b) under as-built, direct aging (DA), and T6 conditions [132].

(ii) Moderate- and high-strength Al alloys

Until now, investigations into high cycle fatigue, fracture toughness [140], and crack growth behaviour [141] of L-PBF moderate- and high-strength Al alloys have been limited. The high cycle fatigue property is sensitive to the testing directions and microstructure variation induced by heat treatment. Heat treatment can effectively tailor the microstructure and the resultant cycle fatigue strength. The 10^7 cycles fatigue strength of L-PBF Al5024+Sc/Zr is 75 MPa, 105 MPa, and 90 MPa, respectively, for the as-built (AB), hot isostatic pressing (HIP) processed, and overaged (OA2) samples (Fig. 20a$_1$), which show a positive correlation with the yield strength [142]. Furthermore, significant anisotropy of fatigue strength exists for L-PBF AlMgScZr sample due to the lack of fusion defects, which engender a higher stress concentration in the V samples than that of H samples, and thus a higher fatigue strength (100.5 MPa) for the horizontally built (H) sample relative to that (57 MPa) of vertically built (V) samples (Fig. 20a$_2$) [122]. For the fracture toughness study, Wang et al. [140] have reported a K_{IC} value of 25.4 MPa·m$^{1/2}$ and 23.2 MPa·m$^{1/2}$ for the horizontal and vertical L-PBF AlMgScZr samples, respectively (Fig. 20b$_1$). The lower fracture toughness for the vertical samples is due to less tortuous crack propagation along the molten-pool boundaries, which reduced propagation resistance. The combination of yield strength and toughness is comparable to those of Al7075–T651 (Fig. 20b$_2$).

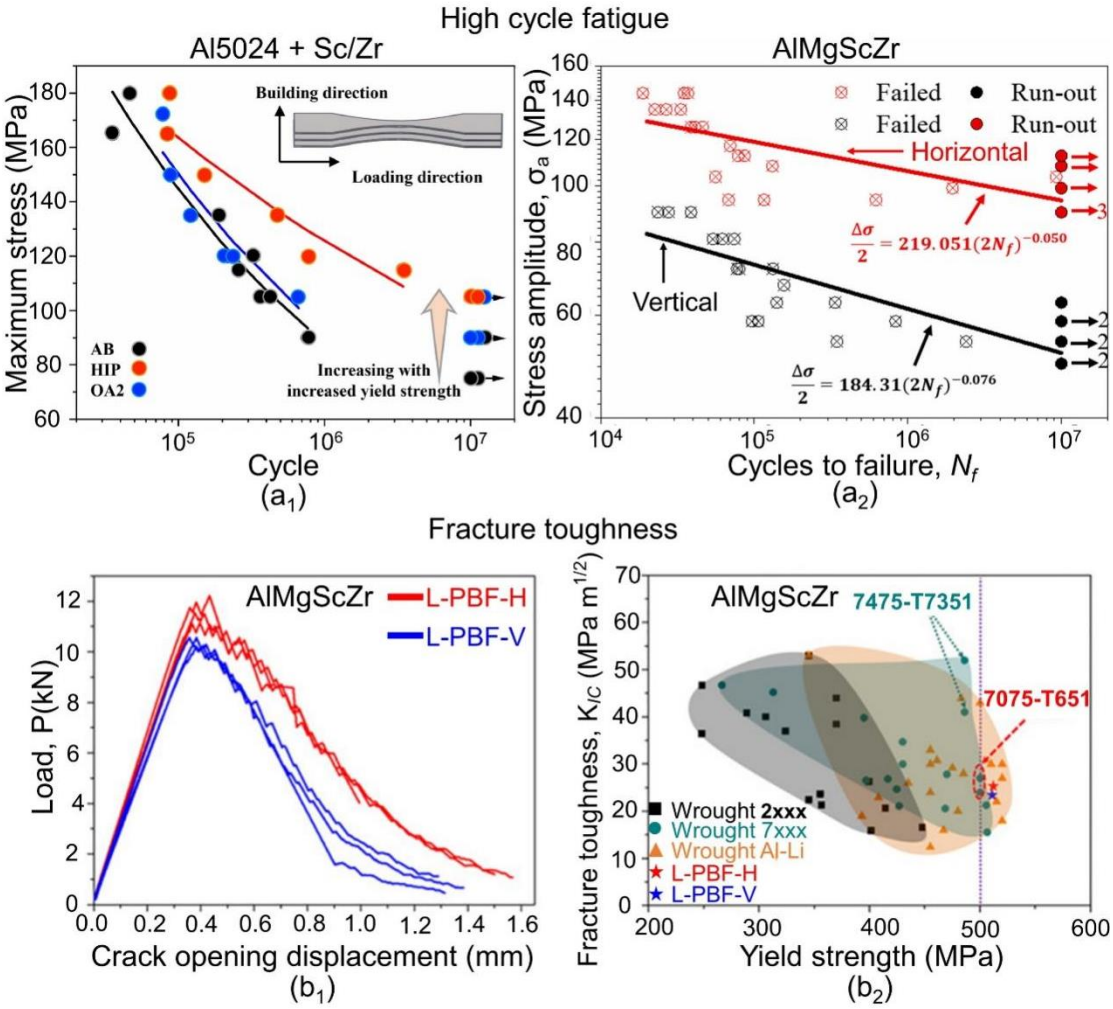

Fig. 20. Fatigue and fracture toughness of laser powder bed fusion high-strength aluminum alloys. (a_1) High cycle fatigue property of Sc/Zr-modified Al5024 alloy under as-built (AB), hot isostatic pressing (HIP), and over aging (OA2) conditions, respectively [142]. (a_2) Stress amplitudes-cycles to failure (S-N) curves of laser powder bed fusion Al–Mg–Sc–Zr alloy in horizontal and vertical directions [122]. (b_1) Load-crack opening displacement (COD) curves of the laser powder fusion AlMgScZr alloy [140]. (b_2) Comparison of strength and fracture toughness of the laser powder bed fusion AlMgScZr alloy compared with those of 2xxx, 7xxx, and Al-Li wrought alloy [140].

4.4 Corrosion properties

4.4.1 Al–Si alloys

Due to the special microstructure, such as refined grains compared with those of

conventionally-fabricated counterparts and microstructure heterogeneity, the corrosion property of L-PBF Al alloys deserves investigations to pave the way for industrial application. The results hitherto indicated that the Si shell plays a significant role in influencing the corrosion property. The L-PBF Al−12Si possesses a better corrosion resistance than that of cast counterparts in the NaCl solution [70] in terms of a lower weight loss rate, a lower corrosion current density, $i_{corr,\ L\text{-}PBF}$ (0.36 ± 0.03 μA cm^{-2}), and higher pitting potential, $E_{pit,\ L\text{-}PBF}$ (-0.69 ± 0.01 V) (Fig. 21a). The different corrosion behaviours are explained based on the different eutectic silicon particles. For the cast Al−12Si, micro-scale silicon particles triggered the formation of macro-galvanic couples, where eutectic silicon particles serve as micro-cathodes and the aluminum substrate serves as the anode. What is more, the large-sized eutectic silicon particles increase the fluctuation of oxide film, forming a porous oxide layer, which causes Cl^- to erode the Al matrix. In contrast, the ultrafine eutectic silicon particles trigger the formation of micro-galvanic couples, facilitating the formation of $Al(OH)_3$ in the early stage and subsequent dehydration into a compact Al_2O_3 protective film. Thus, the ultrafine silicon particles in the L-PBF Al–Si alloys can stabilize the oxide layers and prevent the aluminum substrate from being further eroded. The obstruction of oxide front caused by the more finely distributed silicon is also validated for the L-PBF AlSi10Mg alloy [143]. In addition, the L-PBF Al−12Si alloy exhibits anisotropic corrosion behaviours along the XY-plane and XZ-plane are observed for [144]. The XZ-plane exhibits a better corrosion resistance relative to that of the XY-plane, as supported by the lower corrosion current density, $i_{corr,\ L\text{-}PBF}$ (0.16 ± 0.02 μA cm^{-2}), and higher pitting potential, $E_{pit,\ L\text{-}PBF}$ (-0.65 ± 0.02V) for the XZ-plane (Fig. 21b). The enhanced corrosion resistance is supported by the surface morphology after the polarization experiment (Fig. 21c,d). The entire pitting process is observed on the XY-plane, where the oxide film is damaged by the Cl^- (Fig. 21c). However, no obvious pitting holes are observed on the XZ-plane (Fig. 21d). The anisotropy of corrosion property is due to different morphology of Si shells. The circular Si shells with a cellular morphology and a large depth on the XY-plane are beneficial for the corrosion products

to continuously grow and break the shells. In contrast, the shallow Si particles with columnar morphology on the XZ-plane are not conducive for the growth of corrosion products. Thus, the exposed Si shells and oxide film on the XZ-plane can prevent the Al matrix from being further eroded.

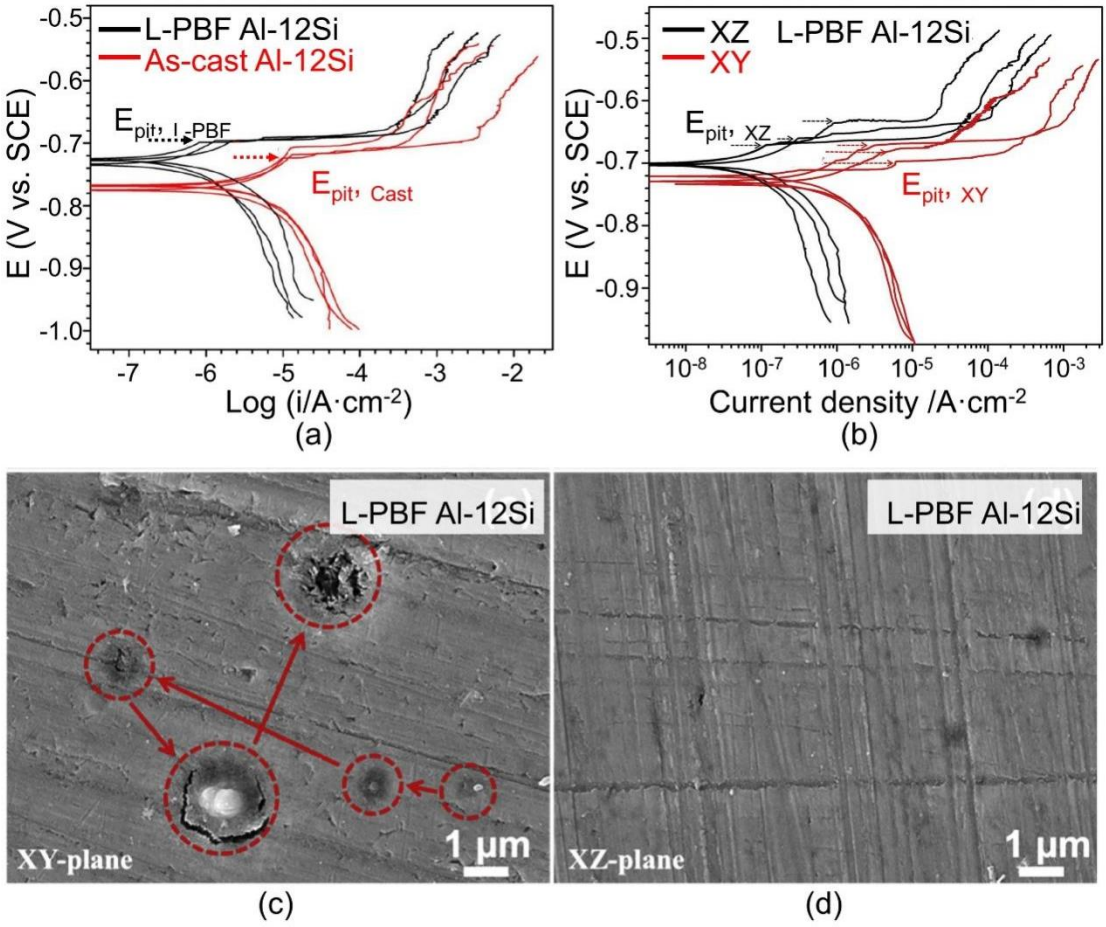

Fig. 21. Corrosion property of laser powder bed fusion Al–Si alloys. (a) Potentiodynamic polarization curves of the laser powder bed fusion Al–12Si and as-cast Al–12Si alloy in the aerated 3.5 wt.% NaCl solution [70]. (b) Potentiodynamic polarization curves of the XY- and XZ-planes for the laser powder bed fusion Al−12Si alloy in the aerated 3.5 wt.% NaCl solution [144]. Scanning electron microscopy images showing the morphology after polarization experiments in the aerated 3.5wt.% NaCl solution for the laser powder bed fusion Al−12Si sample on the (c) XY-plane and (d) XZ-plane [144].

Since the Si cells play a significant role on the corrosion property for L-PBF Al–Si

alloys, the heat treatment that alters the Si network can influence the corrosion property [145]. Rubben et al. [146] further found that the Si network can hinder the propagation of corrosion, and thus resulting in a superficial corrosion spreading around the melt pools boundary. In contrast, for AlSi10Mg sample without Si network after heat treatment, the corrosion propagates in depth which results in a more deeply penetrating corrosion attack, since it is not hindered by the Si network. Meanwhile, the corrosion attacks occurred initially at the melt pool boundaries where the potential difference between Al and Si phases is larger, which provides a larger driving force for galvanic coupling. Finally, the surface conditions can significantly influence corrosion resistance. The as-built AlSi10Mg sample shows lower corrosion resistance as compared to that of polished samples due to different passive film properties. On one hand, polishing can remove the oxide film formed during L-PBF, and a film more resistant to the chlorides is formed. On the other hand, polishing can reduce the surface roughness and potential sites for pitting initiation and surface conditions [145].

Based on what has been reviewed, the cellular structure with Si particles decorating along the cell boundary and the melt pool boundary play a critical role in influencing the corrosion properties of L-PBF. The ultra-fine Si particles can prevent the Al substrate from being further eroded due to enhancement in the stability of oxide layer, leading to the enhanced corrosion resistance relative to that of cast counterparts. The different morphologies of Si cells also lead to corrosion anisotropy for the XY-plane and XZ-plane of L-PBF Al−12Si sample.

4.4.2 Moderate- and high-strength Al alloys

The corrosion properties of L-PBF moderate- and high-strength Al alloys are critical for engineering applications, which has attracted research interest recently [147-149]. The study of corrosion properties has been conducted from different perspectives, such as the corrosion mechanism [148], corrosion anisotropy [148], and heat treatment effects [150]. For the inoculation treated Al alloys with equiaxed grains, it is found that the addition of Zr can improve the corrosion resistance of AA5083 alloy with a

significant decrease of pitting (Fig. 22a), which is attributed to the refined grains resulting in efficient passivation with a more stable oxide layer [151]. Due to different microstructures, including precipitation behaviours, grain size distribution, and crystallographic orientation, along the XY- and XZ-planes, the Sc- and Zr-modified Al−Mg alloys exhibit corrosion anisotropy [148]. The XY-plane exhibits a better corrosion resistance with a lower current density than that of the XZ-plane. In contrast, the XZ-plane shows a better resistance for pitting initiation (Fig. 22b). At the initial stage of the corrosion process, passive films including $Al(OH)_3$ and Al_2O_3 formed on the XY- and XZ-planes. The refined grain size and high grain boundary density lead to faster formation of an oxide film on the XZ-plane. In contrast, the dominated (111) crystallographic along the XY-plane promotes the easier formation of initial pits, causing a lower value of E_{pit} on the XY-plane. Subsequently, the $Al_3(Sc,Zr)$ particles serve as local cathodes and facilitate the dissolution of the Al matrix. Due to the higher fraction of $Al_3(Sc,Zr)$ particles on the XZ-plane, the pit propagation is quicker than that on the XY-plane, leading to deep pits on the XZ-plane. Based on what has been discussed, the corrosion resistance of L-PBF Al alloys is closely correlated with the microstructure, thus, heat treatment modifying the metastable microstructure can significantly influence the corrosion resistance. For the Sc- and Zr-modified moderate- and high-strength Al alloys, the corrosion resistance is tunable depending on the heat treatment profiles. The corrosion resistance is decreased after direct aging at 325 °C for 4h for the L-PBF Al–Mg–Si–Sc–Zr alloy (Fig. 22c) due to the formation and coarsening of secondary $Al_3(Sc,Zr)$ precipitations [150]. This is due to the fact that the Al matrix near the precipitates could act as the anode and was corroded preferentially [152]. However, the dependence of corrosion resistance of L-PBF Al–Mg–Sc–Zr on heat treatment is also influenced by the size and spacing of precipitates. Direct aging at 325 °C for 1 h and 4 h reduces the corrosion resistance for L-PBF Al–Mg–Sc–Zr alloy, however, the corrosion resistance is enhanced when further direct aged for 12 h and 120 h due to the increased size and spacing of grain boundary precipitations [153].

In total, the L-PBF moderate- and high-strength Al alloys with ultrafine grains exhibit higher corrosion resistance relative to their cast counterparts. Due to different precipitation behaviours, grain size, and texture, the XY-plane and XZ-plane show different corrosion behaviours. Moreover, corrosion resistance is sensitive to heat treatment conditions, which tailors the size and spacing of precipitates.

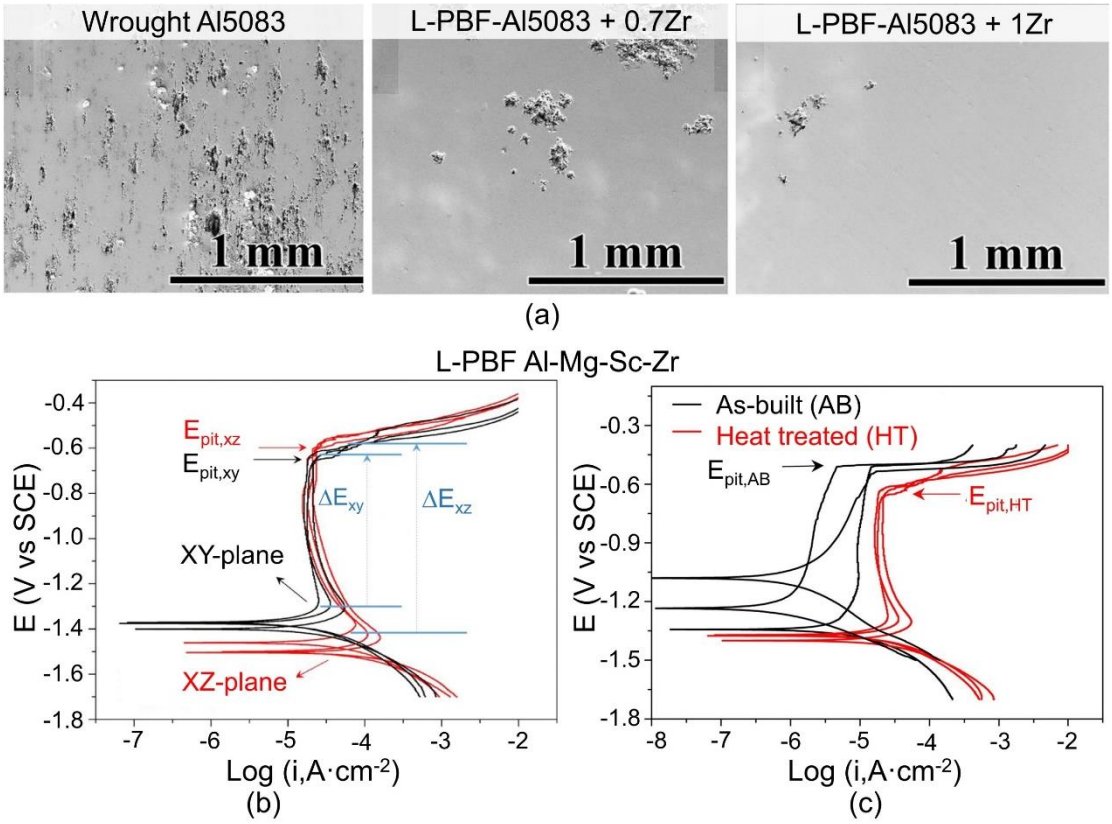

Fig. 22. Corrosion property of laser powder bed fusion moderate- and high-strength aluminum alloys. SEM image of the (a) AA5083, AA5083 + 0.7Zr, and AA5083 + 1 Zr alloys after 168 h in 3.5 wt.% NaCl [151]. (b) Potentiodynamic polarization curves for the XY- and XZ-planes of laser powder bed fusion AlMgScZr alloys in 3.5 wt.% NaCl solution [148]. (c) Potentiodynamic polarization curves for the as-built and heat treated AlMgScZr alloys in 3.5 wt.% NaCl solution [150].

4.5 Elevated temperature applications

Developing Al alloys for moderate-temperature applications has been a longstanding issue and has significance for industrial applications, such as partial replacing Ti alloys to reduce weight and cost [154,155]. However, for the typical high-strength Al alloys,

the potent strengthening precipitates get coarsened or dissolve into the matrix, limiting their elevated applications [156]. Comparatively, nickel-based superalloys can remain mechanically stable at temperatures exceeding 75% of their absolute temperatures. Analogously, the service temperature would be about 425 °C if taking the melting temperature of Al of 660 °C as the benchmark. This indicates that there is still much space for improving the high-temperature mechanical performance of Al alloys. In consideration of the necessity and potential improvement space, much work has been conducted to develop Al alloys for high-temperature applications. The common approach to this is the introduction of a thermally stable phase. There are three different routes to develop Al alloys targeted for elevated temperature applications [155]: (*i*) introducing thermally stable strengthening precipitates, such as the typical $L1_2$-structured Al_3X (X = Zr or Sc) particles [157]; (*ii*) introducing a high volume fraction of intermetallics, such as Al–Fe [158], Al–Ce [159,160], Al–Ni [161], and so on; and (*iii*) introducing thermal resistant ceramic particles, such as oxides, carbides, nitrides, and borides. As to the high-temperature Al alloys fabricated by the AM technologies, work has been conducted from the above-mentioned perspectives. We will focus here on the previous two subgroups and the last group of Al alloys with thermally stable ceramic particles will be discussed in *Section 6* on the AM of Al matrix composites (AMCs). The mechanical properties of some developed high temperature Al alloys are listed in Table A. 6. The dependence of σ_y and σ_{UTS} on testing temperature is shown in Fig. 23. The mechanical properties of L-PBF AMCs are also listed in Table A. 6 and Fig. 23 for benchmarking. Based on the plot, it can be seen that when the testing temperature is higher than 200 ˚C, only the A2024-RAM and Al–6Fe–5Cr exhibit higher yield strength than that of AA8009. What is more, there is still a broad opportunity space for improvement when the strength of Al alloys with the specific strength of Ti6Al4V is benchmarked. We will describe the high-temperature mechanical properties from three different perspectives, including Al–Si, thermally stable strengthening precipitates, and the high volume fraction of intermetallics, in turn.

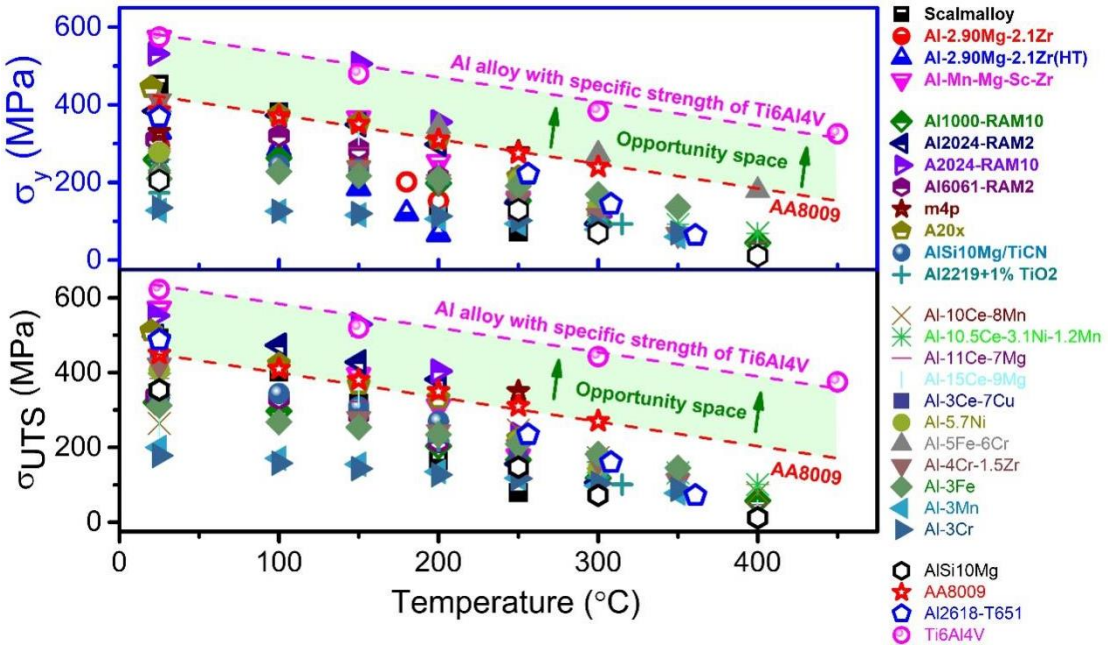

Fig. 23. The dependence of (a) yield strength, and (b) ultimate tensile strength for the laser powder bed fusion aluminum alloys and conventionally fabricated aluminum alloys, including the AA8009 and 2618–T651. The strength of aluminum alloys with the specific strength of Ti6Al4V alloys is also shown for comparison. The data of Scalmalloy® is taken from Ref. [162], Al–8Ce–10Mg is taken from Ref. [159], Al–11Ce–7Mg and Al–15Ce–9Mg is taken from Ref. [160], Al–10Ce is taken from Ref. [163], Al–3Ce–7Cu is taken from Ref. [164], Al–10Ce–8Mn is taken from Ref. [162], Al–5.7Ni is taken from Ref. [161], Al–7.5Ni, Al–7.5Ni–0.5Cu and Al–7.5Ni–2.0Cu is taken from Ref. [165], Al–3Ni–1Ti–0.8Zr is taken from Ref. [166], Al–5Fe–6Cr is taken from Ref. [167], Al–4Cr–1.5Zr is taken from Ref. [168], Al–3Fe, Al–3Mn, Al–3Cr is taken from Ref. [169], 2618–T651 is taken from Ref. [170], AA8009 is taken from Ref. [171], and AlSi10Mg is taken from Ref. [172].

4.5.1 Al–Si alloys

For the Al–Si alloy, the investigation of high-temperature mechanical behaviours is limited [172,173]. Due to a lack of high temperature strengthening phase, the strength decreased significantly at higher temperatures. Due to coarsening of the eutectic solidification structure, the yield strength decreased from 138 ± 3 MPa (tested at room temperature) to 114 ± 4 MPa (tested at 200 °C) for the L-PBF Al−12Si sample [173] and

decreased from ~204 MPa at room temperature to about 70 MPa at 300 °C for L-PBF AlSi10Mg alloy [172]. The significant drop of strength at higher temperatures limits the high temperature applications of L-PBF Al–Si alloys [174].

4.5.2 Thermally stable strengthening precipitates

For the thermally strengthening precipitates, the typical alloys are Scalmalloy® [175] or the Addalloy® [11,176]. Following on from these, Sc and Zr modified Al–Mg–Si [97,101] and Al–Zn alloys [102] have been developed. However, investigations into the high-temperature mechanical properties of the developed alloys have scarcely begun. The present preliminary investigations indicated that the as-built and as-aged AlMgZr samples show a lower yield strength, which is 87 MPa and 24 MPa at 260 °C, respectively (Fig. 24a) [176]. The lower yield strength for the aged sample is due to the coarsening of grain-boundary precipitates, decreasing their ability to inhibit grain boundary sliding of the fine equiaxed grains. Furthermore, for the creep property test, it was found that the fitting value of n = 2 (Fig. 24b_2) or n = 3 (Fig. 24b_3) is better than n = 1 (Fig. 24b_1) when the Mukherjee-Bird-Dron power-law equation was used to fit the creep rate vs. stress curve. The n = 2 or n = 3 values correspond to the grain boundary sliding or dislocation motion during creep, respectively [176].

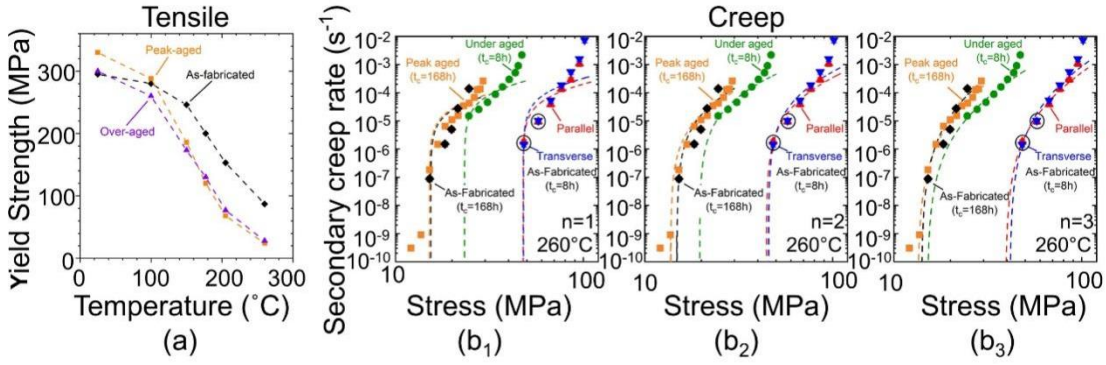

Fig. 24. High temperature tensile and creep property of laser powder bed fusion AlMgZr alloy. (a) Dependence of yield strength on the testing temperature of the laser powder bed fusion AlMgZr alloy. (b_1-b_3) Double logarithmic plot of secondary creep rate vs. stress for creep testing at 260 °C of AlMgZr alloy in three conditions: as-fabricated, under aged (260 °C, 168 h), peak aged (400 °C, 8 h) [176].

4.5.3 High volume fraction of intermetallics

Deriving from the rapidly solidified Al alloys consisting of a high volume fraction of intermetallics with high coarsening resistance [177], high volume fraction intermetallic Al alloys have been developed, which are mainly based on the near-eutectic alloy composition. The developed Al alloys can be categorized into several systems, including Al–Ce alloys [159-162], and Al–TM alloy [161,166,169,178], where TM denotes a transitional metal, such as Fe, Ni, Cr, or Mn.

(i) Al–Ce

The Al–Ce-based Al alloys with the eutectic structure are a typical high temperature alloy for L-PBF, showing a strong hot-tearing resistance [179]. The low solubility of Ce in the Al matrix makes it coarsening resistant at elevated temperatures [180]. The L-PBF Al–Ce–Mn alloy exhibited a heterogeneous structure with the intermetallics of $Al_{20}Mn_2Ce$, $Al_{11}Ce_3$, and Al_6Mn (Fig. 25a) [162]. At room temperature, it exhibited a lower yield strength (~252 MPa) compared with that of Al2618 (~369 MPa) and Scalmalloy® (~453 MPa). However, the strength of L-PBF Al–Ce–Mn is higher than AlSi10Mg and Scalmalloy® and comparable relative to that of Al2618 starting from 150 °C to 400 °C, signifying its excellent strength retention ability at high temperatures [162].

(ii) Al–TM (*TM = Fe*, *Ni*, *Cr*, or *Mn*)

The transition metals (TM), such as Fe, Ni, Mn, and Cr, are commonly incorporated into the Al alloy to enhance the elevated-temperature tensile properties due to several factors: (1) the low maximum solid solubility of TMs in Al; (2) the formation of coarse resistant intermetallics; and (3) the low diffusion coefficient of TMs in the Al. Thus, the Al–Ni alloy system [181], Al–Fe [182], Al–Mn [169], Al–Cr [169] all show potential elevated-temperature applications. It is reported that the L-PBF Al–5Fe–6Cr alloy exhibits a heterogeneous distribution of precipitates in the interior of melt pools and along the grain boundary (Fig. 25b) [167]. Due to the formation of nanoscale icosahedral and intermetallic phases, the as-built Al–5Fe–6Cr exhibited a high yield

strength of 344 MPa at 200 °C, which is higher than that of AA8009 [171]. Furthermore, the yield strength of 273 MPa is the highest for the reported values for L-PBF Al alloy tested at 300 °C.

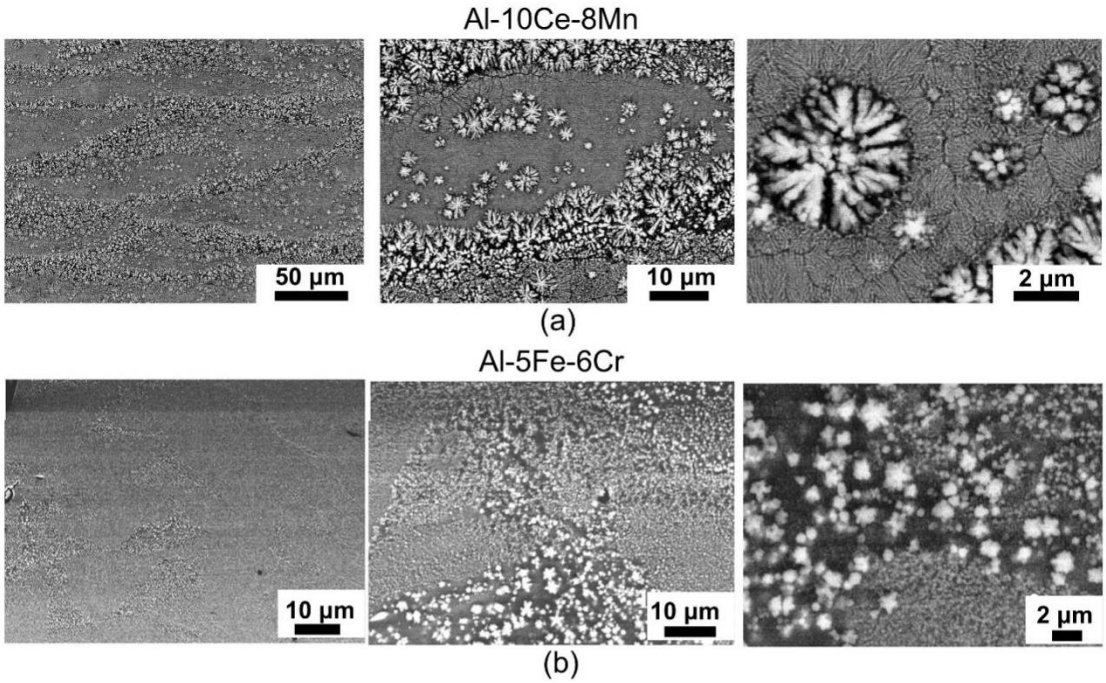

Fig. 25. Scanning electron microscopy images showing the heterogeneous multiscale microstructure of laser powder bed fusion aluminum alloys. (a) as-built Al–Ce–Mn sample [162]. (b) as-built Al–5Fe–6Cr samples [167].

Based on what has been discussed so far, for the L-PBF Al alloys containing thermally stable precipitates, the microstructure stability is not comparable to that of cast counterparts, and there are still many opportunities to overcome this by the composition modification inspired by the literatures of cast counterparts. As to the Al alloys by means of high volume fraction of intermetallics, the preliminary results show that they can potentially show promise as high temperature Al alloys. However, future work needs to be conducted through the tailoring of composition, printing parameters, and the evaluation of other high-temperature mechanical properties (such as creep, fatigue, and fracture toughness) beyond the tensile properties.

4.6 Effect of powder feedstock and degradation on quality

4.6.1 Powder characteristics on the microstructure and mechanical properties

The printing quality of the L-PBF samples depends on various factors, such as the powder feedstock, printing environment, and printing parameters. As the starting materials for printing, the powder feedstock plays an important role in influencing the quality of the printed samples, such as the printability [183], densification [184], and tensile property [185]. The common powder characteristics include powder morphology, density, flowability, spreadability, and chemical composition (Fig. 26). The powder morphology includes particle size distribution, satellites, sphericity of powders, aspect ratio, and agglomeration of powders, while the density of powders can be reflected using the apparent density, packing, and bulk density. Furthermore, Archimedes' density reflecting the internal porosity of powders is also used to reflect powder quality. In addition, the chemical composition, including the content of trace elements, oxides, impurities, and moisture, can also influence the phase formation, microstructure, and mechanical properties of printed samples. Finally, the rheology of powders including flowability, recoatability, and spreadability, influences the powder packing behaviour during L-PBF.

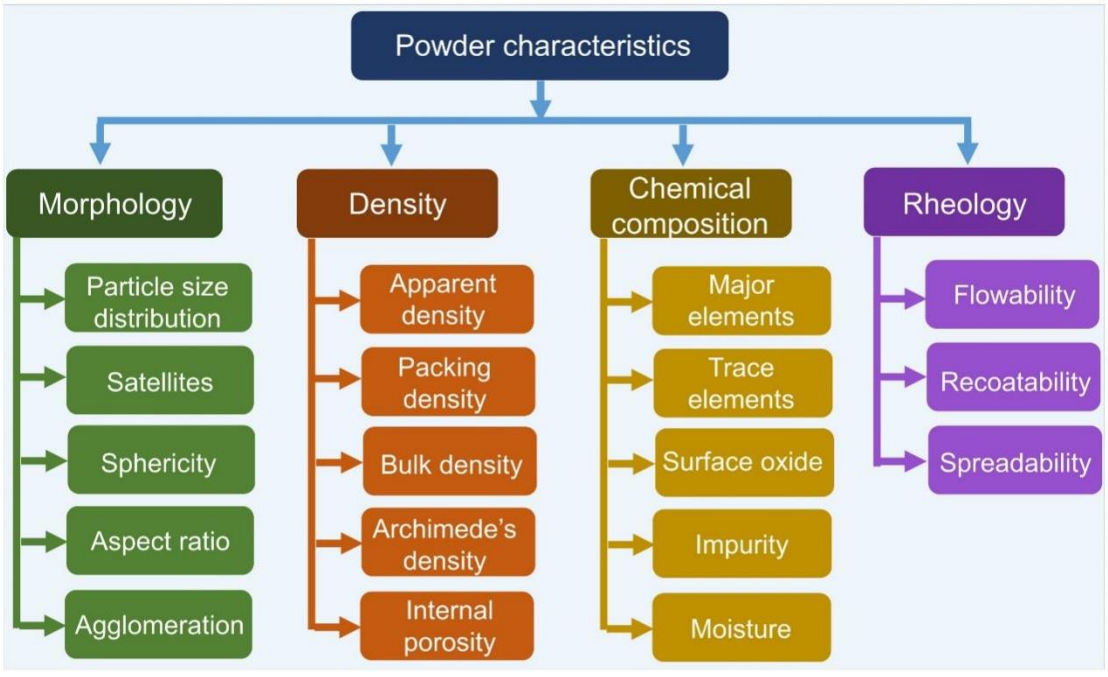

Fig. 26. Powder characteristics that are used to reflect the powder quality.

The powder characteristics play a critical role in the densification and mechanical properties of L-PBF Al alloys. The powder feedstock characteristics (particle size distribution and morphology) (Fig. 27a_1-a_4) of AlSi10Mg powders can significantly influence the flowability, which is in inverse relationship with the avalanche angles [185]. Coarse powders with spherical particle morphology show the lowest avalanche angles, and thus the best flowability (Fig. 27b_1). Furthermore, Laser absorption increases with the increased fraction of fine-sized particles and more irregular-shaped powders by forming a larger amount of beam trap (Fig. 27b_2). Moreover, the samples printed with the plasma atomized powders yield significantly improved surface quality and a higher fraction of fine powders leads to a rougher surface (Fig. 27b_3). This is due to the fact that the finer particles adhere more to the melt pool than coarser and heavier powders. Due to the different flowability and laser absorption, plasma atomized powders (B1) lead to the fabrication of samples with the highest relative density (99.98-99.99 %). The finest powders (A2) show the lowest relative density (99.84-99.87 %) (Fig. 27b_4). On the basis of densification, the plasma atomized powders (B1) engender higher ultimate tensile strength and elongation (Fig. 27b_5,b_6), ascribing to the higher relative density for the samples printed with B1 powders. Comparatively, the B1 powder-fabricated samples exhibit a lower yield strength, which might be associated with the chemical composition.

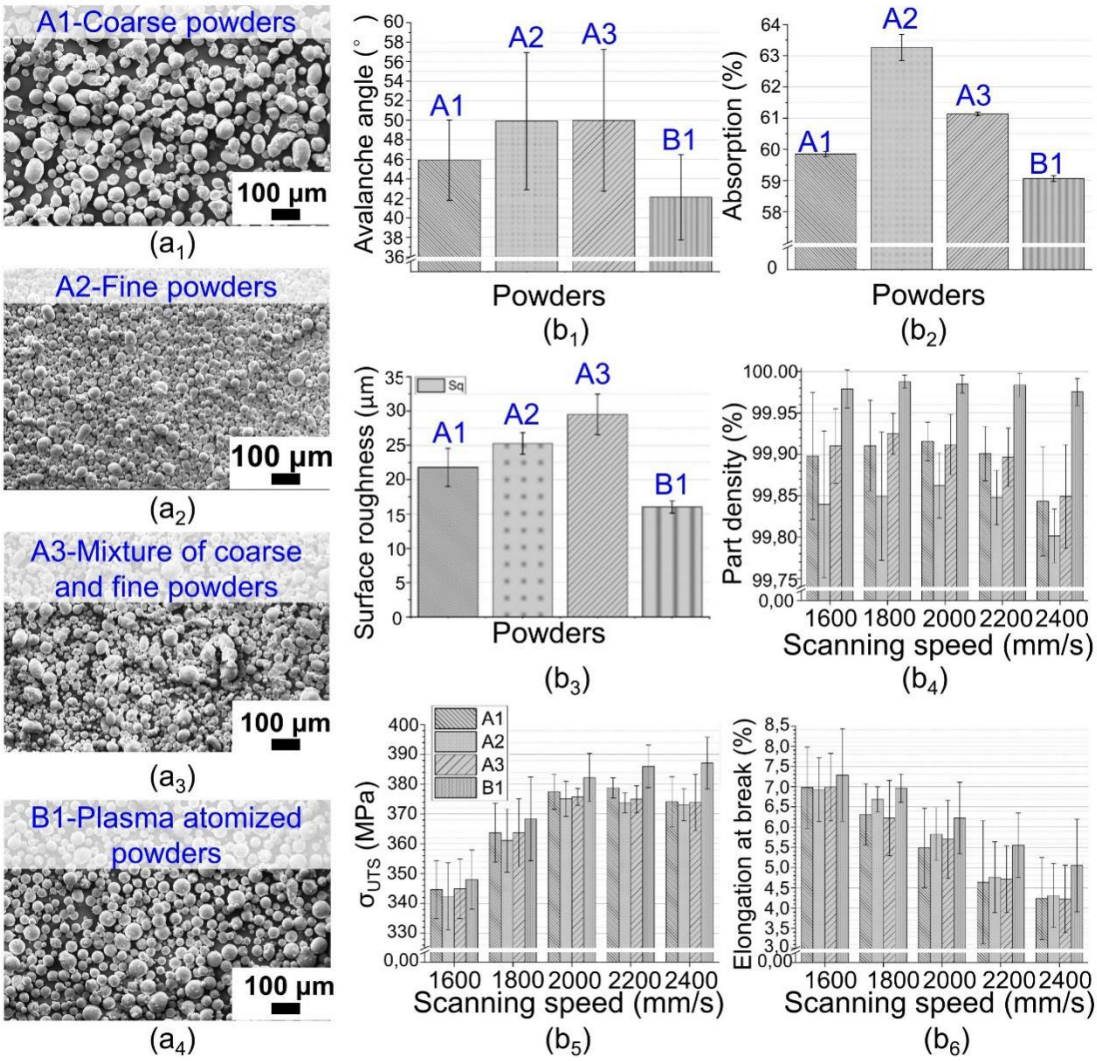

Fig. 27. Dependence of powder characteristics on the printing quality and tensile property of laser powder bed fusion AlSi10Mg alloys [185]**.** Scanning electron micrographs of the aluminum powders (a_1) A1: coarse powders; (a_2) A2: fine powders; (a_3) A3: mixture of coarse and fine powders; (a_4) B1: plasma atomized powders. (b_1)–(b_6) show the avalanche angle, absorption, surface roughness, part density, ultimate tensile strength (σ_{UTS}), and elongation at break.

Apart from the powder morphology and particle size distribution, the moisture skin attached to the powder surface degrades densification by forming Al oxides and hydroxides. Thus, drying powders is beneficial for densifying the printed samples by removing moisture, which has been verified by L-PBF Al−12Si [186]. The effect of moisture on printability is due to the following facts. On the one hand, the moisture on

the powder surface could suppress flowability [187]. On the other hand, the moisture can react with Al by forming Al_2O_3, and hydrogen is entrapped in the melt [188]. This indicates that it is necessary to bake the Al powders to remove the moisture to enhance printability.

4.6.2 Powder reuse on the powder characteristics and quality of printed Al alloys

To maximize the powder use for AM to ensure lower waste and reduce cost, powder reuse is often adopted during AM fabrication [189]. However, the powder characteristics might undergo degradation after reuse, which can influence the printability and quality of printed samples. Currently, the effect of powder reuse on AM has been conducted for various materials [190], such as steels, Ni-based superalloys, and Ti alloys. Principally speaking, the degradation of powders is ascribed to the variation of powder characteristics (Fig. 26) and the associated mechanical properties. Fig. 28 summarizes the variation of powder characteristics and mechanical properties with powder reuse for L-PBF Al alloys.

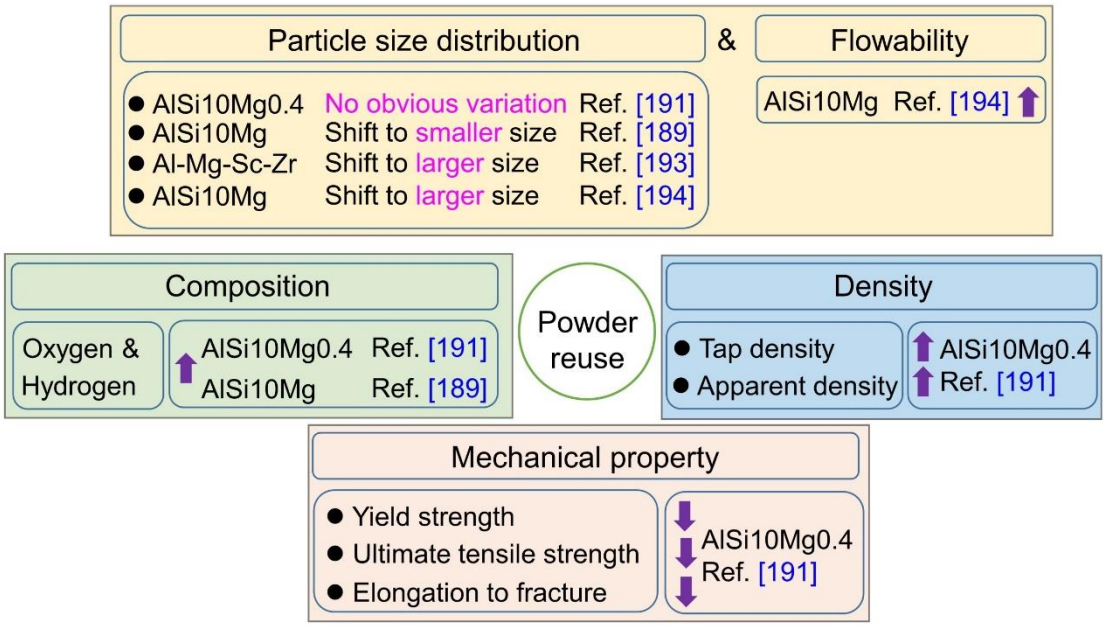

Fig. 28. Evolution of powder characteristics after reuse based on the published literature. The up and down arrows represent the increase and decrease, respectively.

One of the significant factors for chemical composition variation is the oxygen content

due to oxidation during L-PBF, especially when considering the high oxygen affinity of Al alloys. The work reported hitherto indicated that the oxygen content increased progressively due to the fact that the oxygen in the chamber can oxidize the molten spatter particles [191,192]. Fig. 29a_1,a_2 show the SEM images of the virgin AlSi10Mg powders and reused AlSi10Mg powders for 30 months. Bright oxidized powders as shown by the red circles are detected for the reused powders [189]. Fiegl et al. [191] further reported that the oxygen content follows a logarithmic function with aging time and the oxide layer thickness increased. The oxygen content increased from 0.052% (virgin powders) to 0.123% (reused powders for 30 months), as listed in Table A. 7. In conjunction with the increase of oxygen content, the hydrogen content generally increased after reuse, as indicated for the AlSi10Mg0.4 alloy [191,192] (Table A. 7 and A. 9).

Apart from the composition variation, other powder characteristics also undergo variations. (1) For the particle size distribution (PSD), its evolution is different depending on the materials and processing methods used. Fiegl et al. [191] have reported a near similar PSD for the AlSi10Mg0.4 powder after reuse (Table A. 7). In their experiment, the virgin powders are added continuously to the system to ensure that the total weight of powders is ~550 Kg. Thus, the as-investigated powders in their experiment are a mixture of powders aged for different times after manufacturing [191]. Comparatively, a shift of PSD to higher particle size after reuse has been reported for the Al–Mg–Sc–Zr [193] and AlSi10Mg alloys [194]. The shift of PSD to larger particle size is due to the fact that smaller particles will melt and sinter to form satellites. In contrast, Raza et al. [189] have reported the shift of PSD to a smaller size, which is ascribed to the removal of agglomerated particles. (2) As for the tapping and apparent density for the reused powders, a marginal increase in tapping and apparent density was reported (Table A. 7) [191]. However, the detailed mechanism was not given. This could be ascribed to the removal of fine powders resulting a better flowability. (3) Furthermore, powder reuse can cause other variations of powders, such as a lower fraction of satellites (Fig. 28b_1,b_2) and a higher fraction of spatters [189]. The removal

of satellites is due to powder sieving and friction between particles during transportation into the machine. The increased fraction of spatters with reuse is due to the formation of oxides.

The evolution of powder after reuse, such as the composition, particle size distribution, and flowability, may directly influence the printing quality and corresponding mechanical properties. With the increase of oxygen content, oxide layer thickness, and spatters, the porosity level was increased. The AlSi10Mg0.4 samples printed using the powders for reused 30 months exhibited about 3.0% porosity level (Fig. 28c$_1$) compared to that of 0.7% (Fig. 28c$_2$) printed using the virgin powders [191]. An increased porosity level was also observed for the L-PBF Al–Mg–Sc–Zr alloy, where the porosity level increased from 0.06 ± 0.01% for the samples printed with virgin powders to 0.15 ± 0.01% for the samples printed with reused powders [193]. However, the effect of powder reuse on the mechanical properties of as-printed samples varies among different research studies. For the L-PBF AlSi10Mg0.4, the as-printed samples using the powders reused for 30 months exhibit a simultaneously decreased yield strength, ultimate tensile strength, and elongation to fracture (Table A. 8) relative to those printed using virgin powders, due to the higher fraction of porosity level. In contrast, the L-PBF Al–Mg–Sc–Zr alloy does not exhibit a significant drop in strength and ductility, as shown in Table A. 8.

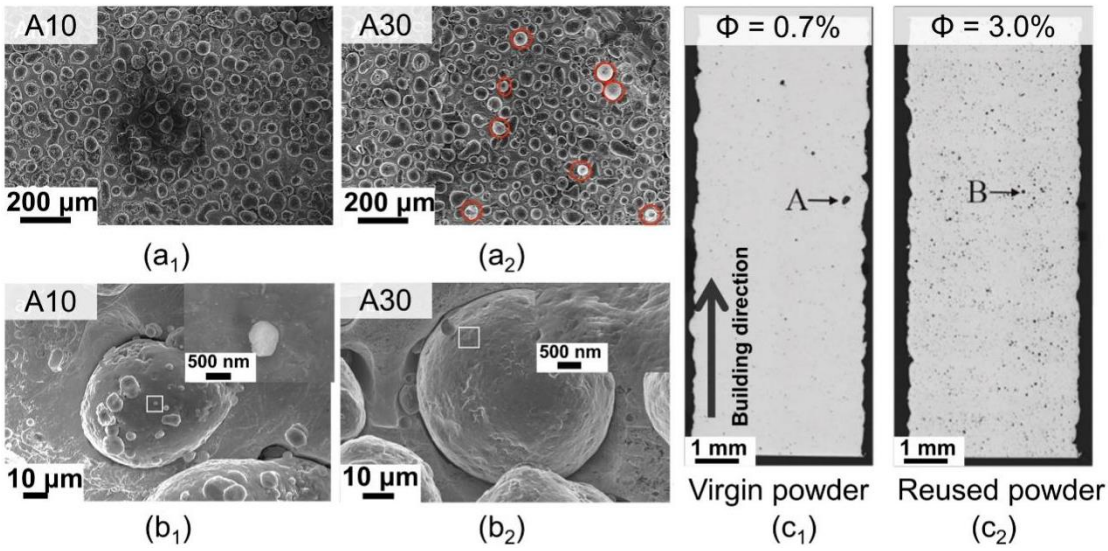

Fig. 29. Powder reuse effect on the powder characteristics and printing quality of laser powder bed fusion aluminum alloy. Scanning electron microscopy images of (a_1) virgin powders and (a_2) reused powders for 30 months [189]. The red circles represent the bright oxidized particles in the reused powders. Surface morphology of (b_1) virgin powders and (b_2) reused powders for 30 months [189]. (c_1) and (c_2) show the optical microscopy (OM) images of the laser powder bed fusion AlSi10Mg0.4 samples using the virgin powders and reused powders, respectively [191].

4.7 Oxidation and element evaporation

During the interaction between the laser and powders, oxidation and element evaporation are often encountered due to the high temperatures the melt pool experiences [195,196]. Oxidation and evaporation play a significant role in the processability and mechanical properties of L-PBF Al alloys. Two kinds of oxides, namely, larger, micron-sized oxides formed due to oxidized vapor or spatter, and smaller, sub-micron oxides originating from the native oxide film, were reported for L-PBF AlSi10Mg [197]. The larger particles are generally associated with the pores. This is due to the fact that oxides can prevent the consolidation of the molten alloy. Thus, oxidation has been considered as a disadvantage, leading to poor processability of Al alloys. The oxidation behaviour is dependent on the printing atmosphere and, in turn, influences the mechanical properties. A higher atmospheric oxygen leads to a higher fraction of oxides and lower ductility for the L-PBF AlCu5MnCdVA alloy [198].

To date, work on the accurate oxygen content as measured by inert gas fusion-infrared absorption spectrometry or Instrument Gas Analyzer (IGA) is still limited. Through IGA analysis, it is found that the oxygen content of L-PBF Al, Al−12Si, and AlSi10Mg alloys is reduced [195] (Fig. 30). Similar oxygen removal after L-PBF was also reported for L-PBF Al [61], in which the oxygen content decreased from 1637 ppm to 1241 ppm after L-PBF. This has challenged the notion that in-situ oxidation occurs and deteriorates the L-PBF printability of Al alloys. during L-PBF. The oxygen removal is

explained by the evaporation of nano-sized solid oxide particles, which consists of the fracture and the spallation of surface oxide layer during core melting of Al (Fig. 30b$_1$-b$_3$), the transfer of nano-sized oxides from the centre of the melt pool to the surface, preventing in-situ oxidation via buoyancy force (Fig. 30b$_4$) and thermocapillary force (Fig. 30b$_5$), and the evaporation of nano-sized oxides during L-PBF (Fig. 30b$_6$) and the subsequent track (Fig. 30b$_7$,b$_8$). The decrease in oxygen content after L-PBF does not necessarily rule out the possibility of in-situ oxidation and can be explained by the competition of evaporation of oxidation and in-situ oxidation.

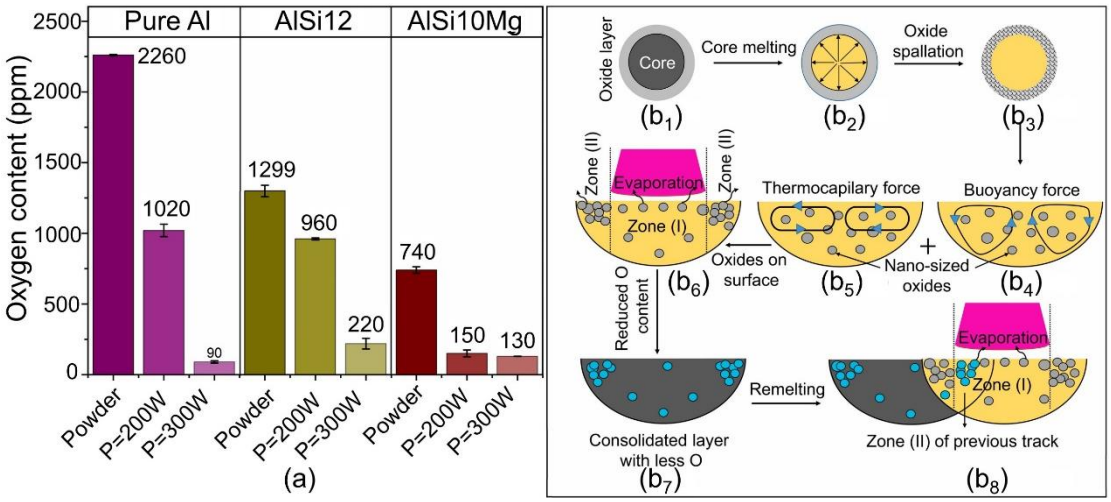

Fig. 30. Evolution of oxygen content in the powders and as-printed aluminum samples [195]**.** (a) The oxygen content (mass ppm) of the starting powders as well as the laser powder bed fusion pure Al, AlSi12, and AlSi10Mg parts. (b$_1$-b$_8$) The schematic graph showing the oxygen removal during the laser powder bed fusion process.

Another issue that needs to be taken into consideration is the element evaporation during L-PBF of Al alloys that contain elements with high evaporation pressure, such as Zn and Mg [199,200]. Fig. 31a shows the equilibrium vapor pressure of some elements at different temperatures [200]. Zn and Mg possess high equilibrium vapor pressure and selective evaporation could occur for Al alloys including such elements. This has been confirmed for a variety of Al alloys processed with L-PBF, such as the Al–Mg–Si and Al–Zn alloys, as shown in Fig. 31b, where the content of Mg/Zn is presented for the powders and printed samples.

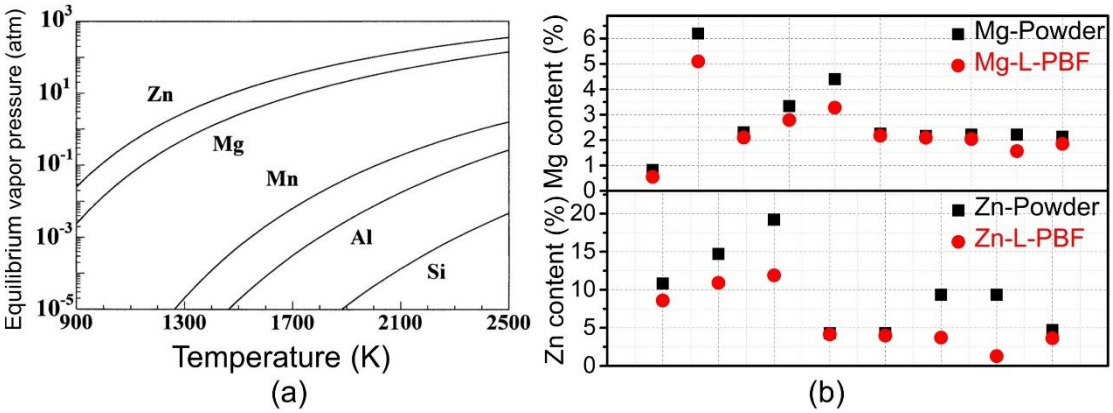

Fig. 31. Equilibrium vapor pressure of metals at different temperatures and evaporation of Mg and Zn during laser powder bed fusion aluminum alloys. (a) Equilibrium vapor pressure of metals at different temperatures [200]. (b) The evaporation of Mg and Zn in the laser powder bed fusion aluminum alloys. The data are cited from Ref. [173,195,196,201-203].

The element evaporation of Mg and Zn can influence the printability and mechanical properties of L-PBF Al–Zn alloys [204]. On the one hand, higher Mg and Zn content would lead to a higher crack susceptibility [90]. Thus, the printing parameters favouring severe evaporation of Mg and Zn, such as higher laser power and lower scanning speed, lead to enhanced processability with fewer cracks [204]. On the other hand, as the major strengthening elements in the Al–Zn alloys [205], a lower concentration of Mg and Zn leads to less nano-precipitation strengthening after heat treatment. Hence, there exists a contradiction between the evaporation of Mg/Zn and the mechanical properties of the alloys. It is important to balance the elimination of cracks and the maintenance of strengthening due to the evaporation of Mg and Zn during L-PBF Al–Zn alloys.

4.8 Advantages and limitations of laser powder bed fusion

As discussed in *Section 2.2*, L-PBF technology boasts the advantages of higher dimensional accuracy and design freedom, which makes it suitable for fabricating geometrically complex parts, such as components with an internal cooling channel. However, this method has some limitations. Due to the fast cooling rate and resultant steep thermal gradient, the moderate- and high-strength Al alloys tend to form cracks,

which has hindered broad application. Though the design of novel L-PBF-specific Al alloys can overcome these issues to some extent and has pushed this technology forward, there is still some way to go ahead to certify the materials and processes to ensure quality, reproductivity, and reliability before they enter the arena for practical industrial application [2].

5. Fabrication of aluminum and aluminum alloys via other technologies

5.1 Laser powder direct energy deposition of aluminum alloys

LP-DED exhibits several advantages in terms of higher deposition rate and the capability of cladding/coating or repairing [39], yet it suffers from the disadvantages of lower forming accuracy and complexity [206,207]. At present, there are numerous attempts to fabricate Al alloys via LP-DED, including the Al–Si [208], Al–Cu [209], Al–Mn [210], Al–Mg [211], and Al–Fe–Cr alloys [212].

Heterogeneous microstructure across multiscale, either in the melt pools or along the build direction, was reported for the LP-DED Al alloys. Due to the heterogeneous solidifications dynamics in the melt pools, LP-DED Al–Si alloy exhibits a heterogeneous gradient microstructure in terms of evolution of cellular dendrite in the previous layer to the heat-affected zone (HAZ) and finally to the dendritic microstructure in the new layer (Fig. 32a) [213]. The evolution of solidification morphology is due to the solidification velocity and thermal gradient. The melt pool boundary, where the thermal gradient is high and solidification velocity is low, favours the formation of columnar dendrites. With the decrease of thermal gradient and increase of solidification velocity towards the melt pool center, the cellular dendrite is favoured [208]. Apart from the heterogeneous microstructure in the melt pool, a heterogeneous microstructure, transiting from cellular to columnar dendrite and finally to equiaxed dendrite along the build direction, was also observed [214]. The microstructure

evolution was ascribed to the decreased cooling rate along the build direction, resulting in coarser secondary dendrite arm spacing and lower hardness towards the top of the sample. As for grain orientation, it is closely correlated with the melt pools affected by the processing parameters and alloy systems. Both the equiaxed and columnar grains with tilt growth angle and no obvious texture for LP-DED Al5083 alloy (Fig. 32b) [211]. In contrast, columnar grains growing epitaxially along the build direction with the preferred orientation along (100) were observed for LP-DED Al3104 (Fig. 32c) [210]. This highlights the important role of processing parameters on texture formation. What is more, the elements with high evaporation pressure (Fig. 31a) suffer from evaporation during LP-DED due to the high energy input. It is reported that the evaporation of Mg elements made the Al5083 alloy evolve into Al5754 [211]. This indicates that the actual composition needs to be taken into consideration when LP-DED process of Al alloy with high evaporation pressure.

There are various studies investigating the microhardness and tensile properties of LP-DED Al alloys (Table A. 9). Due to the heterogeneous microstructure associated with the varied thermal history, the microhardness shows heterogeneity along the build direction. The microhardness decreases from the bottom (~65 HV) to the top side (~53 HV) due to decreased cooling rate and larger secondary dendrite arm spacing for LP-DED AlSi10Mg [208]. The hardness is comparable to that of cast counterparts (~67 MPa) [215]. As for the Al3104 alloy, it exhibits a higher microhardness relative to that of DC-cast fabricated counterparts in the investigated conditions, such as the as-built state, homogenized states, hot-rolled state, and annealed state (Fig. 32d), indicating that LP-DED technology can potentially fabricate the high-performance Al3104 alloy [210]. The higher hardness in the as-built state is ascribed to the rapid cooling rate and dislocation structure while the retardancy of grain growth in the LP-DED samples guarantees higher hardness after heat treatment. The above result indicates the processing conditions and Al alloy systems need to be taken into consideration when the hardness is benchmarked with cast counterparts. As for the tensile property, the LP-DED Al−12Si and AlSi10Mg alloys exhibit a lower yield strength relative to those of

their L-PBF counterparts. The yield strength of LP-DED Al−12Si is ~122 MPa [216], which is similar to that of its cast counterpart (~104 MPa) [126] and lower than that of its L-PBF counterparts (~ 235–284 MPa) (Table A. 4). The lower yield strength of LP-DED sample is due to the lower cooling rate and coarser microstructure relative to those of L-PBF. In terms of the Al5754 alloy, the yield strength ranges from 113 MPa to 120 MPa, slightly higher than that of wrought counterparts (minimum of 80 MPa) [211]. Furthermore, it exhibits PLC serrations during the tensile test (Fig. 32e) [211], which is ascribed to the interaction between the solute Mg atoms and mobile dislocations during the tensile test [102].

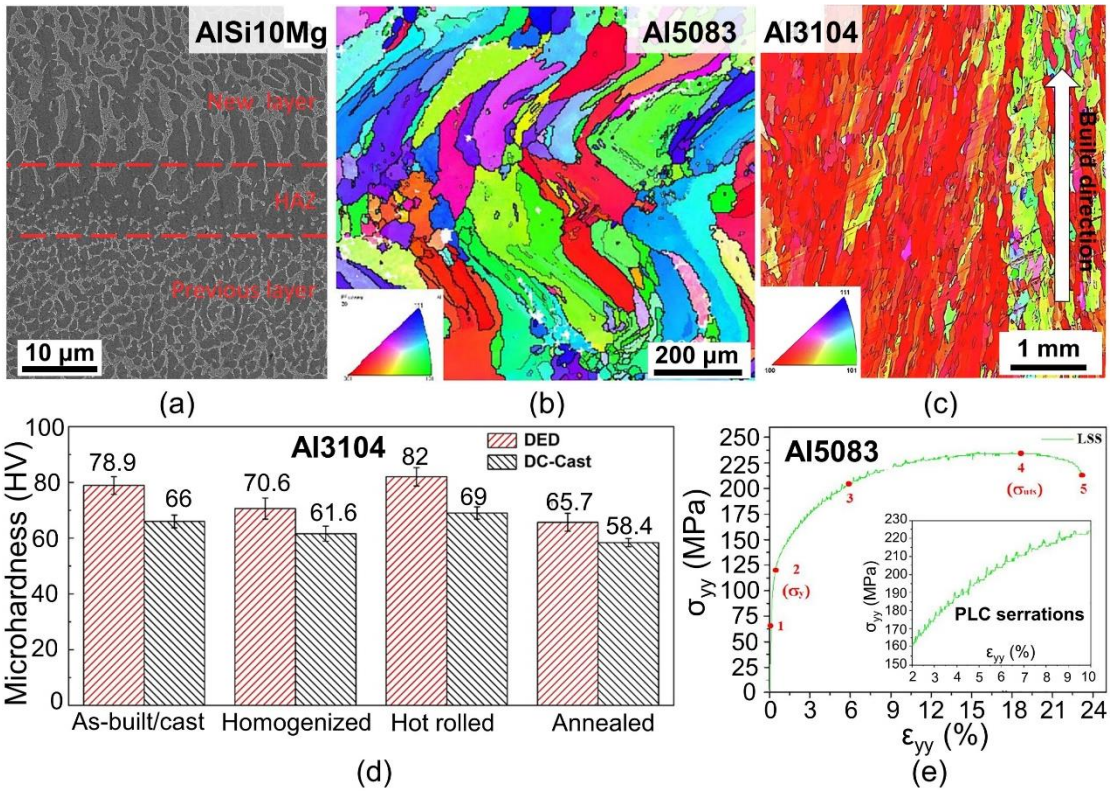

Fig. 32. Microstructure and mechanical properties of laser powder direct energy deposition aluminum alloys. (a) Representative optical microscopy images of the AlSi10Mg specimen in the longitudinal section [213]. Electron backscattered diffraction images of (b) Al5083 alloy [211] and (c) Al3104 alloy [210]. (d) Hardness evolution of laser powder direct energy deposition and direct-chill casting (DC) fabricated Al3104 under different conditions [210]. (e) Tensile property of Al5083 alloy [211].

Apart from Al–Si alloy and moderate-strength Al alloy without inoculation treatment, the well-known Al−Mg alloys inoculation treated with Sc and Zr have been studied using LP-DED. Due to the different thermal history, the LP-DED Al−Mg−Sc−Zr alloy exhibits different microstructure and mechanical properties relative to those of its L-PBF counterparts [217]. The LP-DED Al−Mg−Sc−Zr alloy contains equiaxed grains with an average grain size of 8 μm (Fig. 33a) while the L-PBF Al−Mg−Sc−Zr alloy consists of a heterogeneous microstructure containing coarse grains (grain size of 3.8 μm) and ultrafine grains (grain size of 0.8 μm) (Fig. 33b). Due to the relatively lower cooling rate associated with the LP-DED, the primary Al_3(Sc,Zr) particles form in both the interior and boundaries of the melt pools, triggering the formation of fine equiaxed grains. In contrast, the heterogeneous solidification dynamics along the melt pool boundary and the interior of the melt pools lead to the formation of a bimodal microstructure in L-PBF. The cooling rate at the melt pool boundary is slow enough to trigger the precipitation of primary Al_3(Sc,Zr) particles. It increases towards the centre of the melt pools, leading to the solute trap of Sc and Zr, and the depletion of primary Al_3(Sc,Zr) particles, which results in epitaxial grain growth and the formation of columnar grains. Due to the different microstructure, the L-PBF sample shows a higher yield strength (Fig. 33c). To alter the thermal history, Wang et al. [207] further fabricated the Al–Mg–Sc–Zr alloy using LP-DED on the air-cooled (AC) and water-cooled (WC) substrates. The samples fabricated on the AC substrate consisted of fully equiaxed grains (Fig. 33d), while those fabricated on the WC substrate consisted of a heterogeneous grain structure (Fig. 33e), including fine equiaxed grains at the fusion boundary and coarse columnar grains towards the centre of the molten pools. The formation of a bimodal grain structure on the WC substrate is due to the fact that the cooling rate increases, and the cooling rate is rapid enough to trigger the solute trap of Sc and Zr in the interior of the melt pools. Thus, columnar grains form in the centre of the melt pools. Due to the solute trap of Sc and Zr in the samples fabricated on the WC substrate, the samples provide a more significant strengthening from the secondary Al_3(Sc,Zr) particles after aging. As a result, the samples fabricated on the WC substrate exhibit a higher strength compared with their AC substrate counterparts (Fig. 33f).

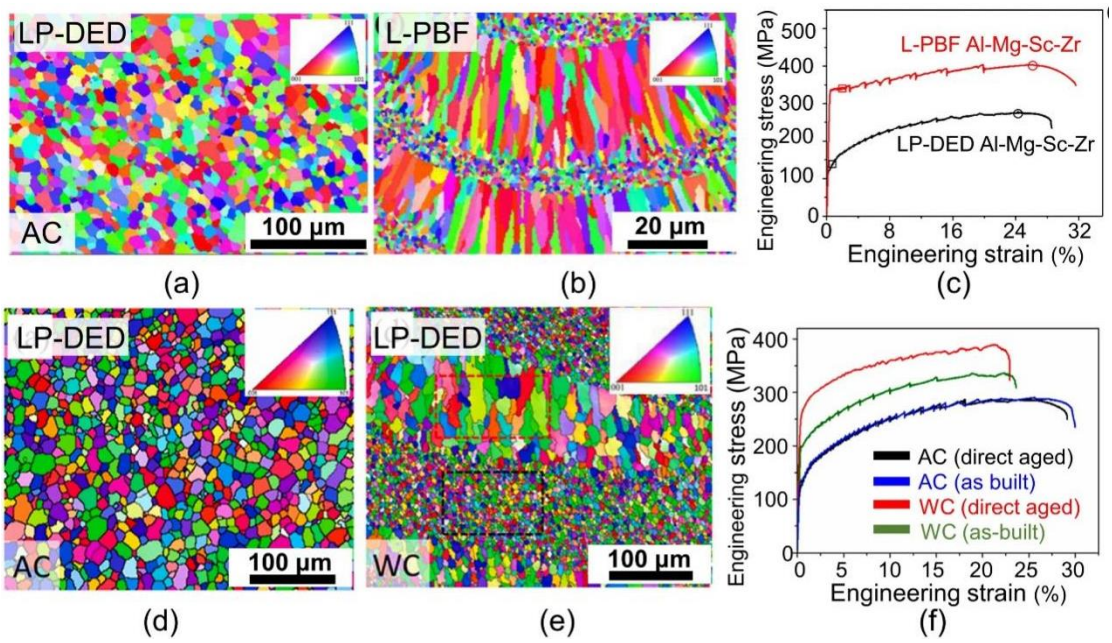

Fig. 33. Microstructure and tensile properties of laser powder direct energy deposition Al–Mg–Sc–Zr alloys. Electron backscattered diffraction of the (a) laser powder direct energy deposition and (b) laser powder bed fusion Al–Mg–Sc–Zr alloys; (c) The tensile property of laser powder direct energy deposition and laser powder bed fusion Al–Mg–Sc–Zr alloys [217]. Electron backscattered diffraction of laser powder direct energy deposition Al–Mg–Sc–Zr with (d) air cooling (AC) and (e) water cooling (WC). (f) The tensile property of laser powder direct energy deposition Al–Mg–Sc–Zr alloys with air cooling (AC) and water cooling (WC) [207].

Apart from the Al–Si and Al–Mg alloys, there have also been a few attempts to fabricate high-strength Al alloys, such as Al–Cu [209], Al–Mg–Si [218], and Al–Zn alloys [219,220]. Crack-free Al2024 alloy with a relative density of 99.7% can be fabricated exhibiting gradient microstructure along the build direction due to the varied thermal history and thermal cycling [209]. The LP-DED Al2024 alloy shows a yield strength of ~170 MPa, which is higher than that of wrought counterparts (< 95 MPa) [209]. However, the strength is not competitive with that of L-PBF Ti-modified Al2024 [97], which exhibits a significant grain refinement. As for LP-DED Al6061 [218] and Al7075 [219] alloys, they exhibit cracks due to high hot-crack susceptibility and rapid cooling rate. Besides, the evaporation of Mg and Zn caused porosity in the LP-DEDAl7075

alloy [220]. Up to now, baseplate preheating to decrease thermal gradient has been demonstrated to be an efficient way to heal cracks [218,219].

5.2 Electron beam powder bed fusion of aluminum alloys

Since preheating is necessary for EB-PBF to inhibit the smoke and reduce thermal stress, EB-PBF has a high potential to fabricate high-strength Al alloys that are susceptible to cracking. Moreover, the building chamber under the vacuum state can also prevent oxidation, which makes it appealing to process Al alloys. However, investigations into fabricating Al alloys using this approach are far rare compared to those fabricated via L-PBF [221-227]. Some of the tensile properties of EB-PBF Al alloys are listed in Table A. 10.

For the typical AlSi10Mg, it exhibits a totally different microstructure relative to that of L-PBF counterparts, which exhibit cellular structures. The EB-PBF AlSi10Mg alloys contain AlFeSi phase and Si particles (Fig. 34a) [222]. Furthermore, the as-built alloy mainly consisted of equiaxed grains with a grain size of about 40 μm (Fig. 34b) and fine sub-grains with sizes ranging from 0.5-2 μm (Fig. 34c). Specific to the mechanical property, it is found that the hardness and yield strength is lower for the EB-PBF sample relative to that of L-PBF counterparts (Fig. 34d,e). The hardness of EB-PBF AlSi10Mg is lower than that fabricated via L-PBF (Fig. 34d). The higher hardness and yield strength for the L-PBF AlSi10Mg is ascribed to the supersaturated Si in the matrix and residual stress in the samples due to the fast-cooling rate associated with L-PBF. The mechanical property of EB-PBF AlSi10Mg can be further tailored via post heat treatment. After ST, the hardness of L-PBF AlSi10Mg decreased due to the release of residual stress while it increased for the EB-PBF-fabricated AlSi10Mg due to the dissolution of Si into the matrix. The hardness and yield strength of EB-PBF alloy can be further enhanced after aging due to the precipitation of a few spherical and rod-like particles (Fig. 34d). The yield strength of EB-PBF AlSi10Mg increased from about 62.2 MPa in the as-printed condition to 249.3 MPa upon aging. In particular, the ultimate

tensile strength of 136.6 MPa is lower than that of its cast counterparts [58].

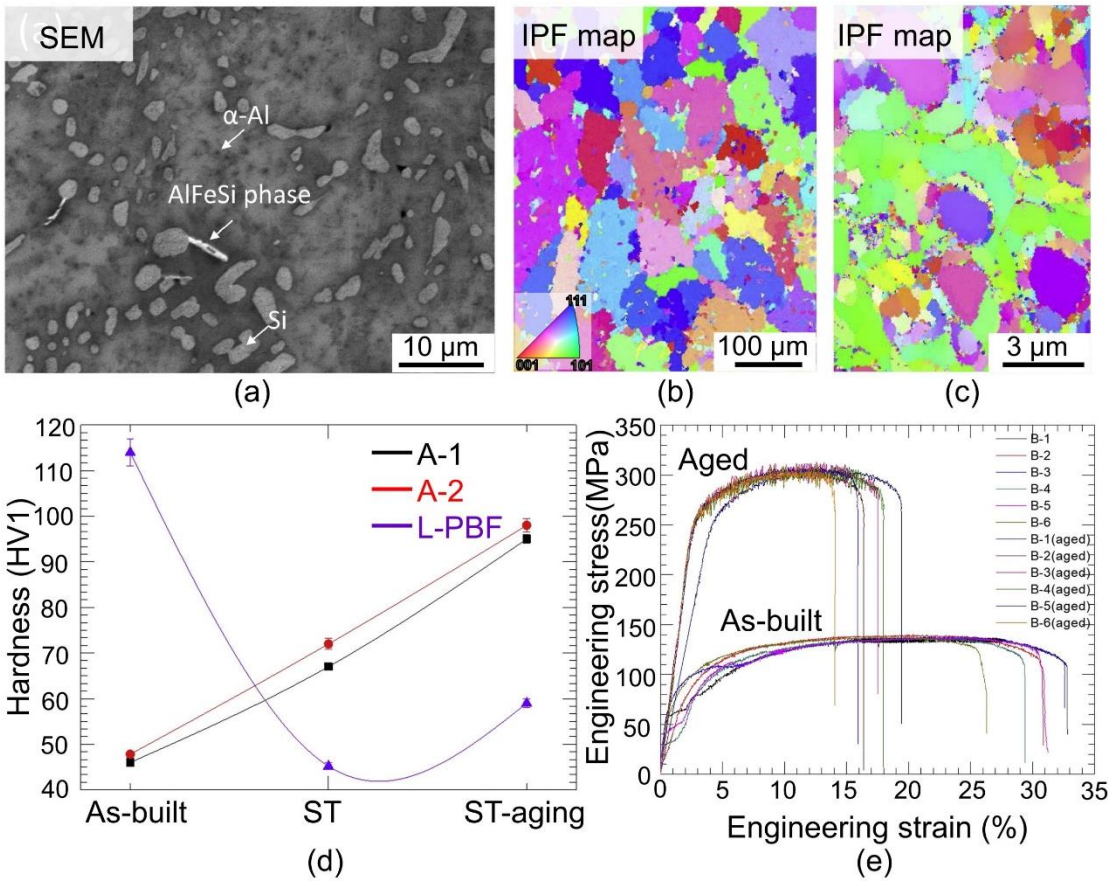

Fig. 34. Microstructure and mechanical property of as-built electron beam powder bed fusion AlSi10Mg alloy [222]**.** (a) Scanning electron microscopy image, (b) and (c) Electron backscattered diffraction inverse pole figure (IPF) images at different magnifications, (d) hardness, (e) engineering stress–strain curves.

Besides the Al–Si alloys, there are also pioneering studies on fabricating moderate- and high-strength Al alloys, such as the Al–Cu, Al–Mg, and Al–Zn of alloys via EB-PBF. Through printing parameter optimization, highly dense Al2024 samples with a relative density of 99.7% were fabricated [223]. The EB-PBF Al2024 exhibited a progressively decreased average area fraction of Al_2Cu from top to bottom along the build direction due to the thermal cycling effect [223], which results in a lower yield strength at the bottom side. Other than AlSi10Mg and Al–Cu alloys, there have also been some printing feasibility studies of medium-strength Al–Mg [227] and high-strength Al–Zn alloys [224]. However, systematic investigations have not been conducted, limited by

the quality of printed samples, due to the formation of pores and element evaporation. These are critical issues that need to be solved in the future.

5.3 Wire arc additive manufacturing of aluminum alloys

WAAM boasts the advantage of a high deposition rate, which is attractive for industrial applications and has been implemented to process alloys, including steels [228], Ni-based superalloys [229], and Ti alloys [230]. To date, considerable work has been conducted on the WAAM of Al alloys [231]. One essential challenge during WAAM of Al alloys is control of the shape and properties, since the inherent high thermal input can lead to high residual stress and distortion, and even result in cracks and delamination. It has been demonstrated that the heat input [232] and arc mode [233] play a critical role in influencing the final forming quality. A lower heat input can facilitate the reduction or even the elimination of porosity [232], while the pulsed arc mode engenders a lower porosity level relative to that of non-pulsed mode [233].

The WAAM Al alloys exhibited a heterogeneous microstructure consisting of equiaxed grains in the inter-layer zone and columnar grains in the inner-layer zone, such as the Al–Zn–Mg–Cu [234], Al–Cu [235,236], Al–Mg [237], and Al6061 [238]. Fig. 35a,b show the microstructure of the WAAM 2219Al sample deposited on the water-cooled substrate. The alternative distribution of equiaxed grains and columnar grains is visible, which is attributed to the heterogeneous distribution of Al_3Zr particles due to the existence of Zr in the 2219Al wires [236]. The microstructure of as-printed samples can be tailored via modifying the chemical composition of the wires [239,240] or by changing the printing conditions [241]. Guo et al. [239] have fabricated the 7B55-Sc alloy decorated with equiaxed grains instead of band structure[242,243]. The formation of equiaxed grains is ascribed to the heterogeneous nucleation of Al triggered by Al_3(Sc,Zr) particles (Fig. 35c_1,c_2). Fu et al. [241] have fabricated an Al–Zn–Mg–Cu alloy mainly consisting of equiaxed grains via feeding hot wire. The columnar to equiaxed grain transition was ascribed to the reduced arc heat input.

Table A. 11 lists the tensile properties of WAAM Al alloys. Similar to the microstructure evolution, the mechanical properties of WAAM Al alloys are sensitive to the printing conditions. Taking the WAAM Al2219 as an example, Wang et al. [235] have reported the yield strength and ultimate tensile strength of 95.2 MPa and 224 MPa, respectively, when the air-cooled substrate is used (Fig. 35d). However, the yield strength and ultimate tensile strength reached 110 MPa and 248 MPa, due to finer grains and smaller primary dendrite arm space when the water-cooled substrate is used [236]. For the WAAM Al–Zn alloys, an ultimate tensile strength of 618 MPa can be achieved with contributions from grain refinement and precipitation hardening (Fig. 35e) [240].

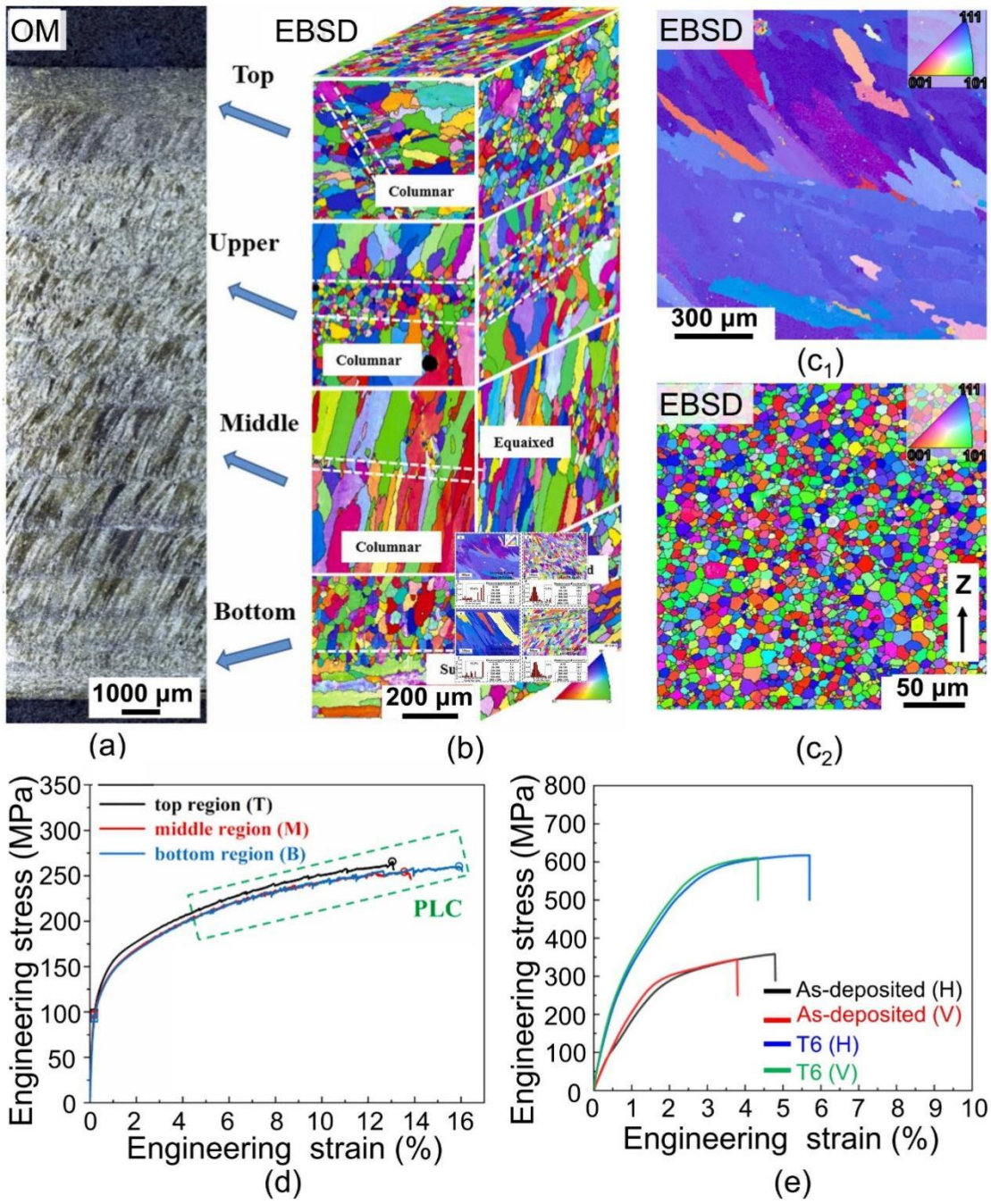

Fig. 35. Microstructure and tensile properties of wire-arc additive manufacturing aluminum alloys. (a) Optical microscopy and (b) electron backscattered diffraction of wire-arc additive manufacturing Al2219 on the water-cooled substrate [236]. Electron backscattered diffraction of (c_1) AlZnMgCu [242] and (c_2) AlZnMgCuSc [239]. (d) Mechanical property of wire-arc additive manufacturing AA2219 alloy [235]. (e) wire-arc additive manufacturing AlZnMgCuSc in the as-deposited and T6 states [240].

Apart from chemical composition modification, inter-layer deformation has also been

adopted to modify the grain structure, such as through inter-layer hammering. The columnar to equiaxed (CTE) transition is due to the plastic deformation and subsequent intrinsic in situ heat treatment. What is more, inter-layer hammering can eliminate pores. Both grain refinement and pore elimination can contribute to enhancing the mechanical performance of the alloy. Fang et al. [244] (Fig. 36a) reported that the total volume of pores decreased from 0.46 mm^3 in the as-deposited states to 0.12 mm^3 with inter-layer hammering. The WAAM Al–Mg alloy consisted of two regions (Fig. 36b) [245], namely the coarse grain region, which is the work hardening region, and the fine grain region, which is the recrystallized region. With inter-layer hammering, the yield strength is enhanced from 148 MPa to 289 MPa with a 50.8% deformation (Fig. 36c) [244].

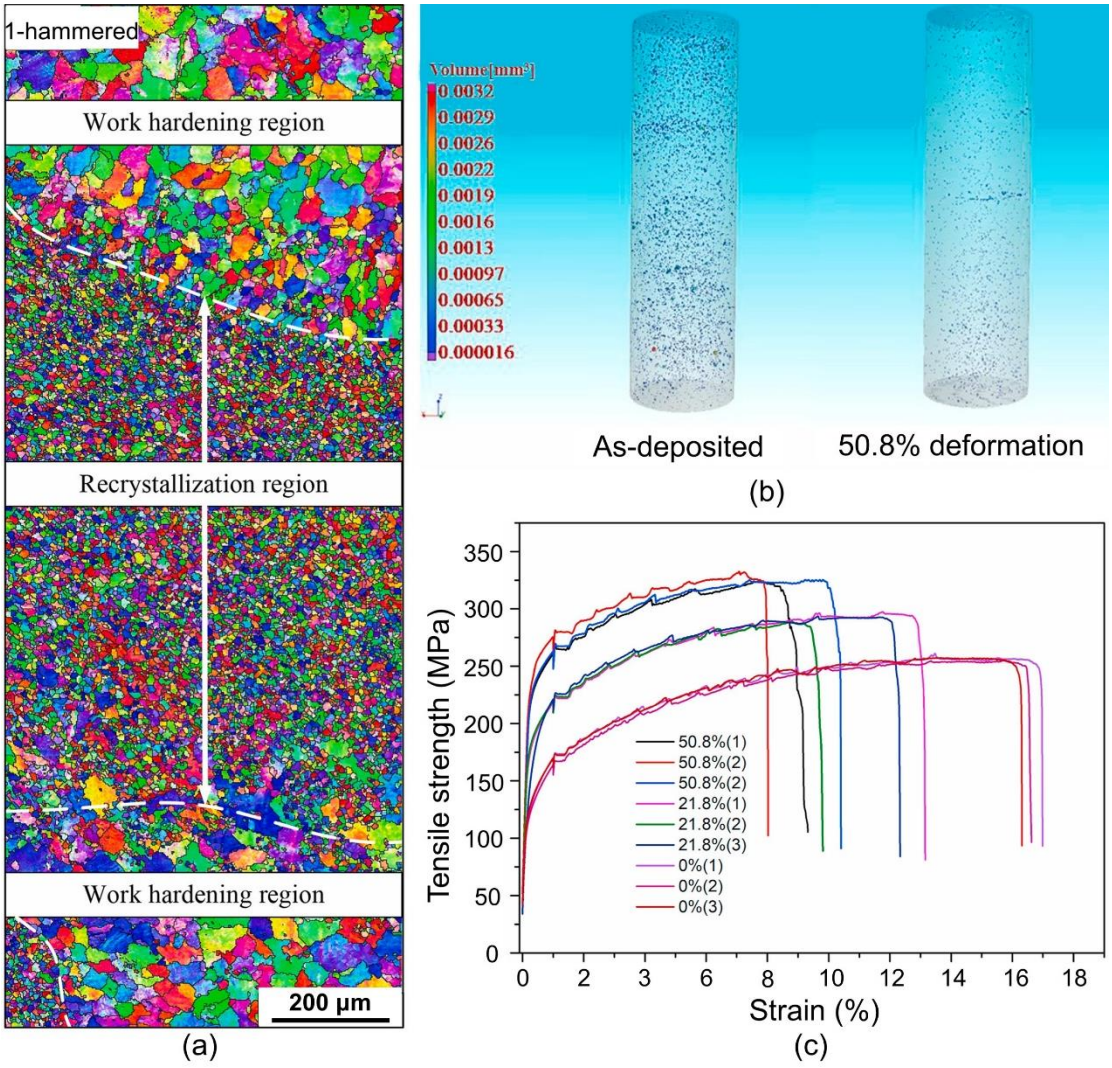

Fig. 36. Evolution of microstructure, densification, and tensile property of wire-

arc additive manufacturing aluminum alloy with inter-layer hammering. (a) Electron backscattered diffraction of wire-arc additive manufacturing Al5B06 with inter-layer hammering [245]. (b) Pore distribution of wire-arc additive manufacturing Al2219 samples without and with hammering [244]. (c) Tensile properties of wire-arc additive manufacturing Al2219 alloy without hammering and with inter-layer hammering to different deformations [244].

5.4 Binder jetting of aluminum and aluminum alloys

Unlike the PBF AM processes, BJ is compatible to process various alloys [22]. However, several issues have prevented the broad application of Al alloys for BJ. Firstly, safety should be taken into consideration when processing the reactive Al powders with BJ [23]. Secondly, the natural oxide layers on the surface of the powders slow down mass transport and make the Al powders difficult to sinter [246]. To date, only one journal paper has been published on the fabrication of unalloyed Al using BJ [15]. The effect of various factors, including binder saturation, roller traverse speed, layer thickness, and sintering atmosphere, on the printing quality of BJ Al parts is studied [15]. The dependence of different levels of binder saturation (from 15% to 100%) on the printing quality of BJ Al indicates that a lower fraction of binder makes the printed sample brittle, while a high fraction of binder leads to the excessive spread of the binder (Fig. 37a) However, the density of sintered parts is still not high enough, and the overall porosity is 50-55% (Fig. 37b). The low densification may be attributed to the formation of oxide layers which slows down the mass transport process during sintering.

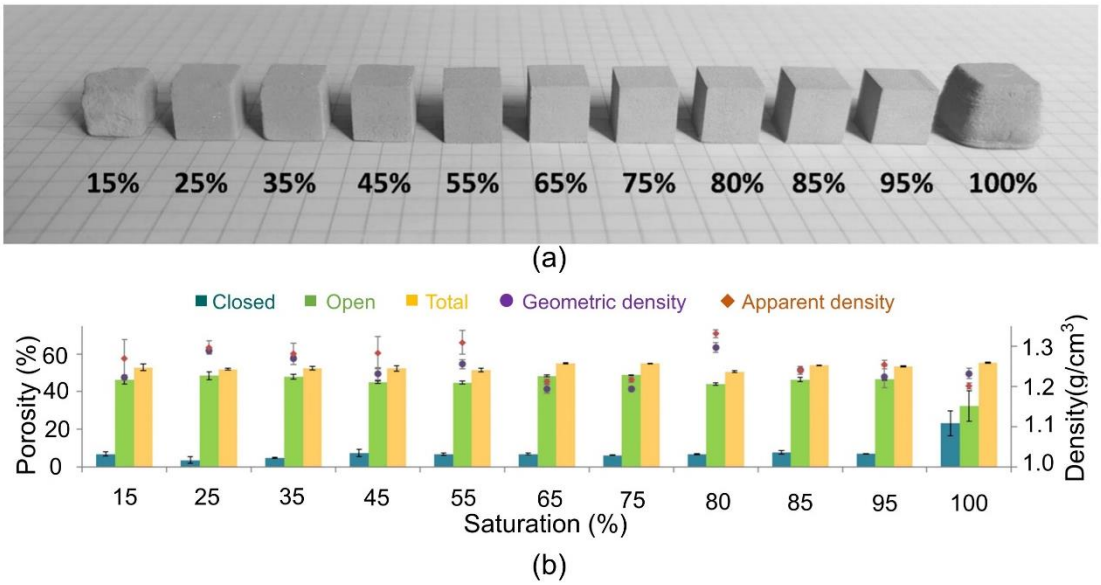

Fig. 37. Morphology and densification of binder jetting printed aluminum parts [15]**.** (a) The binder jetting printed parts with different amounts of binder saturation from 15% to 100%. (b) The fraction of closed pores, open pores, geometric density, and apparent density of binder jetting printed Al parts after sintering in a vacuum.

ExOne and the Ford Motor Co. have developed a new patent-pending process for fabricating Al6061 parts with a final density of 99% and mechanical properties comparable to traditional manufacturing [247]. This can unlock the new fabrication methods of Al alloys in a faster and more scalable way [26].

5.5 Additive friction stir deposition of aluminum alloys

As aforementioned, hot cracks tend to form during melt-based AM of high-strength Al alloys, which belong to the unweldable alloys. To overcome the hot cracks formed in the melt-based AM of high-strength Al alloys, AFSD [43,248-250] has been developed to process the materials and it has broad applications to fabricate Al alloys. Compared with melt-based AM, AFSD technology does not require a harsh fabrication environment, such as shielding gas. Some of the tensile properties of AFSD Al alloys are listed in Table A. 12.

Since the AFSD is mainly targeted for the fabrication of high-strength with pool weldability, it has been used adopted to process, AA2214 [249,250], AA5083 [251], and Al–Zn [252] alloys. Due to the dynamic recrystallization during AFSD, the microstructure in the stir zone is dominated by the equiaxed grains, as reflected by the significant reduction of grain size of about 200 μm for the feedstock to 15 ± 4 μm in the as-deposited Al6061(Fig. 38a-c) [248]. However, it seems that the rotational speed and advancing speed do not significantly influence the grain size of the deposited material. The nearly constant grain size was also observed along the whole build from the top to the bottom for AA2219 alloy [249] (Fig. 39a), indicating the different thermal histories do not significantly influence the grain size though the bottom side experience more thermal cycles. The hardness of AFSD AA2219 shows a trend of minor decrease from the top to the bottom side, and it is lower than that of feedstock AA2219 alloy (AA2219-T851) (Fig. 39a) [249]. The lower hardness is due to the fact that the main strengthening precipitates (θ' precipitates) observed in the feedstock materials are not observed in the AFSD AA2219 (Fig. 39b), which is decorated by the coarser θ precipitates (Fig. 39c) [249]. The high temperature during the AFSD process dissolves the θ' precipitates, and the slow cooling rate allows for the formation of θ precipitates. Similar phenomenon was observed for the AFSD AA6061, where the main strengthening β'' precipitates in the feedstock alloy were replaced by the β precipitates, causing a decrease in the hardness [248]. The above findings indicate that though the grains are refined after the AFSD process, the dissolution of major strengthening phases (θ' precipitates in the AA2219 and β'' precipitates in the AA6061) during AFSD leads to a lower hardness for the AFSD Al alloys.

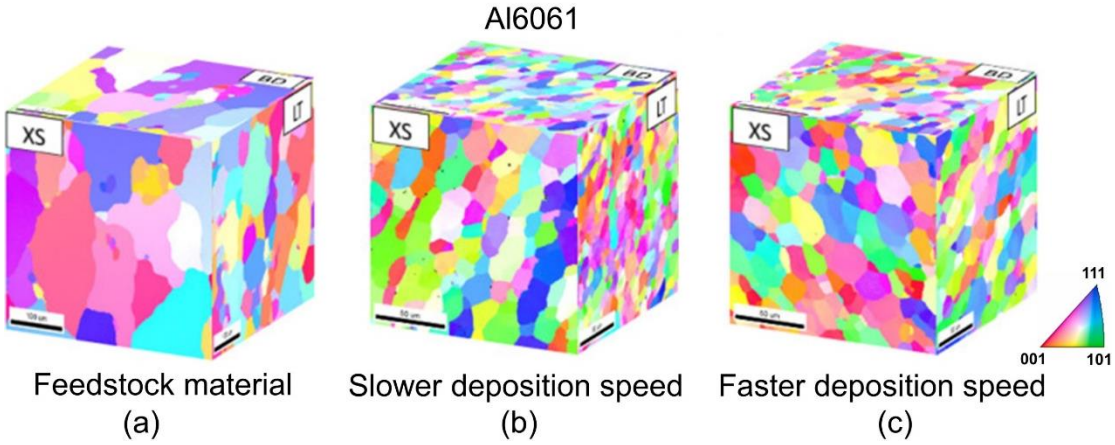

Fig. 38. 3D-electron backscattered diffraction images of the feedstock materials and additive friction stir deposition Al6061 alloy [248]. (a) feedstock materials. (b) Additive friction stir deposition Al6061 with slower deposition speed and (c) additive friction stir deposition Al6061 with faster deposition speed.

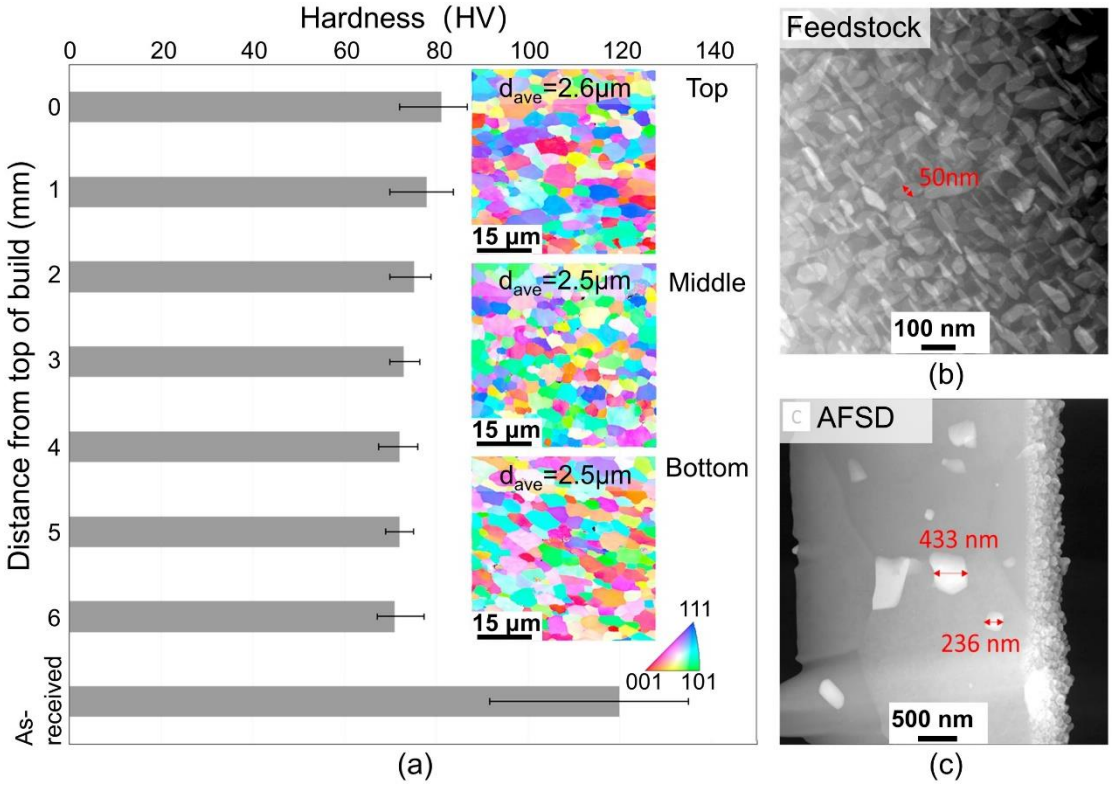

Fig. 39. Microstructure and hardness of additive friction stir deposition AA2219 alloy [249]. (a) Electron backscattered diffraction and hardness of additive friction stir deposition AA2119 and feedstock material. Transmission electron microscopy images showing the (b) θ' precipitates in the feedstock material and (c) θ precipitates in the additive friction stir deposition AA2219, respectively.

Due to the dissolution of the major strengthening θ' precipitates in the AFSD AA2219 alloy, it exhibits a lower yield strength (125 MPa-159 MPa) relative to that of feedstock material(350 MPa). Meanwhile, the yield strength decreased from the top to the bottom side (Fig. 40a) ascribing to the texture evolution [249]. For the AA7075, the AFSD sample exhibits a lower yield strength than that of feedstock material (AA7075-T651) due to coarsening of major strengthening phases of η' and η [253]. However, the heat treatment is effective in tailoring the microstructure and mechanical properties of Al alloy. Through T6 heat treatment, wrought-like mechanical properties have been achieved for AFSD Al7000 (Fig. 40b) [252], indicating the potential applications of AFSD to fabricate high-performance Al alloys.

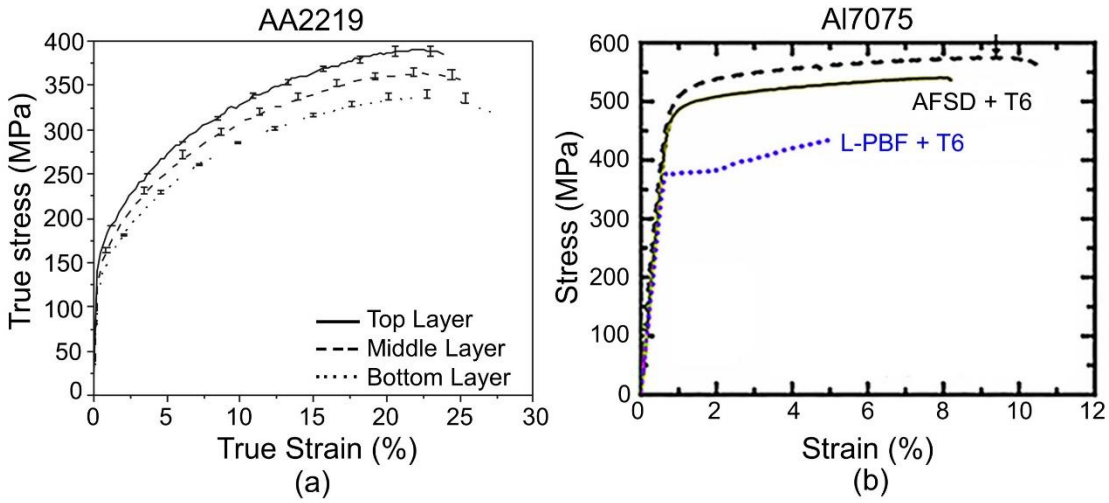

Fig. 40. Tensile property of additive friction stir deposition aluminum alloys. (a) Dependence of tensile properties on the layers [249]. (b) Tensile properties of wrought Al7075 alloy under T6 heat treatment condition, laser powder bed fusion Al7075 under T6 heat treatment condition, and additive friction stir deposition Al7075 under T6 heat treatment condition [252].

5.6 Advantages and limitations of other technologies

Based on *Section 2.2*, LP-DED technology shows the merits of a high deposition rate, the construction of large components, eligibility to do repairing, and fabrication of functionally graded materials. However, it also shows the drawbacks of low dimensional accuracy and higher surface roughness. Specific to Al alloys, it also shows

the following limitations. (i) the results hitherto indicate that the strength of Al alloys fabricated via LP-DED is lower than that of L-PBF, as supported by the AlSi12, AlSi10Mg, AlMnSc, and AlMgScZr alloy (Fig. 41), making it less attractive when high mechanical performance is needed; (ii) the poor flowability of Al powders arising from the low density can affect the stability of the powder flow rate, degrading the quality of printed samples [254]; and (iii) the high moisture content of Al powders can also influence the quality of deposited samples [12].

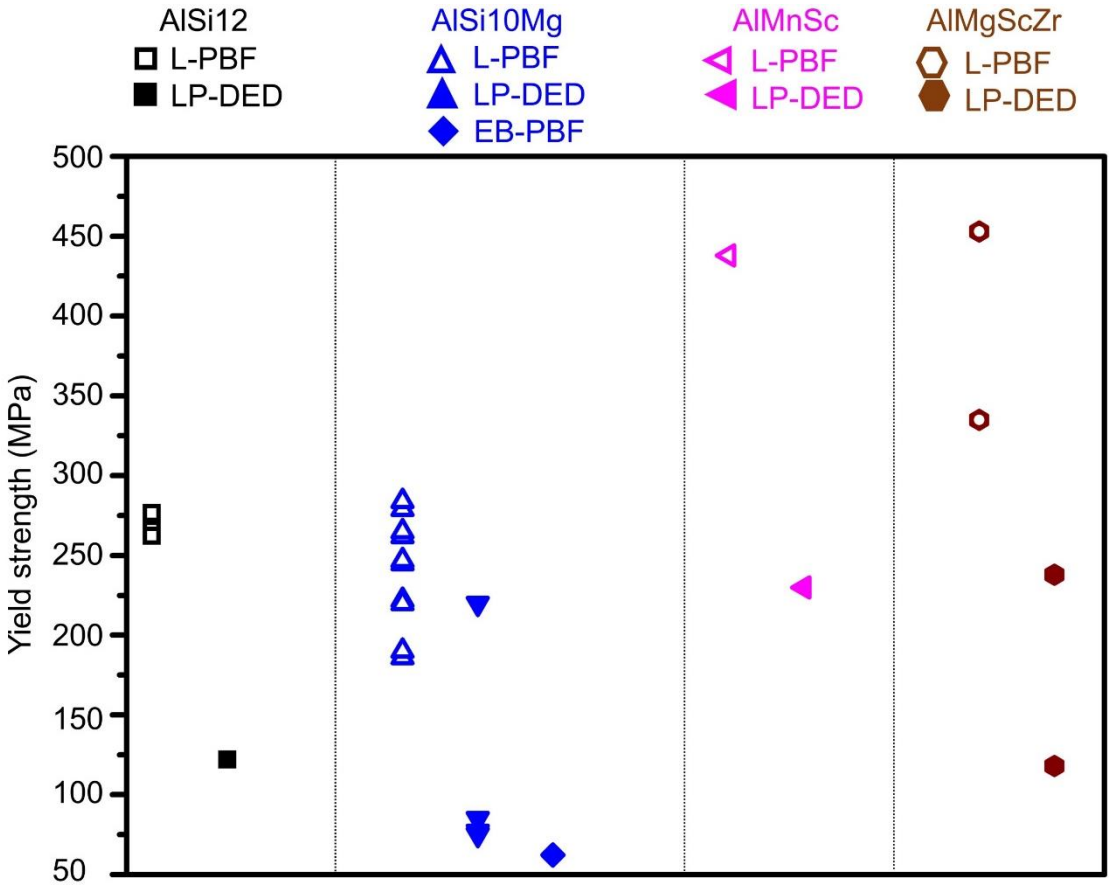

Fig. 41 Plot of yield strength of aluminum alloys fabricated via laser powder bed fusion, laser powder direct energy deposition, and electron beam powder bed fusion. The data used to plot the figure is based on the data from Table A. 4, 5, 9, and 10.

EB-PBF has been broadly adopted to fabricate Ti alloys and Ni-based superalloys. When the Al alloys are referred to, the vacuum environment during EB-PBF could minimize the oxidation issue. However, the adoption of Al alloys for EB-PBF is still

scarce relative to that of Ti6Al4V. The possible reasons may be associated with the elemental evaporation and formation of defects, such as cracks and porosity. Finally, the uncompetitive mechanical properties could be another reason accounting for the lack of research interest (Fig. 41).

WAAM shows the advantages of a higher deposition rate and higher material usage, reducing the fabrication cost. It has been adopted to process various Al alloys, and some of the alloys exhibit high strength. However, investigations of properties beyond tensile property are needed to pave the way for industrial application [240].

As a solid-state AM process without involving the solidification process, BJ can virtually print almost any powders with a high fabrication rate. However, the safety issues and less efficient sintering associated with the surface oxide layers during the BJ of Al alloy powders need to be tackled before it is broadly implemented for AM.

AFSD technology could render a higher deposition rate compared with that of L-PBF, EB-PBF, and LP-DED. Furthermore, there is ample room to control the macrostructure (such as shape), mesostructure, and microstructure of AFSD samples. The solid-state AM can also naturally overcome the crack issues of Al alloys associated with fusion-based AM technologies. Thus, it is foreseen that the AFSD can play a more important role in fabricating Al alloys in the future. However, it also shows some disadvantages as discussed in *Section 2.2*, such as the need for special clamps and customized fixtures are needed when complex-shaped components are printed, the limited minimum feature size, and the need for post-processing.

6. Additive manufacturing of aluminum matrix composites

AMCs exhibit a series of advantages, such as high specific strength, stiffness, high resistance to corrosion, and excellent high-temperature mechanical properties [255]. The conventional fabrication route for AMC includes the solid-state process

(consolidation, diffusion bonding, and vapor deposition) and liquid-state process (stir casting, compo casting, infiltration, spray casting, and in situ processing). However, these methods have limitations in terms of fabricating complex-shaped components. Leveraging the fabrication of AMCs could broaden the industrial applications of AM.

Up to now, L-PBF, LP-DED, EB-PBF, WAAM, and AFSD have been used to fabricate the AMCs, with L-PBF being the most widely used. To distinguish the functionalized powders used to improve printability, such as the additives Ti, Sc, Nb, and Zr, here the reinforcement particles are limited to ceramic particles. *Section 6.1* describes the commonly adopted ceramic particles. The microstructure and mechanical properties of AM AMCs are described in *Section 6.2*. Finally, the advantages and limitations of each technology in fabricating in AMC are given in *Section 6.3*.

6.1 Aluminum matrix and reinforcement particles

The common reinforcement particles used for fabricating AMC include the TiB_2, TiC, TiB_2 + TiC, Al_4SiC_4 + SiC, carbon, LaB_6, Al–Ti–C–B master alloy, SiC, ZrO_2 + Si, carbon nanotubes (CNT), TiN and TiO_2. Fig. 42 shows a compilation of AMCs fabricated via L-PBF, LP-DED, EB-PBF, WAAM, and AFSD. It can be seen that the Al–Si and Al–Cu alloys are the most investigated Al matrix for AMCs.

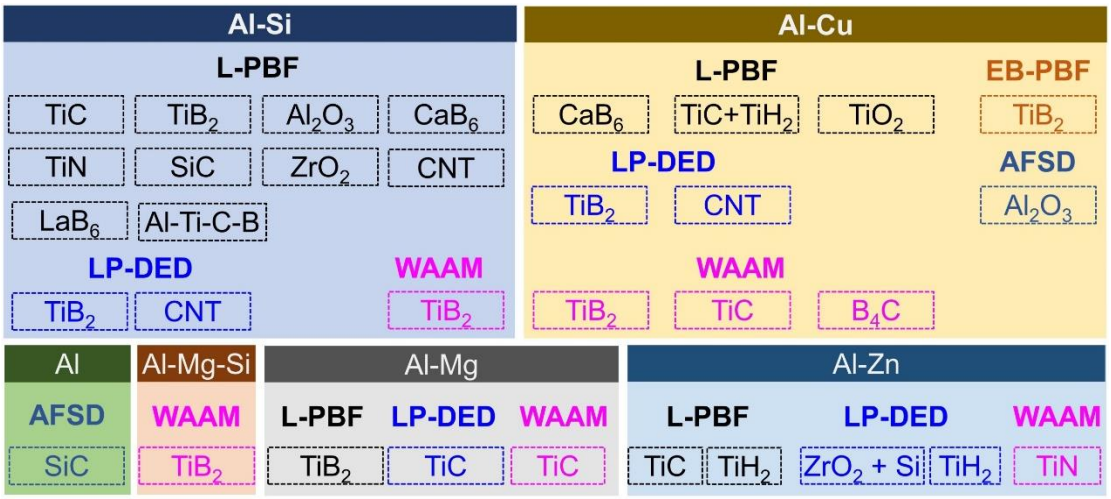

Fig. 42. Compilation of laser powder bed fusion and laser powder direct energy deposition aluminum matrix composites. The data are cited from [256-274].

6.2 Microstructure and mechanical properties

Four sections are divided to discuss the microstructure and mechanical properties of AMCs fabricated via L-PBF, LP-DED/EB-PBF, WAAM, and AFSD, respectively. Some of the tensile properties of AMCs fabricated using various AM methods are listed in Table A. 13.

6.2.1 Laser powder bed fusion

Up to now, the introduction of reinforcement particles for L-PBF AMCs has been achieved via two routes. The first and the most frequently used is through powder blending, such as ball milling [275] and mechanical mixing [269], while the other is through introducing the reinforcement particles into the Al alloy to get the master alloy, followed by fabricating the AMC powders [276]. For the powder blending method, it is convenient to design alloys with novel compositions without isolated atomization for each composition. However, the quality of as-fabricated samples relies on several factors: (1) the uniform distribution of reinforcement particles into the Al matrix powders, which can be influenced by the blending time and blending media; and (2) the size of the reinforcement particles. During the L-PBF process, the reinforcement particles undergo dissolution into the Al matrix. Thus, particles with a high surface-to-volume ratio can be dissolved into the Al melt more readily. However, the nano-sized reinforcement particles with a high surface-to-volume ratio may agglomerate, affecting the printing quality [277]. Thus, leveraging the size of the reinforcement particles is critical to achieving high quality.

As the present dominant technology in fabricating AMCs, L-PBF provides advantages in the uniform dispersion of reinforcement particles into the Al matrix due to the turbulent melt pool with high fluid velocities (> 1 m/s) induced by the Marangoni effects and recoil pressure [278]. Depending on the specified reinforcement particles that have been added and the Al matrix, the following effects are achieved: (1) inducing grain refinement. These kinds of ceramic particles include TiB_2 [257], TiN [273], TiC

[261], and LaB_6 [267], particles. The results indicate that the addition of TiB_2 can refine the grains for the Al−12Si [257] (Fig. 43a_1,a_2), AlSi10Mg [276], and Al–Cu alloys [279], ascribing to the lower interatomic misfit between the α-Al matrix and TiB_2, leading to a reduction of critical nucleation undercooling ΔT_c. However, the columnar to equiaxed grain transition with the addition of TiB_2 ceramic particles is not universal. Cheng et al. [264] and Wang et al. [280] found that the addition of TiB_2 did not trigger grain refinement for L-PBF AlSi10Mg and Al2024 alloys, respectively. Apart from the addition of a single kind of ceramic, the coupling addition of TiB_2 and TiC particles also leads to grain refinement (Fig. 43b_1,b_2) [264]. As aforementioned, grain refinement can heal crack formation in alloys tending to form cracks during L-PBF, which has been verified for the TiC-modified Al7075 alloy [262], TiB_2-modified Al–Cu alloys [279], and TiN-modified Al–Zn alloys [273]. (2) Introducing the chemical reaction. It has been reported that the Al_2O_3 particles are formed via the addition of ZnO for the L-PBF AlSi10Mg alloy [281]. The in-situ formed Al_2O_3 particles did not refine the grains (Fig. 43c_1, c_2).

With the grain refinement, higher yield strength is achieved due to the grain boundary strengthening, which has been verified for the TiB_2-modified AlSi10Mg alloy [279,280, 282] (Fig. 43d_1) and the TiC/TiH_2-modified Al2024 alloy (Fig. 43d_2) [283]. Apart from the grain boundary strengthening, the yield strength of L-PBF SiC-modified AlSi10Mg alloy is enhanced to ~362–407 MPa depending on the adopted processing parameters due to the enhanced dislocation motion resistance caused by the SiC particles [269].

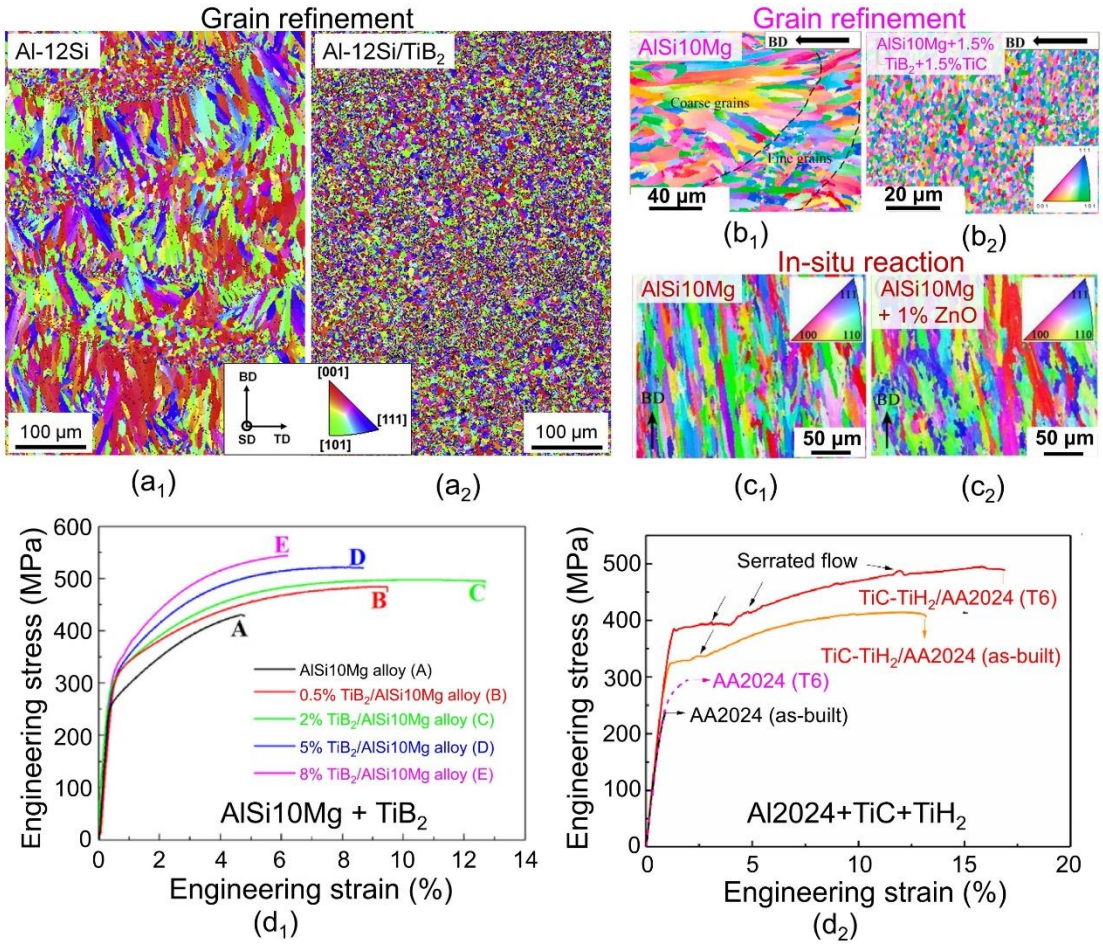

Fig. 43. Microstructure and mechanical properties of laser powder bed fusion aluminum matrix composites. (a_1,a_2) Electron backscattered diffraction of laser powder bed fusion Al−12Si alloy and Al−12Si + 2 wt.% TiB_2, respectively [257]. (b_1,b_2) Electron backscattered diffraction of laser powder bed fusion AlSi10Mg and AlSi10Mg + 1.5wt.% TiB_2 + 1.5wt. % TiC alloys [264]. (c_1,c_2) Electron backscattered diffraction of laser powder bed fusion AlSi10Mg and AlSi10Mg + 1% ZnO alloys [281]. (d_1) Tensile property of laser powder bed fusion AlSi10Mg alloy with different amounts of TiB_2 [282]. (d_2) Tensile property of laser powder bed fusion Al2024 and Al2024 with TiC–TiH_2 under as-built and T6 heat treated conditions [283].

With the growing research interest from industry, some of the developed AMCs have been commercialized and gone into the market, including the A1000-RAM10 [284], A2024-RAM2 [285], A2024-RAM10 [286], A6061-RAM2 [287], Al7050-RAM2 [288], and Al7075-RAM2 [289] alloys developed by Elementum 3D. Here, the

RAM2/RAM10 indicates that 2 wt.% or 10 wt.% ceramic particles are incorporated. Some of the as-developed AMCs exhibit a higher elevated temperature tensile property (Table A. 6 and Fig. 32).

6.2.2 Laser powder direct energy deposition and electron beam powder bed fusion

LP-DED and EB-PBF technologies are also applied to fabricate the AMCs [270,290]. The effect of reinforced ceramic particles depends on the detailed adopted ceramic particles, matrix, and fraction of ceramic particles. Fig. 44a,b show the EBSD images of the LP-DED fabricated Al2024 alloy and TiB_2-modified Al2024 alloy, respectively, signifying the grain refinement with TiB_2, which serves as a heterogeneous nucleation agent [258]. With the grain refinement, the LP-DED TiB_2-Al2024 exhibits a higher yield strength than that of its Al2024 counterparts (Fig. 44c) [291]. For the EB-PBF TiB_2-reinforced AlCuMgFeNi alloy [290], the sample presents an equiaxed grain structure with an average grain size of 8.56 μm containing TiB_2 and Cu–Fe–Ni-rich particles (Fig. 44d). The grain refinement is due to the activation of TiB_2 serving as heterogeneous nuclei. After T6 heat treatment, the Cu–Fe–Ni-rich particles and TiB_2 particles were observed with a marginal grain growth to 9.84 μm arising from excellent thermal resistance of TiB2 and intermetallic particles (Fig. 44e). After T6 heat treatment, the yield strength is enhanced from ~133 MPa to ~201 MPa (Fig. 44f).

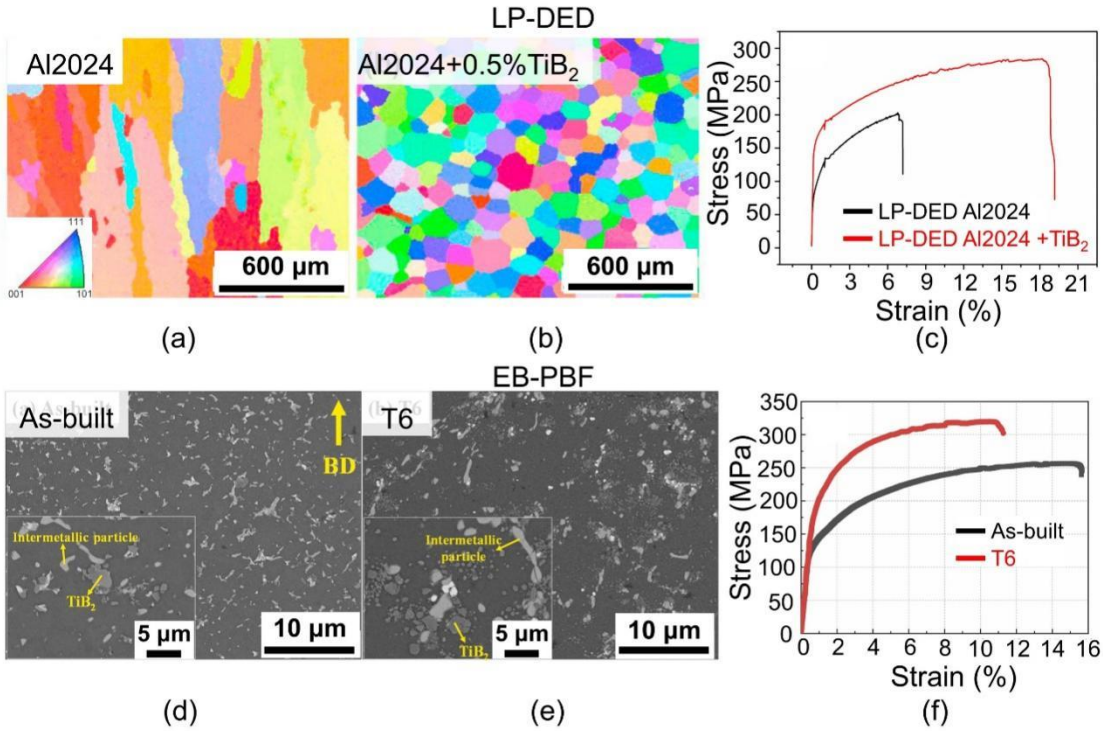

Fig. 44. Microstructure and mechanical properties of laser powder direct energy deposition and electron beam powder bed fusion aluminum matrix composites. Electron backscattered diffraction images of laser powder direct energy deposition (a) Al2024 [258]; (b) Al2024 + 0.5 wt.% TiB_2 [258]. (c) Tensile properties of laser powder bed fusion and laser powder direct energy deposition Al2024 and Al2024 + 3 wt.% TiB_2 [291]. Scanning electron microscopy of electron beam powder bed fusion TiB_2-reinforced AlCuMgFeNi alloy in the (d) as-built and (e) T6 conditions [290]. (f) Stress-strain curves of the as-built and T6 heat-treated TiB_2-reinforced AlCuMgFeNi alloy [290].

6.2.3 Wire-arc additive manufacturing

Until now, WAAM technology has been implemented to tailor the microstructure or mechanical properties of alloys by adding ceramic particles [243,292]. The microstructure and mechanical properties of ceramic particle-reinforced Al matrix are sensitive to the composition, size, and fraction of the ceramic particles. Fig. 45a,b show the microstructure of the WAAM Al–Zn–Mg–Cu and TiN-modified Al–Zn–Mg–Cu alloys [243]. The grains were refined from 459.3μm to 104.6μm, which is ascribed to the formation of Al_3Ti particles serving as the nucleation agent. With grain refinement,

the tensile strength in both horizontal and vertical directions increased. In the horizontal direction, the tensile strength increased from 207 MPa to 284 MPa. TiC has also been shown to refine the WAAM Al alloys, including Al2219. With the addition of 1.5 wt% TiC, the grain size of WAAM Al2219 decreased from 101 μm to ~20 μm (Fig. 45c,d) [292]. However, the appropriate fraction of ceramic particles and printing parameters are vital for achieving high performance for WAAM AMCs. For the TiC-modified Al5183 alloy [293], the grains were significantly refined and the hardness increased, yet the tensile property became worse due to the extensive formation of pores.

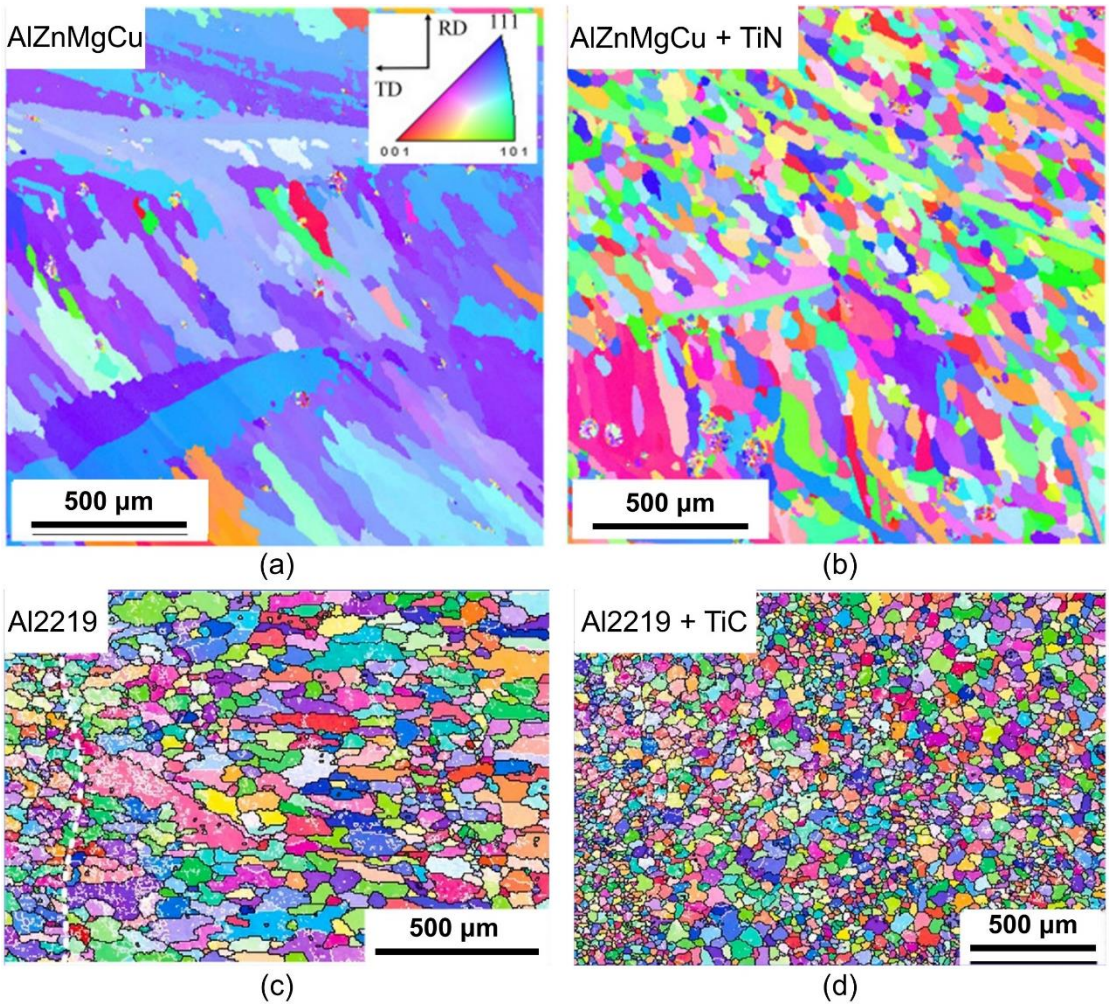

Fig. 45. Microstructure of wire-arc additive manufacturing aluminum matrix composites. Electron backscattered diffraction images of (a) AlZnMgCu and (b) TiN-modified AlZnMgCu [243]. (c) Al2219 and (d) TiC-modified Al2219 [292].

6.2.4 Additive friction stir deposition

Recently, AFSD technology has also been implemented to fabricate AMCs [20,294,295]. However, work in this area remains limited. The feedstock materials can be taken in the following three forms: (i) a pre-alloyed metal matrix rod containing the desired ceramic or oxide particles; (ii) Al alloys and the reinforcement particles; or (iii) both the Al alloys and the reinforcements in powder forms, which are supplied using multiple hollows (Fig. 46a) [20]. Griffiths et al. [20] have demonstrated the feasibility of fabricating Al–20 vol. % SiC composites based on starting Al powders and SiC powders. The SEM image of AFSD Al–20 vol.% SiC (Fig. 46b) shows the uniform distribution of SiC in the Al matrix. The X-ray micro-tomography result (Fig. 46c) shows no obvious evidence of porosity.

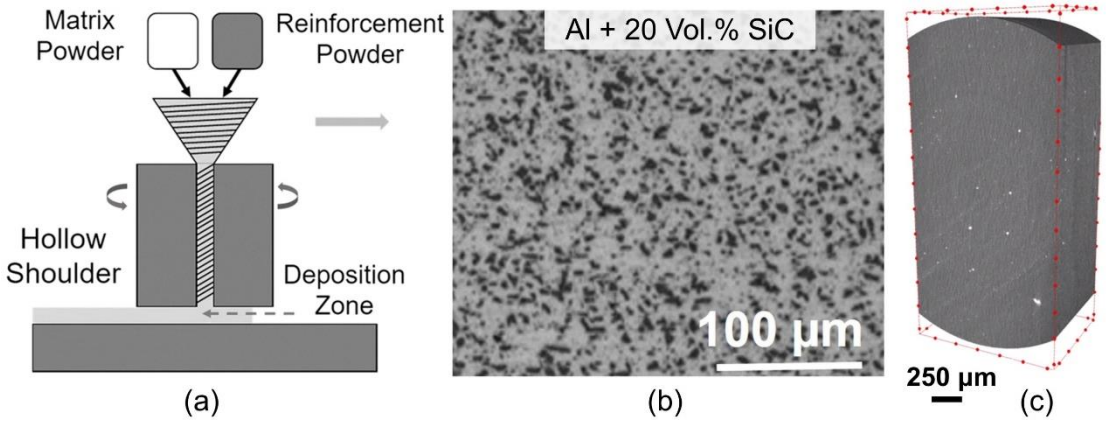

Fig. 46. Microstructure and densification of additive friction stir deposition aluminum matrix composites [20]**.** (a) Schematic graph of additive friction stir deposition process to fabricate the metal matrix composite based on the matrix and reinforcement powders. (b) Optical image and (c) X-ray tomography of additive friction stir deposition Al–20 Vol. % SiC composite.

6.3 Advantages and limitations

As discussed previously, the L-PBF technology shows the advantages of uniform dispersion of reinforcement particles into the matrix assisted by the Marangoni effects and the recoil pressure. However, it also shows some limitations. Firstly, poor wettability between the reinforcement particles and the Al matrix normally leads to weak interfacial bonding, leading to the formation of defects [296]. Xie et al. [296] have

found that increasing the laser power could enhance the wettability between the SiCp and Al, contributing to the improvement of densification. Secondly, the chemical reaction between the reinforcement particles with the matrix may cause the loss of reinforcement particles [297]. Liao et al. [297] have found that the loss of Al_2O_3 can be attributed to the chemical reaction between Al and Al_2O_3, resulting in the formation of gaseous Al_2O.

As to the AFSD technology, it could circumvent the cracking issues associated with fusion-based AM technologies and guarantee the uniform distribution of reinforcement particles. However, it has poor resolution due to the large size of the tools used. Furthermore, the volume fraction of the reinforcement particles is limited since increasing the volume fraction of the particles would lead to a reduction in flowability [20].

7. Products and applications of additive manufacturing aluminum alloys

Compared to traditional subtractive manufacturing technologies, AM can afford the advantages of designing complex-shaped components and reducing waste as well as a short leading time, and it has drawn significant attention in the high-profile aerospace industry [2]. Furthermore, AM has the advantage of designing lightweight structures and part consolidation, which can reduce the joining processes and the resultant cost. With rapid development, there is a range of commercialized Al alloy powders, including the Al [63,298], Al–Si alloys (Al−12Si [299], AlSi10Mg [300], A357 [300], AlSi9Cu3 [301], Al–Cu [170,285,286,302], Al–Mg [303], Al–Mg–Si [287,304], and Al–Zn [104,288,289] powders. the yield strength of L-PBF Al alloys is plotted in Fig. 47. The detailed properties and target applications for the L-PBF samples based on the listed powders are shown in Table A. 14. It is the L-PBF commercialized Al alloys show broad applications in the aerospace industry.

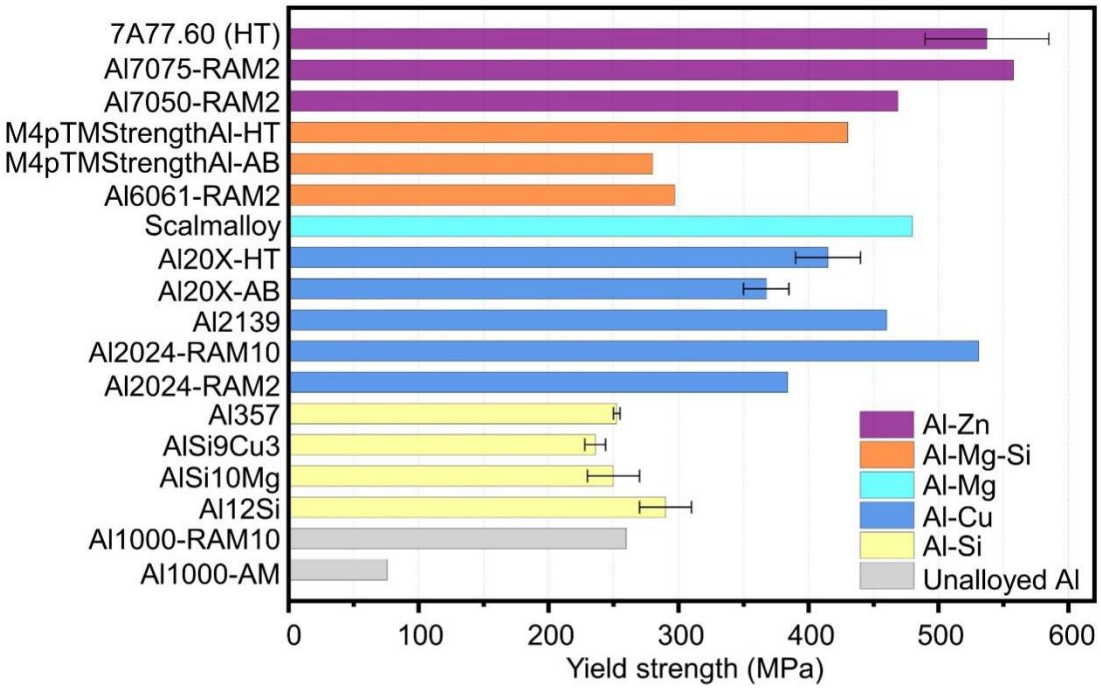

Fig. 47. Yield strength of laser powder bed fusion commercialized aluminum alloys. The data are cited from Ref. [63,104,170,285-289,300-304].

Due to the development of novel AM-specific Al powders and the associated advantages, such as high functionality and production efficiency, the additive manufacturing-fabricated Al alloys show potential applications in various fields, including the aerospace and automobile sectors. Up to now, the fabrication of Al alloys for industrial applications has mainly relied on L-PBF, and the fabrication of Al alloys via LP-DED, WAAM, and BJ has been limited [305]. To the best of the author's knowledge, there is no report on the products of EB-PBF and AFSD Al alloys for practical applications. Thus, this section emphasizes L-PBF with a brief review of LP-DED, WAAM, and BJ fabricated Al products. According to their applications in different areas, such as aerospace & space and automotive, some of the products are presented in Fig. 48. Fig. 48a shows the bionic partition manufactured by APWorks using the Scalmalloy®[306]. This leads to a 45% weight reduction due to the design optimization and the use of Scalmalloy®, which could contribute to fuel savings and reduction of CO_2 emission. Fig. 48b shows an additively manufactured topologically optimized antenna bracket for Sentinel satellites using EOS AlSi10Mg powders [307].

The weight of the L-PBF bracket is 940 g compared to 1.6 kg for the conventionally fabricated counterparts. Fig. 48c presents WAAM Al panels that can be used for building airplane fuselages [308]. Fig. 48d shows the Al spare parts, a thermostat cover for trucks and Unimog models from older model series fabricated via L-PBF technology by Mercedes Benz Trucks [309]. Fig. 48e shows the serially manufactured parts for the BMW i8 [310], which could reduce the weight and autonomy in electric or hybrid vehicles. Fig. 48f shows the BJ Al6061 engine block with high resolution and geometric control [26]. Fig. 48g shows an L-PBF electric motorcycle frame printed by APWORKS using the Scalmalloy® [14]. Fig. 48h shows L-PBF skate blades using AlMgSc by Farsoon Technologies. The 3D-printed skate blades exhibit better flexibility due to weight reduction, offering smoother and better ice grip at cornering and sharp turns [311]. Fig. 48i shows an L-PBF fabricated Al6061–RAM2 heat sink that has been blasted using a glass bead [287]. Fig. 48j shows a piston head fabricated using high-strength and ductile A2024–RAM2 [285]. Fig. 48k shows an LP-DED Al alloy block with a relative density higher than 99% [312]. The above successful adoptions of AM Al alloys for industrial applications indicate that AM holds great potential for future applications.

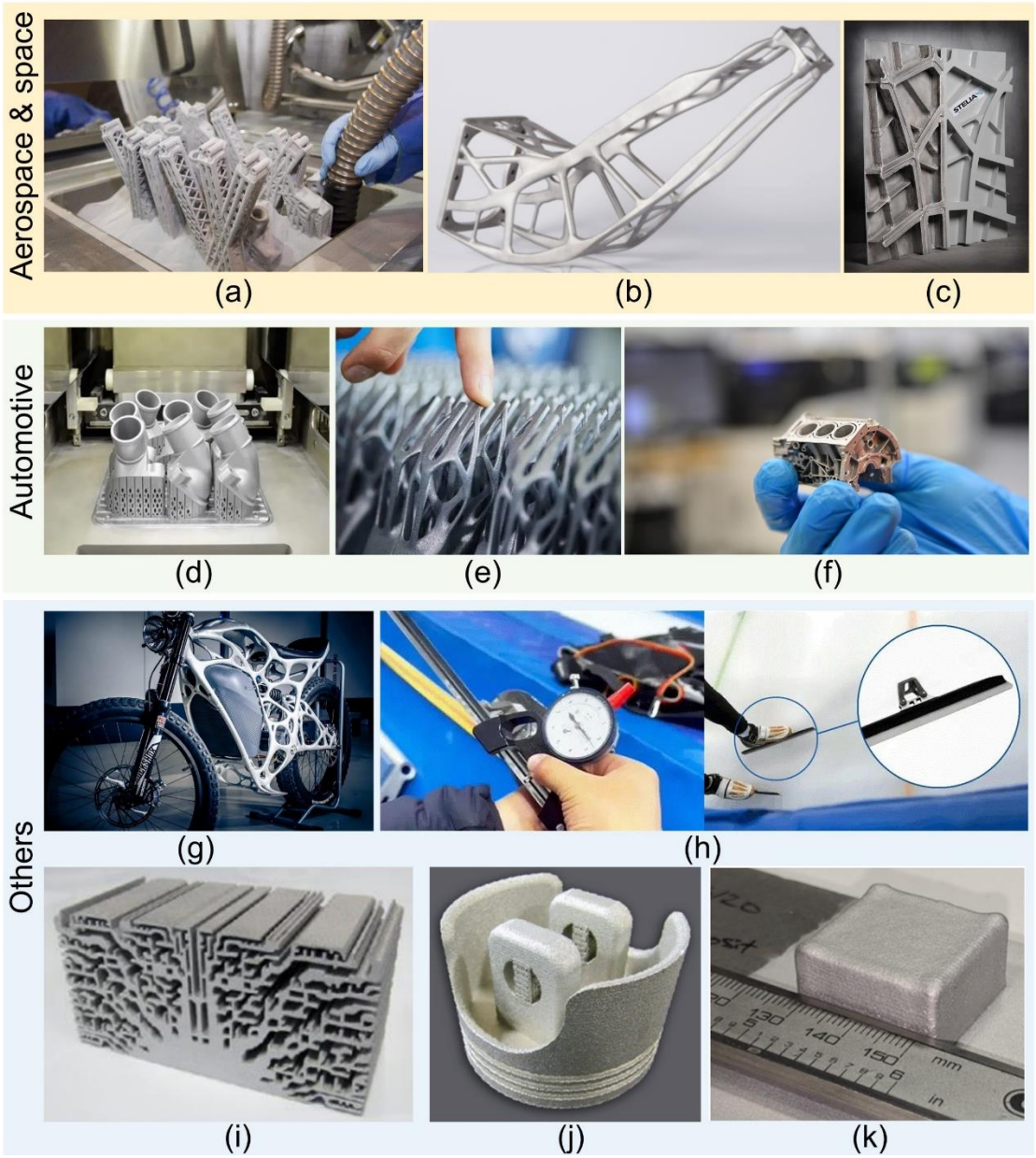

Fig. 48. Products of additive manufacturing aluminum alloys. (a) A Scalmalloy® bionic aircraft partition printed by APWORKS, Airbus Group, Ottobrunn [306]. (b) The topologically optimized antenna bracket for sentinel satellites with EOS Aluminum AlSi10Mg using additive manufacturing [307]. (c) Wire-arc additive manufacturing Al fuselage panel [308]. (d) Laser powder bed fusion Al spare parts by Mercedes Benz Trucks [309]. (e) Serially manufactured parts for the BMW i8 [310]. (f) Binder jetting Al6061 engine block [26]. (g) An electric motorcycles frame, also printed by APWORKS using its Scalmalloy® alloy [14]. (h) Skate blades fabricated with AlMgSc via laser powder bed fusion [311]. (i) Laser powder bed fusion heat sink using A6061–RAM2. The component is blasted using a glass bead [287]. (j) Laser powder bed fusion

piston head using A2024–RAM2 [285]. (k) Laser powder direct energy deposition Al block with high density [312].

Another obvious advantage of L-PBF technology is the design of a lattice structure, which could fabricate a cellular structure with designed geometry [313]. It has been proven that a porous structure with a repeated geometry of octet-truss unit cells exhibits a significant enhancement in nucleate boiling heat transfer due to increased surface area for L-PBF AlSi10Mg [314]. Furthermore, Broughton et al. [315] have shown that L-PBF AlSi10Mg alloys with a cellular structure can show an approximately 60% enhancement of effective heat transfer coefficient compared with those of metal foams with stochastic porous structures. These results indicate that L-PBF Al alloys with cellular structures can have potential applications as heat exchangers.

8. Conclusions

The current state of the art in the additive manufacturing of Al alloys was reviewed, focusing on processing with different additive manufacturing technologies, including laser powder bed fusion and electron beam powder bed fusion, laser powder direct energy deposition, wire-arc additive manufacturing, and additive friction stir deposition. The classifications of additive manufacturing technologies and Al alloys were listed. Then, the "processing-microstructure-mechanical property" relationship of the fabricated Al alloys was introduced. The conclusions of the review can be drawn as follows:

(1) Melt-based and solid-state-based additive manufacturing have been adopted to fabricate Al and Al alloys. Among melt-based additive manufacturing, laser powder bed fusion takes the largest portion, and Al–Si alloys are the most investigated alloy systems for additive manufacturing.

(2) Laser powder bed fusion Al–Si alloys exhibit coarse columnar grains along the build direction and a heterogeneous structure containing cells with a boundary rich in Si. The microstructure and mechanical properties of laser powder bed fusion Al–Si alloys are

tuneable by tailoring the orienting parameters. laser powder bed fusion Al–Si alloys exhibit a higher yield strength relative to that of cast counterparts due to the microstructure refinement arising from the rapid cooling process.

(3) It remains challenging to print highly dense and crack-free high-strength Al alloys with laser powder bed fusion, such as Al–Cu, Al–Mg–Si, and Al–Zn alloys, due to the formation of cracks. The functionalization with micron- or nano-powders, such as Ti, Zr, Sc, and Ta, has been adopted to improve the printing ability. The crack healing is ascribed to the formation of the Al_3X (X = Ti, Zr, Sc, and Ta) phase coherent with the Al matrix, which refines the grains to prevent crack propagation. With grain refinement, laser powder bed fusion high-strength Al alloys exhibit higher yield strengths relative to those of conventionally fabricated Al counterparts.

(4) The microstructure and mechanical properties of laser powder bed fusion Al alloys are tuneable via post heat treatment. Due to the special microstructure, the heat treatment profiles need to be redesigned to achieve the desired microstructure and high performance.

(5) The fabrication of Al alloys using other additive manufacturing technologies is rare compared with those using laser powder bed fusion:

(i) Electron beam powder bed fusion has the advantage of fabricating Al alloys since it can rule out the possibility of oxidation, and it has been adopted to fabricate AlSi10Mg, Al–Cu, and Al–Zn alloys. The EB-PBF fabricated AlSi10Mg alloy exhibited superior ductility and could exhibit precipitation hardening after heat treatment.

(ii) The AlSi10Mg alloy and Scalmalloy® have been fabricated via laser powder direct energy deposition technology. The laser powder direct energy deposition AlSi10Mg exhibited a heterogeneous microstructure along the build direction due to the varied thermal history, while the laser powder direct energy deposition Scalmalloy®exhibited bimodal grain size distribution containing coarse and fine grains.

(iii) Wire-arc additive manufacturing has been implemented to fabricate Al alloy with a heterogeneous microstructure. The microstructure of as-built Al alloy is sensitive to the composition and printing conditions.

(iv) Solid-state additive friction stir deposition technology could potentially fabricate

high-strength Al–Cu and Al–Mg–Si alloys, which tend to form cracks when processed via melt-based additive manufacturing. The grain structure and precipitation behaviour of additive friction stir deposition Al alloys are sensitive to the processing parameters. The tensile properties of additive friction stir deposition fabricated Al7075 are comparable to those of wrought counterparts.

(6) Additive manufacturing technologies could fabricate the Al alloy matrix composite via an in-situ method. Introduced ceramics can achieve either grain refinement to heal cracks or provide a strengthening source.

9. Outlook

With the more important role that AM technologies are playing in industry, the adoption of AM for Al alloys is increasing, and AM is transiting from prototyping to a higher batch production technology. However, additional scientific and technological research needs to overcome the challenges to broaden the applications of AM for Al alloys and we propose the following points deserving further investigation, which are listed in Fig. 49. The outline mainly includes the novel processing methods, novel alloys, novel structure, and understanding of the process–microstructure–property relationship. Detailed perspectives are given below:

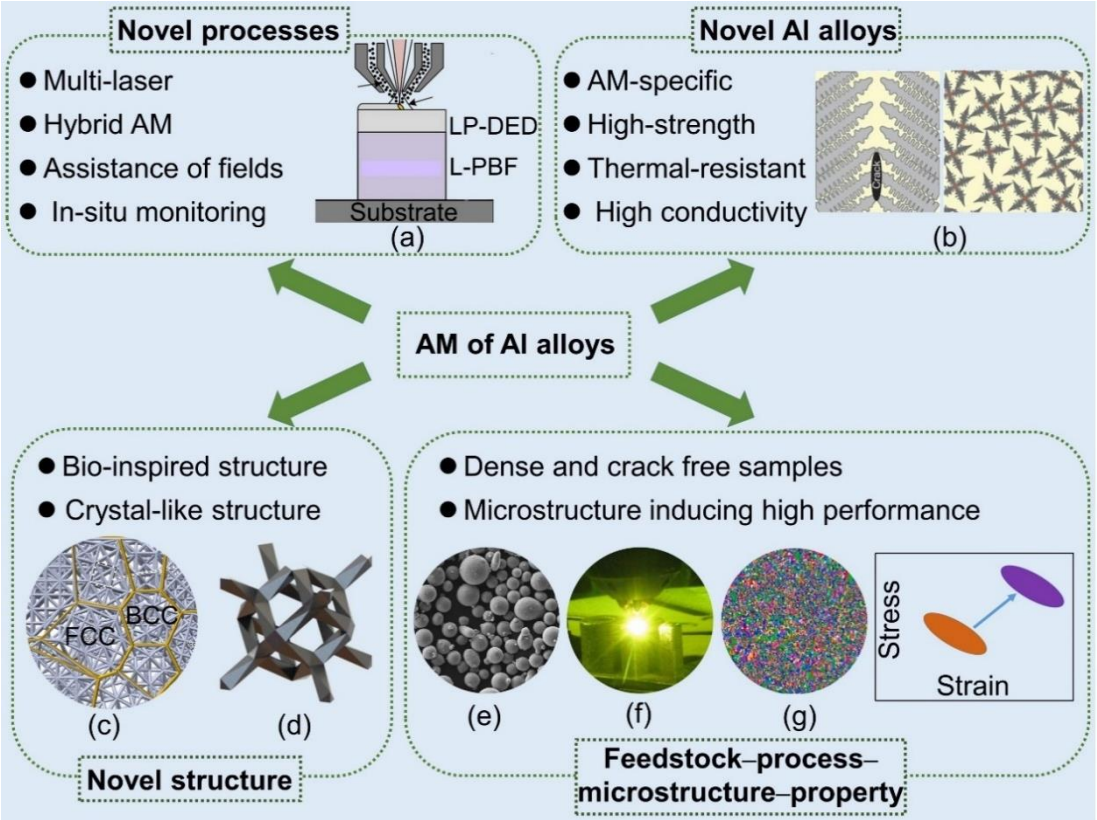

Fig. 49. Outline of development perspectives for the additive manufacturing of aluminum alloys, including novel processing methods, novel alloys, novel structure, and process-microstructure-property relationship. (a) The schematic graph of hybrid manufacturing [316]. (b) developing novel alloys with Ref. [10]. (c) Crystal-inspired cellular structure [317]. (d) Single unit cell for cellular structure [318]. (e) Powders for laser powder bed fusion [102]. (f) Image of laser powder direct energy deposition process [319]. (g) Electron backscattered diffraction of laser powder bed fusion Ti-modified Al2024 [96].

9.1 Novel processing methods

As discussed, the main AM technologies for fabricating Al alloys rely on the L-PBF technology, while LP-DED, EB-PBF, BJ, WAAM, and AFSD technologies are relatively less common. Recently, hybrid AM technologies, taking advantage of each technology, have been adopted to process Al alloys to achieve balanced properties, such as surface roughness, forming accuracy, and size [316]. L-PBF/LP-DED hybrid AM technologies can fabricate samples using L-PBF where surface roughness/complex

geometry is needed and using LP-DED where simple geometry is needed [316]. Apart from hybrid AM technologies, multi-laser is an effective way to enhance the fabrication efficiency for L-PBF [320]. Furthermore, stirring fields [321,322], such as static magnetic fields and ultrasonic fields, are used to affect the solidification process and tailor the microstructure.

9.2 Novel alloy development

Due to the special characteristics associated with AM, such as the rapid heating/cooling rate during L-PBF, the preheating and vacuum during EB-PBF, and the higher deposition rate during LP-DED, it is necessary to develop AM-specific Al alloys. This is achieved through either enhancing the printability (readily printed Al alloys) or pursuing high performance. Improving printability can be achieved through alloy design that enables the reduction of a fraction of porosity or cracks. High mechanical performance design can be achieved by incorporating various strengthening mechanisms (grain boundary strengthening, dislocation strengthening, and precipitation strengthening), or deformation mechanisms.

Another aspect of novel alloy development is targeted for elevated temperature applications. At present, pioneering initial work is being undertaken on the L-PBF of high-temperature Al alloys, while the exploration of thermal-resistant Al alloys via other AM technologies still needs to be explored further.

9.3 Novel structure

The design freedom afforded by AM can provide an opportunity to fabricate novel structures, such as bio-inspired and crystal-like structures. This provides a tremendous opportunity to design lightweight structures, that have extensive applications in the aerospace industry.

Moreover, the advantages of powder-blown LP-DED can be taken into account to

fabricate the multi-materials [323] or functionally graded materials [324], which enable the development of alloys with tailored properties to meet special application demands [325]. It would be beneficial to develop multi-materials or functionally graded materials containing Al to broaden their application.

9.4 Feedstock–process–microstructure–property relationship

As the starting materials, the quality of feedstock materials plays a significant role in influencing the printing quality as well as the microstructure and properties of the output product. Subsequently, the microstructure and mechanical properties are influenced by the printing parameters and post-heat treatment profiles. Taking the L-PBF process as an example, the feedstock powders and coupons as well as components are connected via manufacturing (Fig. 50). Each step is critical for ensuring high-quality printing and high mechanical performance. The detailed perspectives of each step are described in turn in detail below.

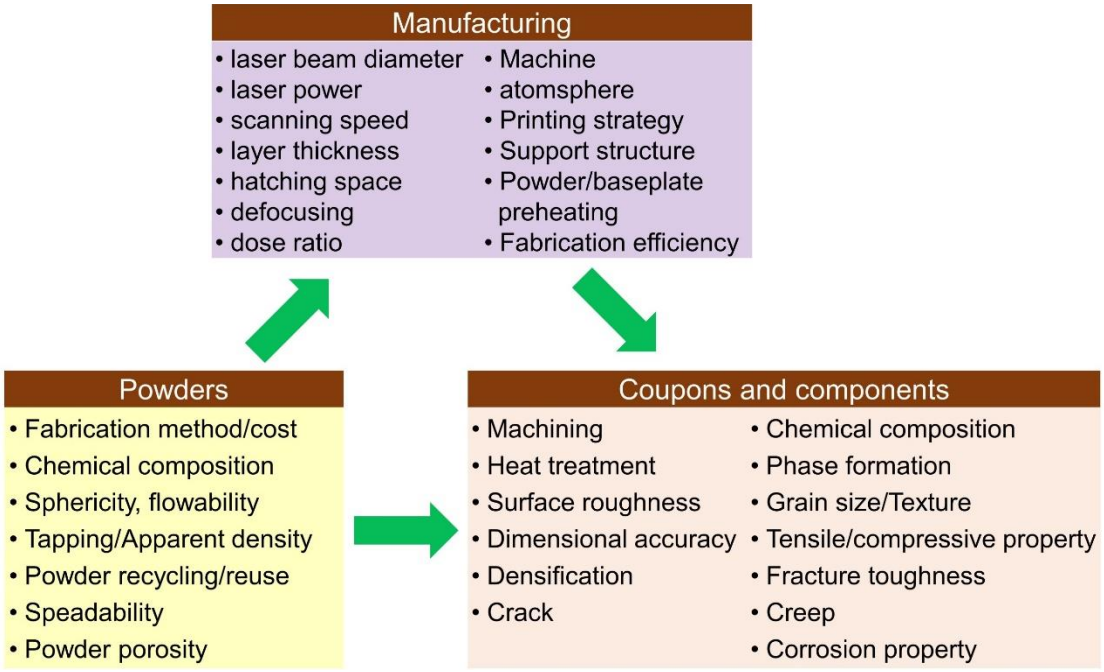

Fig. 50. A schematic graph showing the relationship among "powders–manufacturing–coupons and components".

(1) Quality and cost of feedstock

The high cost of powders limits the broad application of AM to fabricate Al alloys [326].

Thus, reducing the cost of powders would enable the broadening of industrial applications of AM. A reduction of the cost of powder could be achieved through powder recycling, improved fabrication methods, or cost-effective raw materials. However, all of these methods need to be built on the basis that the quality of powders is not compromised, and competitive mechanical performance can be achieved.

(2) Broadening the processing map to enhance performance

At present, there remains processing space for enhancing the mechanical properties since the processing map is not broad enough. Taking the L-PBF of Al–Si alloys as an example, the strength reported hitherto is limited. The uncompetitive mechanical strength is partially due to a lack of strengthening mechanisms, and due to the fact that the processing map is not broad enough to induce novel microstructure and high mechanical performance. Given that a number of factors could influence the microstructure and mechanical performance of printed parts, such as the laser characteristics [327], powder quality, printing parameters (laser power, scanning speed, layer thickness, hatch spacing, baseplate preheating, et al.) [328] as well as strategy, and post heat treatment, recently emergent machine learning coupled with high throughput experiments can be adopted to identify the optimized parameters engendering the desired mechanical performance [329]. This machine learning-assisted printing parameter development sheds light on developing AM-specific Al alloys and exploring the relevant printing parameters.

(3) Post-treatment study for AM-specific Al alloys

Due to the novel microstructure associated with the processing route (rapid cooling rate and thermal recycling) [330] and composition modification, it is necessary to develop novel heat treatment profiles instead of conventional heat treatment to trigger enhanced performance. Until now, systematic heat treatment studies have been conducted for L-PBF Al–Si alloys, while such research is limited for Al–Cu, Al–Mg, Al–Mn, Al–Mg–Si, and Al–Zn alloys to trigger high performance. Apart from heat treatment, surface enhancement and the introduction of the pre-strain are also promising ways to extend

the application of AM parts [331].

(4) Systematic study on the properties of additive manufacturing aluminum alloys

Based on the present understanding, the hot cracking issues encountered during L-PBF of moderate- and high-strength Al alloys, such as Al–Cu, Al–Mg, Al–Mn, Al–Mg–Si, and Al–Zn alloys, can be healed via inoculation treatment, such as the introduction of Zr, Sc, and Ti. However, more properties of compositionally modified Al alloys targeted for application, need to be characterized, including the mechanical properties beyond the quasi-static tensile property (such as creep, fatigue, and fracture toughness tests) as well as the functional properties (corrosion and wear properties). The relevant studies in this area are still limited but are necessary to guarantee safe application.

Apart from the mechanical and corrosion properties, investigations into the functional properties, such as thermal conductivity, electric conductivity, and thermal expansion, are rare. Recently, Pauzon et al. [332] have reported an Al–Fe–Zr alloy fabricated via L-PBF with a superior strength-conductivity trade-off. Developing such alloys could have potential heat exchanger applications.

Finally, since AM technology includes a complex chain, including the powder manufacturer, the machine supplier, and the end-users, it would be beneficial if more collaborations are built among the various actors. With detailed demands from the end-users, AM researchers could have the clear goal to develop specific structures or properties catering to specific practical applications.

Data availability statement

The raw/processed data required to reproduce these findings cannot be shared at this time because this is a review article, and it was taken from the published literature.

Declaration of Competing Interest

The authors declare that they have no known competing financial interests or personal relationships that could have appeared to influence the work reported in this paper.

Acknowledgements

The financial support from the A*STAR Structural and Metal Alloys Programme (SMAP): Work Package II with project No. A18B1b0061 is acknowledged.

References

[1] T. DebRoy, H. L. Wei, J. S. Zuback, T. Mukherjee, J. W. Elmer, J. O. Milewski, A. M. Beese, A. W. Heid, A. De, W. Zhang, Additive manufacturing of metallic components - Process, structure and properties, Prog. Mater. Sci. 2018;92: 112-224.

[2] D. D. Gu, X. Y. Shi, R. Poprawe, D. L. Bourell, R. Setchi, J. H. Zhu, Material-structure-performance integrated laser-metal additive manufacturing, Science 2021; 372: 932.

[3] T. H. Becker, P. Kumar, U. Ramamurty, Fracture and fatigue in additively manufactured metals, Acta Mater. 2021;219:117240.

[4] C. L. Tan, F. Weng, S. Sui, Y. X. Chew, G. J. Bi, Progress and perspectives in laser additive manufacturing of key aeroengine materials, Int. J. Mach. Tool Manufact. 2021;170: 103804.

[5] D. D. Gu, M. J. Xia, D. H. Dai, On the role of powder flow behavior in fluid thermodynamics and laser processability of Ni-based composites by selective laser melting, Int. J. Mach. Tool Manufact. 2019;137:67-78.

[6] S. Sanchez, P. Smith, Z. K. Xu, G. Gaspard, C. J. Hyde, W. W. Wits, I. A. Ashcroft, H. Chen, A. T. Clare, Powder bed fusion of nickel-based superalloys: A review, Int. J. Mach. Tool Manufact. 2021;165: 103729.

[7] J. P. Oliveira, T. G. Santos, R. M. Miranda, Revisiting fundamental welding concepts to improve the additive manufacturing: from theory to practice, Prog. Mater. Sci. 2020;107:100590.

[8] N. Tuncer, A. Bose, Solid-state metal additive manufacturing: A review, JOM 2020;9:72.

[9] J. R. Davis, ASM Specialty Handbook: Aluminum and Aluminum alloys, ASM International 1993.

[10] J. H. Martin, B. D. Yahata, J. M. Hundley, J. A. Mayer, T. A. Schaedler, T. M.

Pollock, 3D printing of high-strength aluminum alloys, Nature 2017;549: 365.

[11] J. R. Croteau, S. Griffiths, M. D. Rossell, C. Leinenbach, C. Kenel, V. Jansen, D. N. Seidman, D. C. Dunand, N. Q. Vo, Microstructure and mechanical properties of Al-Mg-Zr alloys processed by selective laser melting, Acta Mater. 2018;153:35-44.

[12] E. O. Olakanmi, R. F. Cochrane, K. W. Dalgarno, A review on selective laser sintering/melting (SLS/SLM) of aluminum alloy powders: Processing, microstructure, and properties, Prog. Mater. Sci. 2015; 74: 401-477.

[13] I. M. Kusoglu, B. Gökce, S. Barcikowski, Research trends in laser powder bed fusion of Al alloys within the last decade, Addit. Manuf. 2020;36:101489.

[14] https://www.3dprintingmedia.network/aluminum-alloys-additive-manufacturing/, accessed on 12th June 2022.

[15] J. Marczyk, K. Ostrowska, M. Hebda, Influence of binder jet 3D printing process parameters from irregular feedstock powder on final properties of Al parts, Adv. Powder Technol. 2022;33:103768.

[16] Metal additive manufacturing report, AMPOWER Report2020, https://www.additive-manufacturing-report.com, accessed on 10th, Oct. 2022.

[17] M. S. Kenevisi, Y. F. Yu, F. Lin, A review on additive manufacturing of Al-Cu (2xxx) aluminum alloys, process, and defects, Mater. Sci. Technol. 2021;37:805-829

[18] A. Wang, H. Z. Wang, Y. Wu, H. W. Wang, 3D printing of aluminum alloys using laser metal deposition: a review, Int. J. Adv. Manuf. 2021;116:1-37.

[19] B. O. Omiyale, T. O. Olugbade, T. E. Abioye, P. K. Farayibi, Wire arc additive manufacturing of aluminium alloys for aerospace and automotive applications: a review, Mater. Sci. Technol. 2022;38:391-408.

[20] R. J. Griffiths, M. E. J. Perry, J. M. Sietins, Y. H. Zhu, N. Hardwick, C. D. Cox, H. A. Rauch, H. Z. Yu, A perspective on solid-state additive manufacturing of aluminum matrix composites using MELD, J. Mater. Eng. Perform. 2019;28:648-656.

[21] Z. Li, S. Sui, X. Ma, H. Tan, C. L. Zhong, G. J. Bi, A. T. Clare, A. Gasser, J. Chen, High deposition rate powder- and wire-based laser directed energy deposition of metallic materials: A review, Int. J. Machine Tools Manuf. 2022;181:103942.

[22] A. Mostafaei, A. M. Elliott, J. E. Barnes, F. Z. Li, W. D. Tan, C. L. Cramer, P.

Nandwana, M. Chmielus, Binder jet 3D printing-Process parameters, materials, properties, modeling, and challenges, Prog. Mater. Sci. 2021;119:100707.

[23] M. Krinitcyn, N. Toropkov, A. Pervikov, M. Lerner, Structure and mechanical properties of Fe-10Cu alloy obtained by material extrusion-based additive manufacturing method with bimodal powder, Powder Technol. 2022;406: 117593.

[24] M. Jurisch, T. Studnitzky, O. Andersen, B. Kieback, 3D screen printing-Additive manufacturing of finely structured titanium based parts, World PM 2016 Confer. Exhib. 2016.

[25] Y. Lakhdar, C. Tuck, J. Binner, A. Terry, R. Goodridge, Additive manufacturing of advanced ceramic materials, Prog. Mater. Sci. 2021;116:100736.

[26] https://www.exone.com/en-US/Resources/news/ExOne-and-Ford-deliver-aluminum-breakthrough, Accessed on 15th Oct. 2022.

[27] R.R. Dehoff, S. S. Babu, Characterization of interfacial microstructures in 3003 aluminum alloy blocks fabricated by ultrasonic additive manufacturing, Acta Mater. 2010;58:4305-4315.

[28] H. Z. Yu, R. S. Mishra, Additive friction stir deposition: a deformation processing route to metal additive manufacturing, Mater. Res. Lett. 2021;9:71-83.

[29] L. Ajdelsztajn, J. M. Schoenung, B. Jodoin, G. E. Kim, Cold spray deposition of nanocrystalline aluminum alloys, Metal. Mater. Trans. 2005;36: 657-666.

[30] X. M. Wang, F. Feng, M. A. Klecka, M. D. Mordasky, J. K. Garofano, T. EI-Wardany, A. Nardi, V. K. Champagne, Characterization and modeling process in cold spray additive manufacturing, Addit. Manuf. 2015;8:149-162.

[31] A. R. McAndrew, M. A. Rosales, P. A.Colgrove, J. R. Hönnige, A. Ho, R. Fayolle, K. Eyitayo, I. Stan, P. Sukrongpang, A. Crochemore, Z. Pinter, Interpass rolling of Ti-6Al-4V wire + arc additively manufactured features for microstructural refinement, Addit. Manuf. 2018;21:340-349.

[32] D. H. Ding, Z. X. Pan, D. Cuiuri, H. J. Li, Wire-feed additive manufacturing of metal components: technologies, developments and future interests, Int. J. Adv. Manuf. Technol. 2015;81:465-481.

[33] S. Nachum, J. Vogt, F. Rarther, Additive manufacturing of ceramics:

Stereolithography versus binder jetting, CFI-Ceram. Forum Int. 2016;3:27-33.

[34] H. Miyanaaji, K. M. Rahman, M. Da, C. B. Williams, Effect of fine powder particles on quality of binder jetting parts, Addit. Manuf. 2020;36:101587.

[35] M. Ziaee, N. B. Crane, Binder jetting: A review of process, materials, and methods, Addit. Manuf. 2019;28:781-801.

[36] https://www.eos.info/en, Accessed on April 23, 2020.

[37] P. Sun, Z. G. Zak Fang, Y. Zhang, Y. Xia, Review or the methods for production of spherical Ti and Ti alloy powder, JOM 2017;69:1853-1860.

[38] S. Gorsse, C. Hutchinson, M. Gouné, R. Banerjee, Additive manufacturing of metals: a brief review of the characteristic microstructures and properties of steels, Ti-6Al-4V and high entropy alloys, Sci. Technol. Adv. Mater. 2017;18:584-610.

[39] A. Singh, S. Kapil, M. Das, A comprehensive review of the methods and mechanisms for powder feedstock handling in directed energy deposition, Addit. Manuf. 2020;35:101388.

[40] E. Davoodi, H. Montazerian, A. S. Mirhakimi, M. Zhianmanesh, O. Ibhadode, S. I. Shahabad, R. Esmaeilizadeh, E. Sarikhani, S. Toorandaz, S. A. Sarabi, R. Nasiri, Y. Z. Zhu, J. Kadkhodapour, B. B. Li, A. Khademhosseini, E. Toyserkani, Additively manufactured metallic biomaterials, Bio. Mater. 2022;15:214-249.

[41] B. Zhou, J. Zhou, H. Li, F. Lin, Fabrication and characterization of Ti6Al4V by selective electron beam and laser hybrid melting, In: Proceedings of the 28th Annual International-Solid Freeform Fabrication Symposium 20171924-1934.

[42] M. Galati, G. Rizza, S. Defanti, L. Denti, Surface roughness prediction model for electron beam melting (EBM) processing Ti6Al4V, Pre. Eng. 2021;69: 19-28.

[43] H. Z. Yu, M. E. Jones, G. W. Brady, R. J. Griffiths, D. Garcia, H. A. Rauch, C. D. Cox, N. Hardwick, Non-beam-based metal additive manufacturing enabled by additive friction stir deposition, Scr. Mater. 2018;153:122-130.

[44] R. Baker, Method of making decorative articles. U. S. Pat. 1925:1-3.

[45] L. P. Raut, R. V. Taiwade, Wire arc additive manufacturing: A comprehensive review and research directions, J. Mater. Eng. Perform. 2021;30:4768-4791.

[46] C. R. Cunningam, J. M. Flynn, A. Shokrani, V. Dhokia, S. T. Newman, Invited

review article: Strategies and processes for high quality wire arc additive manufacturing, Addit. Manuf. 2018;22: 672-686.

[47] W. S. W. Harun, M. S. I. N. Kamariah, N. Muhamad, S. A. C. Ghani, F. Ahmad, Z. MohAM, A review of powder additive manufacturing processes for metallic biomaterials, Powder Technol. 2018;327:128-51.

[48] M. Brandt, The role of lasers in additive manufacturing, in: M. Brandt (Ed.), Laser Additive Manufacturing, Woodhead Publishing 2017, pp. 1-18.

[49] I. Yadroitsev, I. Yadriotsava, A. Du Plessis, E. Macdonald, Fundamentals of laser powder bed fusion of metals, first ed., 2021.

[50] Optomec Overview. https://optomec.com/optomec-overview, Accessed on 22nd 2022.

[51] M. Forend, V. Ventzke, N. Kashaev, J. Enz, Thermal analysis of wire-based direct energy deposition of Al-Mg using different laser irradiances, Addit. Manuf. 2019;29: 100800.

[52] L. E. Andersson, M. Larsson, Device and arrangement for producing a three-dimensional object, Patent WO 2001081031 A1, 2001.

[53] M. Galati, L. Luliano, A literature review of powder-based electron beam melting focusing on numerical simulations, Addit. Manuf. 2018;19:1-20.

[54] K. Kandasamy, Solid state joining using additive friction stir processing, United States Patent, Assignee: MELD Manufacturing Corporation. 2016; US9511445B2.

[55] R. S. Mishra, Z. Y. Ma, Friction stir welding and processing, Mater. Sci. Eng. R 2005;50:1-78.

[56] S. C. Beck, B. A. Rutherford, D. Z. Avery, B. J. Phillips, H. Rao, M. Y. Reckha, L. N. Brewer, P. G. Allison, J. B. Jordon, The effect of solutionizing and artificial aging on the microstructure and mechanical properties in solid-state additive manufacturing of precipitation hardened Al-Mg-Si alloy, Mater. Sci. Eng. A 2021;819:141351.

[57] D. Raabe, C. C. Tasan, E. A. Olivetti, Strategies for improving the sustainability of structural metals, Nature 2019;575: 64-74.

[58] H. R. Kotadia, G. Gibbons, A. Das, P. D. Howes, A review of laser powder bed fusion additive manufacturing of aluminum alloys: microstructure and properties, Addit.

Manuf. 2021;46:102155.

[59] N. T. Aboulkhair, M. Simonelli, L. Parry, I. Ashcroft, C. Tick, R. Hague, 3D printing of Aluminum alloys: additive manufacturing of aluminum alloys using selective laser melting, Prog. Mater. Sci. 2019;106: 100578.

[60] R. Ghiaasiaan, S. Shankar, Effect of alloy composition on microstructure and tensile properties of net-shaped castings of Al-Zn-Mg-Cu alloys, Int. J. Metal Casting 2019;13:300-310.

[61] T. Kimura, T. Nakamoto, Thermal and mechanical properties of commercial-purity aluminum fabricated using selective laser melting, Mater. Trans. 2017;58:799-805.

[62] J. H. Martin, B. Yahata, J. Mayer, R. Mone, E. Stonkevitch, J. Miller, M. R. O'Masta, T. Schaedler, J. Hundley, P. Callahan, T. Pollock, Grain refinement mechanisms in additively manufactured nano-functionalized aluminum, Acta Mater. 2020;200: 1022-1037.

[63] https://www.elementum3d.com/wp-content/uploads/2022/01/A1000-AM-Data-Sheets-2021-04-15.pdf, accessed on 25th. Sep. 2022.

[64] https://www.metals4printing.com/wp-content/uploads/2021/Data_Sheets/EN/Al-Base/04_m4p_DataSheet_PureAl_EN.pdf, accessed on 16th. Oct. 2022.

[65] C. M. Laursen, S. A. Dejong, S. M. Dickens, A. N. Exil, D. F. Susan, J. D. Carroll, Relationship between ductility and the porosity of additively manufactured AlSi10Mg, Mater. Sci. Eng. A 2020;795:139922.

[66] S. M. H. Hojjatzadeh, N. D. Parab, W. T. Yan, Q. L. Guo, L. H. Xiong, C. Zhao, M. L. Qu, L. I. Escano, X. H. Xiao, K. Fezzaa, W. Everhart, T. Sun, L. Y. Chen, Pore elimination mechanisms during 3D printing of metals, Nat. Commun. 2019;10:3088.

[67] S. M. H. Hojjatzadeh, N. D. Parab, Q. L. Guo, M. L. Qu, L. H. Xiong, C. Zhao, L. J. Escano, K. Fezza, W. Everhart, T. Sun, L. Y. Chen, Direct observation of pore formation mechanisms during LPBF additive manufacturing process and high energy density welding, Int. J. Mach. Tools 2020;153: 103555.

[68] Q. L. Guo, C. Zhao, L. I. Escano, Z. Young, L. H. Xiong, K. Fezzaa, W. Everhart, B. Brown, T. Sun, L. Y. Chen, Transient dynamics of powder spattering in laser powder

bed fusion additive manufacturing process revealed by in-situ high-speed high-energy x-ray imaging, Acta Mater. 2018;151:169-180.

[69] C. Zhao, N. D. Parab, X. X. Li, K. Fezzaa, W. D. Tan, A. D. Rollett, T. Sun, Critical instability at moving keyhole tip generates porosity in laser melting, Science 2020; 370: 1080-1086.

[70] Y. Yang, Y. Chen, J. X. Zhang, X. H. Gu, P. Qin, N. W. Dai, X. P. Li, J. P. Kruth, L. C. Zhang, Improved corrosion behavior of ultrafine-grained eutectic Al-12Si alloy produced by selective laser melting, Mater. Des. 146 (2018) 239-248.

[71] H. Hyer, L. Zhou, A. Mehta, S. Park, T. Huynh, S. T. Song, Y. L. Bai, K. Cho, B. McWilliams, Y. H. Sohn, Composition-dependent solidification cracking of aluminum-silicon alloys during laser powder bed fusion, Acta Mater. 2021;208:116698.

[72] A. Suzuki, T. Miyasaka, N. Takata, M. Kobashi, M. Kato, Control of microstructural characteristics and mechanical properties of AlSi12 alloy by processing conditions of laser powder bed fusion, Addit. Manuf. 2021;48:102383.

[73] S. Rakesh Ch, A. Raja, P. Nadig, R. Jayagathan, N. J. Vasa, Influence of working environment and built orientation on the tensile properties of selective laser melted AlSi10Mg alloy, Mater. Sci. Eng. A 2019;750:141-151.

[74] K. V. Yang, P. Rometsch, C. H. J. Davies, A. J. Huang, X. H. Wu, Effect of heat treatment on the microstructure and anisotropy in mechanical properties of A357 alloy produced by selective laser melting, Mater. Des. 2018;154:275-290.

[75] J. Wu, X. Q. Wang, W. Wang, M. M. Attallah, M. H. Loretto, Microstructure and strength of selectively laser melted AlSi10Mg, Acta Mater. 2016;117:311-320.

[76] L. Zhao, J. G. Santos Macías, L. Ding, H. Idrissi, A. Simar, Damage mechanisms in selective laser melted AlSi10Mg under as built and different post-heat treatment conditions, Mater. Sci. Eng. A 2019;764:138210.

[77] Q. Liu, H. K. Wu, M. J. Paul, P. D. He, Z. X. Peng, B. Gludovatz, J. J. Kruzic, C. H. Wang, X. P. Li, Machine-learning assisted laser powder bed fusion process optimization for AlSi10Mg: New microstructure description indices and fracture toughness, Acta Mater. 2020;201:316-328.

[78] H. X. Chen, S. Patel, M. Vlasea, Y. Zou, Enhanced tensile ductility of an additively

manufactured AlSi10Mg alloy by reducing the density of melt pool boundaries, Scr. Mater. 2022;221:114954.

[79] M. N. Liu, K. W. Wei, X. Y. Zeng, High power laser powder bed fusion of AlSi10Mg alloy: Effect of layer thickness on defect, microstructure and mechanical property, Mater. Sci. Eng. A 2022;842:143107.

[80] Y. X. Geng, Q. Wang, Y. M. Wang, Q. H. Zang, S. B. Mi, J. H. Xu, Y. K. Xiao, Y. Wu, J. H. Luan, Microstructural evolution and strengthening mechanism of high-strength AlSi8.1Mg1.4 alloy produced by selective laser melting, Mater. Des. 2022;28:110674.

[81] Z. H. Hu, X. J. Nie, Y. Qi, H. Zhang, H. H. Zhu, Cracking criterion for high strength Al–Cu alloys fabricated by selective laser melting, Addit. Manuf. 2021;37: 101709.

[82] G. Mathers, 11-Weld defects and quality control, in: Mathers (Ed.), The welding of aluminum and its alloys, Woodhead Publishing 2002;199-215.

[83] L. Zhou, H. Hyer, S. Park, H. Pan, Y. L. Bai, K. P. Rice, Y. H. Sohn, Microstructure and mechanical properties of Zr-modified aluminum alloy 5083 manufactured by laser powder bed fusion, Addit. Manuf. 2019;28:485-496.

[84] G. Del Guercio, D. G. McCartney, N. T. Aboulkhair, S. Robertson, R. Maclachlan, C. Tuck, M. Simonelli, Cracking behaviour of high strength AA2024 aluminum alloy produced by laser powder bed fusion, Addit. Manuf. 2022;54:102776.

[85] Y. Qi, H. Zhang, X. J. Nie, Z. H. Hu, H. H. Zhu, X. Y. Zeng, A high strength Al-Li alloy produced by laser powder bed fusion: Densification, microstructure, and mechanical properties, Addit. Manuf. 2020;35:101346.

[86] S. Z. Uddin, L. E. Murr, C. A. Terrazas, P. Morton, D. A Roberson, R.B. Wicker, Processing and characterization of crack-free aluminum 6061 using high-temperature heating in laser powder bed fusion additive manufacturing, Addit. Manuf. 2018;22 405-415.

[87] Y. Chen, C. W. Xiao, S. Zhu, Z. W. Li, W. X. Yang, F. Zhao, S. F. Yu, Y. S. Shi, Microstructure characterization and mechanical properties of crack-free Al-Cu-Mg-Y alloy fabricated by laser powder bed fusion, Addit. Manuf. 2022;58:103006.

[88] H. Zhang, H. H. Zhu, T. Qi, Z. H. Hu, X. Y. Zeng, Selective laser melting of high-

strength Al-Cu-Mg alloys: processing, microstructure and mechanical properties, Mater. Sci. Eng. A 2016;656:47-54.

[89] A. Mehta, L. Zhou, T. Huynh, S. Park, H. Hyer, S. T. Song, Y. L. Bai, D. D. Imholte, N. E. Woolstenhulme, D. M. Wachs, Y. H. Sohn, Additive Manufacturing and mechanical properties of the dense and crack free Zr-modified aluminum alloy 6061 fabricated by the laser-powder fusion, Addit. Manuf. 2021;41:101966.

[90] Z. G. Zhu, F. L. Ng, H. L. Seet, S. M. L. Nai, Selective laser melting of micron-sized niobium functionalized Al7075 alloy: element evaporation and grain refinement, Mater. Sci. Eng. A 2022;834:142595.

[91] T. T. Wang, Y. L. Wang, X. Yang, B. J. Chen, H. H. Zhu, Cracks and process control in laser powder bed fusion of Al-Zn-Mg alloy, J. Manuf. Process. 2022;81:571-579.

[92] W. Stopyra, K. Gruber, I. Smolina, T. Kurzynowki, B. Kuznicka, Laser powder bed fusion of AA7075 alloy: influence of process parameters on porosity and hot cracking, Addit. Manuf. 2020;35:101270.

[93] M. Rasch, J. Heberle, M. A. Dechet, D. Bartels, M. R. Gotterbarm, L. Klein, A. Gorunov, J. Schmidt, C. Körner, W. Peukert, M. Schmidt, Grain structure evolution of Al–Cu alloys in powder bed fusion with laser beam for excellent mechanical properties, Materials 2020;13:82.

[94] M. L. M. Sistiaga, R. Mertens, B. Vrancken, X. B. Wang, B. V. Hooreweder, J. P. Kruth, J. V. Humbeeck, Changing the alloy composition of Al7075 for better processability by selective laser melting, J. Mater. Process. Technol. 2016;238:437-445.

[95] M. Opprecht, J. P. Garandet, G. Roux, C. Flament, M. Soulir, A solution to the hot cracking problem for aluminium alloys manufactured by laser beam melting, Acta Mater. 2020;197:40-53.

[96] Q. Y. Tan, Z. Q. Fan, X. Q. Tang, Y. Yin, G. Li, D. N. Huang, J. Q. Zhang, Y. G. Liu, F. Wang, T. Wu, X. L.Yang, H. Huang, Q. Zhu, M. X. Zhang, A novel strategy to additively manufacture 7075 aluminum alloy with selective laser melting, Mater. Sci. Eng. A 2021;821:141638.

[97] Q. Y. Tan, J. Q. Zhang, Q. Sun, Z. Q. Fan, G. Li, Y. Yin, I. G. Liu, M. X. Zhang, Inoculation treatment of an additively manufactured 2024 aluminum alloy with

titanium nanoparticles, Acta Mater. 2020;196:1-16.

[98] K. V. Yang, Y. J. Shi, F. Palm, X. H. Wu, P. Rometsch, Columnar to equiaxed transition in Al-Mg(-Sc)-Zr alloys produced by selective laser melting, Scr. Mater. 2018;145:113-117.

[99] Y. Ekubaru, O. Gokcekaya, T. Ishimoto, K. Sato, K. Manabe, P. Wang, T. Nakano, Excellent strength-ductility balance of Sc-Zr-modified Al-Mg alloy by tuning bimodal microstructure via hatch spacing in laser powder bed fusion, Mater. Des. 2022;221:110976.

[100] S. Griffiths, M. D. Rossell, J. Croeatu, N. Q. Vo, D. C. Dunand, C. Leinenbach, Effect of laser rescanning on the grain microstructure of a selective laser melted Al-Mg-Zr alloy, Mater. Charact. 2018;143:34-42.

[101] M. Opprecht, J. P. Garandet, G. Roux, C. Flament, An understanding of duplex microstructures encountered during high strength aluminum alloy laser beam melting processing, Acta Mater. 2021;15:117024.

[102] Z. G. Zhu, F. L. Ng, H. L. Seet, W. J. Lu, C. H. Liebscher, Z. Y. Rao, D. Raabe, S. M. L. Nai, Superior mechanical properties of a selective-laser-melted AlZnMgCuScZr alloy enabled by a tunable hierarchical microstructure and dual-nanoprecipitation, Mater. Today 2022;52: 90-101.

[103] F. Belelli, R. Casati, F. Larini, M. Riccio, M. Vedani, Investigation on two Ti-B-reinforced Al alloys for laser powder bed fusion, Mater. Sci. Eng. A 2021;808:140944.

[104] https://www.hrl.com/products-services/materials, Accessed on 15th Oct. 2022.

[105] AP Works, Material Data Sheet-Scalmalloy 2016.

[106] M. Bärtl, X. Xiao, J. Brillo, F. Palm, Influence of surface tension and evaporation on melt dynamics of aluminum alloys for laser powder bed fusion, J. Mater. Eng. Perform. 2022;31:6221-6233.

[107] D. Schimbäck, P. Mair, M. Bärtl, F. Palm, G. Leichtfried, S. Mayer, P.J. Uggowitzer, S. Pogatscher, Alloy design strategy for microstructural-tailored scandium-modified aluminum alloys for additive manufacturing, Scr. Mater. 2022;207: 114277.

[108] I. Rosenthal, R. Shneck, A. Stern, Heat treatment effect on the mechanical

properties and fracture mechanism in AlSi10Mg fabricated by additive manufacturing selective laser melting process, Mater. Sci. Eng. A 2018;729:310-322.

[109] C. Colombo, C. A. Biffi, J. Fiocchi, D. Scaccabarozzi, B. Saggin, A. Tuissi, L. M. Vergani, Modulating the damping capacity of L-PBF AlSi10Mg through stress-relieving thermal treatments, Theor. Appl. Fract. Mech. 2020;17:102537.

[110] J. H. Rao, Y. Zhang, K. Zhang, A. J. Huang, C. H. J. Davies, X. H. Wu, Multiple precipitation pathways in an Al-7Si-0.6Mg alloy fabricated by selective laser melting, Scr. Mater. 2019;160:66-69.

[111] X. P. Li, X. J. Wang, M. Saunders, A. Suvorova, L. C. Zhang, Y. J. Liu, M. H. Fang, Z. H. Huang, T. B. Sercombe, A selective laser melting and solution heat treatment refined Al-12Si alloy with a controllable ultrafine eutectic microstructure and 25% tensile ductility, Acta Mater. 2015;95:74-82.

[112] EOS GmbH−Electro Optical Systems Material Data Sheet: EDS Aluminium AlSi10Mg.

[113] J. Fiocchi, A. Tuissi, C. A. Biffi, Heat treatment of aluminum alloys produced by laser powder fusion: A review, Mater. Des. 2021;204:109651.

[114] T. H. Park, M. S. Baek, H. Hyer, Y. H. Sohn, K. A. Lee, Effect of direct aging on the microstructure and tensile properties of AlSi10Mg alloy manufactured by selective laser melting process, Mater. Charact. 2021;176:111113.

[115] H. Zhang, Y. Wang, J. J. Wang, D. R. Ni, D. Wang, B. L. Xiao, Z. Y. Ma, Achieving superior mechanical properties of selective laser melted AlSi10Mg via direct aging treatment, J. Mater. Sci. Technol. 2022;108:226-235.

[116] Z. H. Hu, Y. Qi, S. B. Gao, X. J. Nie, H. Zhang, H. H. Zhu, X. Y. Zeng, Aging response of an Al-Cu alloy fabricated by selective laser melting, Addit. Manuf. 2021;37: 101635.

[117] P. Wang, C. Gammer, F. Brenne, K. G. Prashanth, R. G. Mendes, M. H. Rümmeli, T. Gemming, J. Eckert, S. Scudino, Microstructure and mechanical properties of a heat-treatable Al-3.5Cu01.5Mg-1Si alloy produced by selective laser melting, Mater. Sci. Eng. A 2018;711:562-570.

[118] Y. Qi, H. Zhang, J. J. Zhu, X. J. Nie, Z. H. Hu, H. H. Zhu, X. Y. Zeng, Mechanical

behavior and microstructure evolution of Al–Cu–Mg alloy produced by laser powder bed fusion: Effect of heat treatment, Mater. Character. 2020;165:110364.

[119] M. Opprecht, G. Roux, J. P. Garandet, C. Flament, A study of the mechanical properties of Al6061-Zr1.2 alloy processed by laser beam melting, J. Mater. Eng. Perform. 2023;32:1840-1855.

[120] Y. F. Wang, X. Lin, N. Kang, Z. H. Wang, Y. X. Liu, W. D. Huang, Influence of post-heat treatment on the microstructure and mechanical properties of Al-Cu-Mg-Zr alloy manufactured by selective laser melting, J. Mater. Sci. Technol. 2022;111:35-48.

[121] Q. B. Jia, F. Zhang, P. Rometsch, J. W. Li, J. Mata, M. Weyland, L. Bourgeois, M. L. Sui, X. H. Wu, Precipitation kinetics, microstructure evolution and mechanical behavior of a developed Al-Mn-Sc alloy fabricated by selective laser melting, Acta Mater. 2020;193:239-251.

[122] Z. H. Qin, N. Kang, M. El Mansori, Z. H. Wang, H. X. Wang, X. Lin, J. Chen, W. D. Huang, Anisotropic high cycle fatigue property of Sc and Zr-modified Al-Mg alloy fabricated by laser powder bed fusion, Addit. Manuf. 2022; 49: 102514.

[123] G. W. Wang, D. Song, Z. K. Zhou, Y. Liu, N. N. Liang, Y. N. Wu, A. B. Ma, J. H. Jiang, Developing high-strength ultrafine-grained pure Al via large-pass ECAP and post-rolling, J. Mater. Res. Technol. 2021;15:2419-2428.

[124] G. Guiglionda, W. J. Poole, The role of damage on deformation and fracture in Al – Si eutectic alloys, Mater. Sci. Eng. A 2002:336:159-169.

[125] B. Chen, S. K. Moon, X. Yao, G. Bi, J. Shen, J. Umeda, K. Kondoh, Strength and strain hardening of a selective laser melted AlSi10Mg alloy, Scr. Mater. 2017;141:45-49.

[126] J. Suryawanshi, K. G. Prashanth, S. Scudino, J. Eckert, Om Prakash, U. Ramamurty, Simultaneous enhancements of strength and toughness in an Al-12Si alloy synthesized using selective laser melting, Acta Mater. 2016;115:285-294.

[127] H. Rao, S. Giet, K. Yang, X. H. Wu, C. H. J. Davies, The influences of processing parameters on aluminium alloy A357 manufactured by selective laser melting, Mater. Des. 2016;109:334-346.

[128] B. Zhang, W. Wei, W. Shi, Y. W. Guo, S. P. Wen, X. L. Wu, K. Y. Gao, L. Rong, H. Huang, Z. R. Nie, Effect of heat treatment on the microstructure and mechanical properties of Er-containing Al-7Si-0.6Mg alloy by laser powder bed fusion, J. Mater. Res. Technol. 2022;18:3073-3084.

[129] Z. H. Xiong, S. L. Liu, S. F. Li, Y. Shi, Y. F. Yang, R. D. K. Misra, Role of melt pool boundary condition in determining the mechanical properties of selective laser melting AlSi10Mg alloy, Mater. Sci. Eng. A 2019;740-741:148-156.

[130] S. Q. Chen, Q. Y. Tan, W. Q. Gao, G. L. Wu, J. M. Fan, Z. Q. Feng, T. L. Huang, A. W. Godfrey, M. X. Zhang, X. X. Huang, Effect of heat treatment on the anisotropy in mechanical properties of selective laser melted AlSi10Mg, Mater. Sci. Eng. A 2022;858:144130.

[131] S. Q. Chen, Q. Y. Tan, W. Q. Gao, G. L. Wu, J. M. Fan, Z. Q. Feng, T. L. Huang, A. W. Godfrey, M. X. Zhang, X. X. Huang, Effect of heat treatment on the anisotropy in mechanical properties of selective laser melted AlSi10Mg, Mater. Sci. Eng. A 2022; 858:144130.

[132] M. S. Baek, R. Kreethi, T. H. Park, Y. H. Sohn, K. A. Lee, Influence of heat treatment on the high-cycle fatigue properties and fatigue damage mechanism of selective laser melted AlSi10Mg alloy, Mater. Sci. Eng. A 2021;819:141486.

[133] Z. H. Hu, H. Zhang, H. H. Zhu, Z. X. Xiao, X. J. Nie, X. Y. Zeng, Microstructure, mechanical properties and strengthening mechanisms of AlCu5MnCdVA aluminum alloy fabricated by selective laser melting, Mater. Sci. Eng. A 2019;759:154-166.

[134] H. Zhang, H. H. Zhu, X. J. Nie, J. Yin, Z. H. Hu, X. Y. Zeng, Effect of Zirconium addition on crack, microstructure and mechanical behavior of selective laser melted Al-Cu-Mg alloy, Scr. Mater. 2017;134:6-10.

[135] Q. B. Jia, P. Rometsch, P. Kürnsteiner, Q. Chao, A. J. Huang, M. Weyland, L. Bourgeois, X. H. Wu, Selective laser melting of a high strength Al-Mn-Sc alloy: alloy design and strengthening mechanisms, Acta Mater. 2019;171:108-118.

[136] Z. H. Wang, X. Lin, J. F. Wang, N. Kang, Y. L. Hu, D. Q. Wang, H. Y. Li, W. D. Huang, F. S. Pan, Remarkable strength-impact toughness conflict in high-strength Al–

Mg–Sc–Zr alloy fabricated via laser powder bed fusion additive manufacturing, Addit. Manuf. 2022;59:103093.

[137] Y. C. Zhang, X. L. Yuan, S. H. Yuan, R. Sun, T. Sakai, M. I. Lashari, U. Hamid, W. Li, High-cycle-fatigue properties of selective-laser-melted ASi10Mg with multiple build directions, Int. J. Mech. Sci. 2022;224:107336.

[138] N. E. Uzan, R. Shneck, O. Yeheskel, N. Frage, Fatigue of AlSi10Mg specimens fabricated by additive manufacturing selective laser melting (AM-SLM), Mater. Sci. Eng. A 2017;704: 229-237.

[139] M. J. Paul, Q. Liu, J. P. Best, X. P. Li, J. Kruzic, U. Ramamurty, B. Gluovatz, Fracture toughness of AlSi10Mg fabricated by laser powder bed fusion, Acta Mater. 2021;211:116869.

[140] Z. H. Wang, X. Lin, N. Kang, Y. F. Wang, X. B. Yu, H. Tan, H. O. Yang, W. D. Huang, Making selective-laser-melted high-strength Al-Mg-Sc-Zr alloy tough via ultrafine and heterogeneous microstructure, Scr. Mater. 2021; 203:114502.

[141] R. Jones, J. Cizek, O. Kovarik, J. Lang, A. Ang, J. G. Michopoulos, Describing crack growth in additively manufactured Scalmalloy, Addit. Manuf. Lett. 2021;1:100020.

[142] P. D. He, R. F. Webster, V. Yakubov, H. Kong, Q. Yang, S. Huang, M. Ferry, J. J. Kruzic, X. P. Li, Fatigue and dynamic aging behavior of a high strength Al-5024 alloy fabricated by laser powder bed fusion additive manufacturing, Acta Mater. 2021;220:117312.

[143] R. L. Revilla, D. Verkens, G. Couturiaux, L. Malet, L. Thijs, S. Dodet, I. De Graeve, Galvanostatic anodizing of additive manufactured Al-Si10-Mg alloy, J. Electrochem. Soc. 2017;164:C1027.

[144] Y. Chen, J. X. Zhang, X. H. Gu, N. W. Dai, P. Qin, L. C. Zhang, Distinction of corrosion resistance of selective laser melted Al-12Si alloy on different planes, J. Alloys Compd. 2018;747:648-658.

[145] M. Cabrini, S. Lorenzi, T. Pastore, C. Testa, D. Manfredi, M. Lorusso, F. Calignano, M. Pavese, F. Andreatta, Corrosion behavior of AlSi10Mg alloy produced by laser powder bed fusion under chloride exposure, Corros. Sci. 2019;152:101-108.

[146] T. Rubben, R. I. Revilla, I. De Graeve, Influence of heat treatments on the corrosion mechanism of additive manufactured ASi10Mg, Corros. Sci. 2019;147: 406-415.

[147] L. C. Correa, L. G. Rovira, J. de D. López-Castro, F. J. Botana, Pitting and intergranular corrosion of Scalmalloy® aluminum alloy additively manufactured by selective laser melting (L-PBF), Corros. Sci. 2022;201:110273.

[148] D. D. Gu, H. Zhang, D. H. Dai, C. L. Ma, H. M. Zhang, Y. X. Li, S. H. Li, Anisotropic corrosion behavior of Sc and Zr modified Al-Mg alloy produced by selective laser melting, Corros. Sci. 2020;170:108567.

[149] O. Gharbi, D. Jiang, D. R. Feenstra, S. K. Kairy, Y. Wu, C. R. Hutchison, N. Birbilis, On the corrosion of additively manufactured aluminum alloy AA2024 prepared by selective laser melting, Corros. Sci. 2018;143:93-106.

[150] H. Zhang, D. D. Gu, D. H. Dai, C. L. Ma, Y. X. Li, M. Z. Cao, S. H. Li, Influence of heat treatment on corrosion behavior of rare earth element Sc modified Al-Mg alloy processed by selective laser melting, Appl. Surf. Sci. 2020;509:145330.

[151] L. Zhou, H. Hyer, J. F. Chang, A. Mehta, T. Huynh, Y. Yang, Y. H. Sohn, Microstructure, mechanical performance, and corrosion behavior of additively manufactured aluminum alloy 5083 with 0.7 and 1.0 wt% Zr addition, Mater. Sci. Eng. A 2021;823:141679.

[152] J. Bi, Z. L. Lei, Y. B. Chen, X. Chen,N. N. Lu, Z. Tian, X. K. Qin, An additively manufactured Al-14.1Mg-0.47Si-0.31Sc-0.17Zr alloy with high specific strength, good thermal stability and excellent corrosion resistance, J. Mater. Sci. Technol. 2021;67:23-35.

[153] H. Zhang, D. H. Dai, L. X. Xi, B. Gökce, D. D. Gu, An opposite tendency of mechanical properties and corrosion resistance of a high-strength Al-5024 alloy processed by laser powder bed fusion, J. Manuf. Sci. Eng. 2023;145: 031001.

[154] K. E. Knipling, D. C. Dunand, D. N. Seidman, Criteria for developing castable, creep-resistant aluminum-based alloys−A review, Inter. J. Mater. Res. 2006;97:246.

[155] R. A. Michi, A. Plotkowski, A. Shyam, R. R. Dehoff, S. S. Babu, Towards high-temperature applications of aluminum alloys enabled by additive manufacturing, Inter.

Mater. Rev. 2022;67:298-345.

[156] Polmear I, StJohn D, Nie J-F, et al. Light alloys: metallurgy of the light metals. Oxford: Butterworth-Heinemann; 2017.

[157] L. A. De, D. C. Dunand, D. N. Seidman, Scandium-enriched nanoprecipitates in aluminum providing enhanced coarsening and creep resistance. In: O. Martin, editor. Light Metals 2018, Basel: Springer International Publishing; 2018; P. 439-494.

[158] W. A. Baeslack, K. V. Jata, T. J. Lienert, Structure, properties and fracture of friction stir welds in a high-temperature Al-8.5Fe-1.3V-1.7Si alloy (AA-8009), J. Mater. Sci. 2006;41:2939-2951.

[159] H. B. Henderson, J. A. Hammons, A. A. Baker, S. K. McCall, T. T. Li, A. Perron, Z. C. Sims, R. T. Ott, F. Q. Meng, M. J. Thompson, D. Weiss, O. Rios, Enhanced thermal coarsening resistance in a nanostructured aluminum-cerium alloy produced by additive manufacturing, Mater. Des. 2021;209:109988.

[160] K. Sisco, A. Plotkowski, Y. Yang, D. Leonard, B. Stump, P. Nandwana, R. R. Dehoff, S. S. Babu, Microstructure and properties of additively manufactured Al-Ce-Mg alloys, Sci. Rep. 2021;11:6953.

[161] J. W. Deng, C. Chen, X. C. Liu, Y. P. Li, K. C. Zhou, S. M. Guo, A high-strength heat-resistant Al-5.7Ni eutectic alloy with spherical Al_3Ni nano-particles by selective laser melting, Scr. Mater. 2021;203:114304.

[162] A. Plotkowski, K. Sisco, S. Bahl, A. Shyam, Y. Yang, L. Allard, P. Nandwana, A. M. Rossy, R. R. Dehoff, Microstructure and properties of a high temperature Al-Ce-Mn alloy produced by additive manufacturing, Acta Mater. 2020;196:595-608.

[163] L. Zhou, T. Huynh, S. Park, H. Hyer, A. Mehta, S. T. Song, Y. L. Bai, B. McWilliams, K. Cho, Y. H. Sohn, Laser powder bed fusion of Al-10 wt% Ce alloys: microstructure and tensile property, J. Mater. Sci. 2020;55:14611-14625.

[164] D. R. Manca, A. Yu. Churyumov, A. V. Pozdniakov, A. S. Prosviryakov, D. K. Ryabov, A. Yu. Krokhin, V. A. Korolev, D. K. Daubarayte, Microstructure and properties of novel heat resistant Al-Ce-Cu alloy for additive manufacturing, Metals Mater. Inter. 2019;25:633-640.

[165] G. Rödler, F. G. Fischer, J. Preußner, V. Friedmann, C. Fischer, A. Weisheit, J. H.

Schleifenbaum, Additive manufacturing of high-strength eutectic aluminum-nickel alloys-processing and mechanical properties, J. Mater. Process. Technol. 2021;198:117315.

[166] S. Thapliyal, S. Shukla, L. Zhou, H. Hyer, P. Agrawal, P. Agrawal, M. Komarasamy, Y. H. Sohn, R. S. Mishra, Design of heterogeneous structured Al alloys with wide processing window for laser-powder bed fusion additive manufacturing, Addit. Manuf. 2021;42:102002.

[167] M. T. Pérez, A. Martin, D. F. Shi, S. Milenkovic, C. M. Cepeda-Jiménez, An Al-5Fe-6Cr alloy with outstanding high temperature mechanical behavior by laser powder bed fusion, Addit. Manuf. 2022;55:102828.

[168] T. Kimura, T. Nakamto, T. Ozaki, T. Miki, I. Murakami, Y. Hashizume, A. Tanaka, Microstructural development and aging behavior of Al-Cr-Zr heat-resistant alloy fabricated using laser powder bed fusion, J. Mater. Res. Technol. 2021;15:4193-4207.

[169] T. Kimura, T. Nakamoto, T. Ozaki, T. Miki, Microstructures and mechanical properties of aluminum-transition metal binary alloys (Al-Fe, Al-Mn, and Al-Cr) processed by laser powder bed fusion, J. Alloys Compd. 2021;872:159680.

[170] https://www.eckart.net/medias/sys_master/root/hf5/hb7/8930552086558/ECKART-A20X-POWDER.pdf, accessed on 19th. Oct. 2022.

[171] J. G. Kaufman,(Ed.), Properties of Aluminum alloys, ASM International, Washington, D. C. 1999.

[172] N. E. Uzan, R. Shneck, O. Yeheskel, N. Frage, High-temperature mechanical properties of AlSi10Mg specimens fabricated by additive manufacturing using selective laser melting technologies (AM-L-PBF), Addit. Manuf. 2018;24: 257-263.

[173] K. G. Prashanth, S. Scudino, J. Eckert, Tensile properties of Al-12Si fabricated via selective laser melting (L-PBF) at different temperatures, Technologies 2016;4:38.

[174] Y. Cao, X. Lin, Q. Z. Wang, S. Q. Shi, L. Ma, N. Kang, W. D. Huang, Microstructure evolution and mechanical properties at high temperature of selective laser melted AlSi10Mg, J. Mater. Sci. Eng. Technol. 2021;62:162-172.

[175] A. B. Spierings, K. Dawson, K. Kern, F. Palm, K. Wegener, L-PBF-processed Sc- and Zr- modified Al-Mg alloy: Mechanical properties and microstructural effects of

heat treatment, Mater. Sci. Eng. A 2017;701:264-273.

[176] S. Griffiths, J. R. Croteau, M. D. Rossell, R. Erni, A. De Luca, N. Q. Vo, D. C. Dunand, C. Leinenbach, Coarsening- and creep resistance of precipitation-strengthened Al-Mg-Zr alloys processed by selective laser melting, Acta Mater. 2020;188:192-202.

[177] E. Y. Gutmanas, Materials with fine microstructures by advanced powder metallurgy, Prog. Mater. Sci. 1990;34:261-266.

[178] H. Ding, Y. K. Xiao, Z. Y. Bian, Y. Wu, H. H. Yang, H. Z. Wang, H. W. Wang, Design, microstructure and thermal stability of a novel heat-resistant Al-Fe-Ni alloy manufactured by selective laser melting, J. Alloys Compd. 2021;885:160949.

[179] Z. C. Sims, D. Weiss, S. K. McCall, M A. McGuire, R. T. Ott, T. Geer, O. Rios, P. A. E. Turchi, Cerium-based, intermetallic-strengthened aluminum casting alloy: high-volume co-product development, JOM 2016;68:1940-1947.

[180] Z. C. Sims, O. R. Rios, D. Weiss, P. E. A. Turchi, A. Perron, J. R. I. Lee, T. T. Li, J. A. Hammons, M. B. Hansen, T. M. Willey, K. An, Y. Chen, A. H. King, S. K. McCall, High performance aluminum-cerium alloys for high-temperature applications, Mater. Horizons 2017;4:1070-1078.

[181] G. Boussinot, M. Döring, S. Hemes, O. Stryzhyboroda, M. Apel, M. Schmidt, Laser powder fusion of eutectic Al-Ni alloys: Experimental and phase-field studies, Mater. Des. 2021;198:109299.

[182] S. B. Sun, L. J. Zheng, Y. Y. Liu, J. H. Liu, H. Zhang, Characterization of Al-Fe-V-Si heat-resistant aluminum alloy components fabricated by selective laser melting, J. Mater. Res. 2015;30:1661-1669.

[183] M. A. Balbaa, A. Ghasemi, E. Fereiduni, M. A. Elbestawi, S. D. Jadhav, J. -P. Kruth, Role of powder particle size on laser powder bed fusion processability of AlSi10Mg alloy, Addit. Manuf. 2021;37:101630.

[184] R. Baitimerov, P. Lykov, D. Zherebtsov, L. Radionova, A. Shultc, K. G. Prashanth, Influence of powder characteristics on processability of AlSi12 alloy fabricated by selective laser melting, Materials 2018;11:742.

[185] K. Riener, N. Albrecht, S. Ziegelmeier, R. Ramakrishnan, L. Haferkamp, A. B. Spierings, G. J. Leichtfried, Influence of particle size and morphology on the properties

of the powder feedstock as well as of AlSi10Mg parts produced by laser powder bed fusion (L-PBF), Addit. Manuf. 2020;34:101286.

[186] X. P. Li, K M. O'Donnell, T. B. Sercombe, Selective laser melting of Al-12Si alloy: Enhanced densification via powder drying, Addit. Manuf. 2016;10:10-14.

[187] N. T. Aboulkhair, I. Maskery, I. Ashcroft, C. Tuck, N. M. Everitt, The role of powder properties on the processability of aluminum alloy in selective laser melting, 22nd World Photonics Confer. Lasers Manuf. Conf. 2015.

[188] K. V. Yang, P. Rometsch, T. Jarvis, J. Rao, S. Cao, C. Davies, X. H. Wu, Porosity formation mechanisms and fatigue response in Al–Si–Mg alloys made by selective laser melting, Mater. Sci. Eng. A 2018;712:166-174.

[189] A. Raza, T. Fegl, I. Hanif, A. Markstrom, M. Franke, C. Korner, E. Hryha, Degradation of AlSi10Mg powder during laser based powder bed fusion processing, Mater. Des. 2021;198:109358.

[190] P. Moghimian, T. Poirié, M. H. Korayem, J. A. Zavala, J. Kroeger, F. Marion, F. Larouche, Metal powders in additive manufacturing: A review on reusability and recyclability of common titanium, nickel and aluminum alloys, Addit. Manuf. 2021;43:102017.

[191] T. Fiegl, M. Franke, A. Raza, E. Hryha, C. Körner, Effect of AlSi10Mg0.4 long-term reused powder in PBF-LB/M on the mechanical properties, Mater. Des. 2021;212: 110176.

[192] T. Fiegl, M. Franke, C. Körner, Correlation of powder degradation, energy absorption and gas pore formation in laser-based powder bed fusion process of AlSi10Mg0.4, Addit. Manuf. 2022;56:102917.

[193] L. Cordova, T. Bor, M. de Smit, S. Carmignato, M. Campos, Effects of powder reuse on the microstructure and mechanical behavior of Al-Mg-Sc-Zr alloy processed by laser powder bed fusion (L-PBF), Addit. Manuf. 2020;36:101625.

[194] L. Cordova, M. Campos, T. Tinga, Revealing the effects of powder reuse for selective laser melting by powder characterization, JOM 2019;71:1062-1072.

[195] A. Ghasemi, E. Fereiduni, M. Balbaa, S. D. Jadhav, M. Elbestawi, S. Habibi, Influence of alloying elements on laser powder bed fusion processability of aluminum:

A new insight into the oxidation tendency, Addit. Manuf. 2021;46:102145.

[196] R. D. Li, M. B. Wang, T. C. Yuan, B. Song, C. Chen, K. C. Zhou, P. Cao, Selective laser melting of a novel Sc and Zr modified Al-6.2Mg alloy: Processing, microstructure, and properties, Powder Technol. 2017;319:117-128.

[197] M. Tang, P. C. Pistorius, Oxides, porosity and fatigue performance of AlSi10Mg parts produced by selective laser melting, Int. J. Fatigue 2017;94:192-201.

[198] Z. H. Hu, H. H. Zhu, X. J. Nie, C. C. Zhang, H. Zhang, X. Y. Zeng, On the role of atmospheric oxygen into mechanical properties and fracture behavior of selective laser melted AlCu5MnCdVA, Mater. Des. 2018;150:18-27.

[199] J. Yin, W. Q. Zhang, L. D. Ke, H. L. Wei, D. Z. Wang, L. L. Yang, H. H. Zhu, P. Dong, G. Q. Wang, X. Y. Zeng, Vaporization of alloying elements and explosion behviour during laser powder bed fusion of Cu-10Zn alloy, Int. J. Mach. Tool Manufact. 2021;161:103686.

[200] H. Zhao, T. DebRoy, Weld metal composition change during conduction mode laser welding of aluminum alloy 5182, Metall Mater. Trans. B 2001;32:163-172.

[201] A. P. Babu, S. K. Kairy, A. Huang, N. Birbilis, Laser powder bed fusion of high solute Al-Zn-Mg alloys: Processing, characterisation and properties, Mater. Des. 2020;196:109183.

[202] T. Qi, H. H. Zhu, J. Yin, B. J. Chen, Z. H. Hu, X. Y. Zeng, Porosity development and cracking behavior of Al-Zn-Mg-Cu alloys fabricated by selective laser melting, In: Solid freeform fabrication 2017.

[203] O. Gharbi, S. K. Kairy, P. R. De Lima, D. R. Jiang, J. Nicklaus, N. Birbilis, Microstructure and corrosion evolution of additively manufactured aluminum alloy AA7075 as a function of aging, NPJ Mater. Degrad. 2019;3:40.

[204] L. Zhou, H. Hyer, S. Thapliyal, R. S. Mishra, B. McWilliams, K. Cho, Y. Sohn, Process-dependent composition, microstructure, and printability of Al-Zn-Mg and Al-Zn-Mg-Sc-Zr manufactured by laser powder fusion, Metall. Mater. Trans. A 2020; 51: 3215-3227.

[205] H. Zhao, Y. Q. Chen, B. Gault, S. K. Makineni, D. Ponge, D. Raabe, $(Al,Zn)_3Zr$ dispersoids assisted η' precipitation in an Al-Zn-Mg-Cu alloy, Materialia 2020;10: 100641.

[206] D. D. Gu, W. Meiners, K. Wissenbach, R. Poprware, Laser additive manufacturing of metallic components: materials, processes and mechanisms, Int. Mater. Rev. 2013;57:133-164.

[207] Z. H. Wang, X. Lin, N. Kang, J. Chen, Y. Tang, H. Tan, X. B. Yu, H. O. Yang, W. D. Huang, Directed energy deposition additive manufacturing of a Sc/Zr-modified Al-Mg alloy: Effect of thermal history on microstructural evolution and mechanical properties, Mater. Sci. Eng. A 2021; 802: 140606.

[208] G. P. Dinda, A. K. Dasgupta, S. Bhattacharya, H. Natu, B. Dutta, J. Mazumder, Microstructural characterization of laser-deposited Al4047 alloy, Metall. Mater. Trans A 2012; 44 (5): 2233-2242.

[209] T. Gu, B. Chen, C. W. Tan, J. C. Feng, Microstructure evolution and mechanical properties of laser additive manufacturing of high strength Al-Cu-Mg alloy, Opt. Laser Technol. 2019; 112: 140-150.

[210] Q. Y. Pan, M. Kapoor, S. Mileski, J. Carsley, X. Y. Lou, Technical basis of using laser direct energy deposition as a high-throughput combinatorial method for DC-cast Al–Mn alloy development, Mater. Des. 2021;212:110290.

[211] D. Svetlizky, B. L. Zheng, T. L. Buta, Y. Z. Zhou, Oz Golan, U. Breiman, R. Haj-Ali, J. M. Schoenung, E. J. Lavernia, N. Eliaz, Directed energy deposition of Al5xxx alloy using laser engineered net shaping (LENS®), Mater. Des. 2020;192:108763.

[212] J. C. Li, X. Lin, N. Kang, J. L. Lu, Q. Z. Wang, W. D. Huang, Microstructure, tensile and wear properties of a novel graded Al matrix composite by direct energy deposition, J. Alloys Compd. 2020;826:154077.

[213] P. Kiani, A. D. Dupuy, K. K. Ma, J. M. Schoenung, Directed energy deposition of AlSi10Mg: Single track nonscalability and bulk properties, Mater. Des. 2020;194: 108847.

[214] M. Javidani, J. A. Zavala, J. Danovitch, Y. Tian, M. Brochu, Additive manufacturing of AlSi10Mg alloy using direct energy deposition: Microstructure and

hardness characterization, J. Therm. Spray Tech. 2017;26:587-597.

[215] K. Zygula, B. Nosek, H. Pasiowiec, N. Szysiak, Mechanical properties and microstructure of AlSi10Mg alloy fabricated by casting and SLM technique, World Scientific News 2018;104:462-472.

[216] A. Singh, A. Ramakrishnan, G. P. Dinda, Direct laser metal deposition of eutectic Al–Si alloy for automotive applications, TMS 146th Annual Meeting & Exhibition Supplemental Proceedings 2017:71-80.

[217] Z. H. Wang, X. Lin, N. Kang, Y. L. Hu, J. Chen, W. D. Huang, Strength-ductility synergy of selective laser melted Al-Mg-Sc-Zr alloy with a heterogeneous structure, Addit. Manuf. 2020;34:101260.

[218] B. A. Fulcher, D. A. Leigh, T. J. Watt, Comparison of AlSi10Mg and Al6061 processed through DMLS, in: Proceedings of the Solid Freeform (SFF) Symposium, Austin, TX, USA, 2014.

[219] A. Bhagavatam, A. Ramakrishnan, C. Adapa, G. P. Dinda, Laser metal deposition of aluminum 7075 alloy, Int. J. Mater. Sci. Res. 2018;1:50-55.

[220] A. Singh, A. Ramakrishnan, G. Dinda, Direct laser metal deposition of Al7050 alloy, SAE Technical Paper 2017-01-0286.

[221] S. B. Sun, L. J. Zheng, H. Peng, H. Zhang, Microstructure and mechanical properties of Al-Fe-V-Si aluminum alloy fabricated produced by electron beam melting, Mater. Sci. Eng. A 2016;659:207-214.

[222] H. K. Bian. K. Aoyagi, Y. F. Zhao, C. Maeda, T. Mouri, A. Chiba, Microstructure refinement for superior ductility of Al‑Si alloy by electron beam melting, Addit. Manuf. 2020;32:100982.

[223] M. S. Kenevisi, F. Lin, Selective electron beam melting of high strength Al2024 alloy: microstructural characterization and mechanical properties, J. Alloys Compd. 2020;843:155866.

[224] T. Mahale, D. Cormier, O. Harrysson, K. Ervin, Advances in electron beam melting of aluminum alloys, 18th Solid Free Fabr. Symp. SFF 2007; 2007:312.

[225] M. S. Kenevisi, F. Lin, Dissolution of Al_2Cu precipitate in Al2024 additively manufactured by electron beam melting, Adv. Eng. Mater. 2021;23:2100323.

[226] Y. F. Yu, M. S. Kenevisi, W. T. Yan, F. Lin, Modeling precipitation process of Al-Cu alloy in electron beam selective melting with a 3D cellular automaton model, Addit. Manuf. 2020;36:101423.

[227] V. R. Utyaganova, N. N. Shamarin, A. A. Eliseev, Electrochemical impedance study of corrosion properties of AA535 3D-printed by electron beam melting, AIP Conf. Proc. 2019;2167:020379.

[228] T. A. Rodrigues, V. R. Duarte, D. Tomás, J. A. Avila, J. D. Escobar, E. Rossinyol, N. Schell, T. G. Santos, J. P. Oliveira, In-situ strengthening of a high strength low alloy steel during wire and arc additive manufacturing (WAAM), Addit. Manuf. 2020;34: 101200.

[229] X. F. Xu, J. L. Ding, S. Ganguly, S. Williams, Investigation of process factors affecting mechanical properties of INCONEL 718 superalloy in wire + arc additive manufacture process, J. Mater. Process. Technol. 2019;265: 201-209.

[230] F. D. Wang, S. Williams, P. Colegrove, A. A. Antonysamy, Microstructure and mechanical properties of wire and arc additive manufactured Ti-6Al-4V, Metall. Mater. Trans. 2013;44:968-977.

[231] B. O. Omiyale, T. O. Olugbade, T. E. Abioye, P. K. Farayibi, Wire arc additive manufacturing of aluminum alloys for aerospace and automotive applications: a review, Mater. Sci. Technol. 2022;38:391-408.

[232] B. Q. Cong, R. J. Ouyang, B. J. Qi, J. L. Ding, Influence of cold metal transfer process and its heat input on weld bead geometry and porosity of aluminum-copper alloy welds, Rare Metal Mater. Eng. 2016;45:0606-0611.

[233] J. G. Pan, B. Yuan, J. G.Ge, Y. Ren, H. J. Chen, L. Zhang, H. Lu, Influence of arc mode on the microstructure and mechanical properties of 5356 aluminum alloy fabricated by wire arc additive manufacturing, J. Mater. Res. Technol. 2022;20:1893-1907.

[234] Y. L. Guo, Q. F. Han, W. J. Lu, F. C. An, J. L. Hu, Y. Y. Yan, C. M. Liu, Microstructure tuning enables synergistic improvements in strength and ductility of wire-arc additive manufactured commercial Al–Zn–Mg–Cu alloys, Virtual Phys. Prototyp. 2022;17:649-661.

[235] Z. N. Wang, X. Lin, L.L. Wang, Y. Cao, Y. H. Zhou, W. D. Huang, Microstructure evolution and mechanical properties of the wire + arc additive manufacturing Al–Cu alloy, Addit. Manuf. 2021;47:102298.

[236] Y. H. Zhou, X. Lin, N. Kang, T. Yang, W. D. Huang, Z. N. Wang, The heterogeneous band microstructure and mechanical performance in a wire+arc additively manufactured 2219Al alloy, Addit. Manuf. 2022;49:102486.

[237] L. W. Wang, T. Wu, A. P. Liu, H. Yan, Y. N. Mao, Y. Liu, Z. Z. Peng, D. L. Wang, Z. M. Liang, Q. Wang, G. Yang, B. Narayanaswamy, Effect of Al–5Ti–1B grain refiner on microstructure and properties of arc-additive-manufactured Al–Mg alloy, Vacuum 2022;200:111012.

[238] G. Doumenc, L. Couturier, B. Courant, P. Paillard, A. Benoit, E. Gautron, B. Girault, T. Pirling, S. Cabeza, D. Gloaguen, Investigation of microstructure, hardness and residual stresses of wire and arc additive manufactured 6061 aluminium alloy, Materialia 2022;25: 101520.

[239] X. P. Guo, H. J. Li, Z. X. Pan, S. Y. Zhou, Microstructure and mechanical properties of ultra-high strength Al-Zn-Mg-Cu-Sc aluminum alloy fabricated by wire + arc additive manufacturing, J. Manuf. Process. 2022;79: 576-586.

[240] X.P. Guo, H. J. Li, P. Xue, Z. X. Pan, R. Z. Xu, D. R. Ni, Z. Y. Ma, Microstructure and mechanical properties of 600 MPa grade ultra-high strength aluminum alloy fabricated by wire-arc additive manufacturing, J. Mater. Sci. Technol. 2023;149:56-66.

[241] R. Fu, W. J. Lu, Y. L. Guo, H. S. Lei, Y. N. Cui, J. R. Wang, D. Gao, J. C. Wang, C. M. Liu, Achieving high strength-ductility of Al-Zn-Mg-Cu alloys via hot-wire arc additive manufacturing enabled by strengthening precipitates, Addit. Manuf. 2022;58:103402.

[242] X. L. Ren, X. Q. Jiang, T. Yuan, X. H. Zhao, S. J. Chen, Microstructure and properties research of Al-Zn-Mg-Cu alloy with high strength and high elongation fabricated by wire arc additive manufacturing, J. Mater. Process. Technol. 2022;307:117665.

[243] T. Yuan, X. L. Ren, S. J. Chen, X. Q. Jiang, Grain refinement and property improvements of Al-Zn-Mg-Cu alloy by heterogeneous particle addition during wire

and arc additive manufacturing, J. Mater. Res. Technol. 2022;16:824-839.

[244] X. W. Fang, L. J. Zhang, G. P. Chen, K. Huang, F. Xue, L. Wang, J. Y. Zhao, B. H. Lu, Microstructure evolution of wire-arc additively manufactured 2319 aluminum alloy with interlayer hammering, Mater. Sci. Eng. A 2021;800:140168.

[245] S. Y. Zhou, J. Y. Wang, G. Yang, B. Wu, H. Xie, K. Wu, and D. An, Periodic microstructure of Al–Mg alloy fabricated by inter-layer hammering hybrid wire arc additive manufacturing: Formation mechanism, microstructural and mechanical characterization, Mater. Sci. Eng. A 2022;860:144314.

[246] C. Menpae, G. Cipolloni, M. Hebda, G. Ischia, Spark plasma sintering behaviour of copper powders having different particle sizes and oxygen contents, Powder Technol. 2016;291:170-177.

[247] https://www.exone.com/enUS/Resources/News/ExOne_Abbott_Binder_Jet_Continuous_Furance, Accessed on 15th Oct. 2022.

[248] B. J. Phillips, D. Z. Avery, T. Liu, O. L. Rodriguez, C. J. T. Mason, J. B. Jordon, L. N. Brewer, P. G. Allison, Microstructure-deformation relationship of additive friction stir-deposition Al-Mg-Si, Materialia 2019;7:100387.

[249] O. G. Rivera, P. G. Allison, L. N. Brewer, O. L. Rodriguez, J. B. Jordon, T. Liu, W. R. Whittington, R. L. Martens, Z. McClelland, C. J. T. Mason, L. Garcia, J. Q. Su, N. Hardwick, Influence of texture and grain refinement on the mechanical behavior of AA2219 fabricated by high shear solid state material deposition, Mater. Sci. Eng. A 2018;724:547-558.

[250] R. S. Mishra, R. S. Haridas, P. Agrawal, Friction stir-based additive manufacturing, Sci. Technol. Weld Joi. 2022;27:141-165.

[251] J. B. Jordon, P. G. Allison, B. J. Phillips, D. Z. Avery, R. P. Kinser, L. N. Brewer, C. Cox, K. Doherty, Direct recycling of machine chips through a novel solid-state additive manufacturing process, Mater. Des. 2020;193:108850.

[252] J. K. Yoder, R. J. Griffiths, H. Z. Yu, Deformation-based additive manufacturing of 7075 aluminum alloy with wrought-like mechanical properties, Mater. Des. 2021; 198:109288.

[253] D. Z. Avery, B. J. Phillips, C. J. T. Mason, M. Palermo, M. B. Williams, C. Cleek,

O. L. Rodriguez, P. G. Allison, J. B. Jordon, Influence of grain refinement and microstructure on fatigue behavior for solid-state additively manufactured Al-Zn-Mg-Cu alloy, Metall. Mater. Trans. A 2020;51A:2778-2795.

[254] Y. Ding, J. A. Muniz-Lerma, M. Trask, S. Chou, A. Walker, M. Brochu, Microstructure and mechanical property considerations in additive manufacturing of aluminum alloys, MRS Bull 2016;41:745-751.

[255] M. K. Surappa, Aluminium matrix composites: challenges and opportunities, Sadhana 2003;28:319-334.

[256] R. Xu, R. D. Li, T. C. Yuan, H. B. Zhu, P. Li, Microstructure and mechanical properties of TiC-reinforced Al-Mg-Sc-Zr composites additively manufactured by laser direct energy deposition, Acta Metall. Sinica. 2022;35:411-424.

[257] L. X. Li, H. Zhang, P. Wang, H. C. Li, K. G. Prashanth, K. J. Lin, I. Kaban, D. D. Gu, Comparative investigation of microstructure, mechanical properties and strengthening mechanisms of Al-12Si/TiB2 fabricated by selective laser melting and hot pressing, Ceram. Inter. 2018;44:17635-17642.

[258] B. Chen, X. Xi, T. Gu, C. W. Tan, X. G. Song, Influence of heat treatment on microstructure evolution and mechanical properties of TiB_2/Al2024 composites fabricated by directed energy deposition, J. Mater. Res. Technol. 2020;9:14223-14236.

[259] J. H. Wang, T. Liu, L. S. Luo, X. Y. Cai, B. B. Wang, H. H. Zhao, Z. H. Cheng, L. Wang, Y. Q. Su, X. Xue, J. J. Guo, Selective laser melting of high-strength TiB_2/AlMgScZr composites: microstructure, tensile deformation behavior, and mechanical properties, J. Mater. Res. Technol. 2022;16:786-800.

[260] D. H. Dai, D. D. Gu, Tailoring surface quality through mass and momentum transfer modeling using a volume of fluid method in selective laser melting of TiC/AlSi10Mg powder, Int. J. Mach. Tool Manufact. 2015;88:95-107.

[261] D. D. Gu, H. Q. Wang, D. H. Dai, P. P. Yuan, W. Meiners, R. Poprawe, Rapid solidification of Al-based bulk-form nanocomposites with novel reinforcement and enhanced performance by selective laser melting, Scr. Mater. 2015;96:25-28.

[262] T. Q. Zheng, S. H. Pan, N. Murali, B. B. Li, X. C. Li, Selective laser melting of novel 7075 aluminum powders with internally dispersed TiC nanoparticles, Mater. Lett.

2022;319: 132268.

[263] X. W. Li, S. Shi, S. Han, X. G. Hu, Q. Zhu, H. X. Lu, W. W. Li, Y. S. Shi, H. Ding, Microstructure, solidification behavior and mechanical properties of Al-Si-Mg-Ti/TiC fabricated by selective laser melting, Addit. Manuf. 2020;34:101326.

[264] W. Cheng, Y. Z. Liu, X. J. Xiao, B. Huang, Z. G. Zhou, X. H. Liu, Microstructure and mechanical properties of a novel (TiB_2 + TiC)/AlSi10Mg composite prepared by selective laser melting, Mater. Sci. Eng. A 2022;834:142435.

[265] F. Chang, D. D. Gu, D. H. Dai, P. P. Yuan, Selective laser melting of in-situ Al_4SiC_4 + SiC hybrid reinforced Al matrix composites: Influence of starting SiC particle size, Surf. Coat. Technol. 2015;272:15-24.

[266] X. Zhao, B. Song, W. R. Fan, Y. J. Zhang, Y. S. Shi, Selective laser melting of carbon/AlSi10Mg composites: microstructure, mechanical and electronical properties, J. Alloys Compd. 2016;665:271-281.

[267] Q. Y. Tan, J. Zhang, N. Mo, Z. Fan, Y. Yin, M. Bermingham, Y. Liu, H. Huang, M. X. Zhang, A novel method to 3D-print fine-grained AlSi10Mg alloy with isotropic properties via inoculation with LaB_6 nanoparticles, Addit. Manuf. 2020;32: 101034.

[268] T. Gao, S. Y. Zhang, G. L. Liu, Q. Q. Sun, Z. C. Wang, X. F. Liu, X. B. Wang, A high-strength AlSi10Mg alloy fabricated by laser powder fusion with addition of Al-Ti-C-B master alloy powders, Materialia 2021;16:101103.

[269] D. Y. Zhang, D. H. Yi, X. P. Wu, Z. Y. Liu, W. D. Wang, R. Poprawe, J. H. Schleifenbaumc, S. Zieglerd, SiC reinforced AlSi10Mg composites fabricated by selective laser melting, J. Alloys Compd. 2021;162365.

[270] L. B. Li, T. C. Yuan, X. X. Yuan, The microstructure tailoring and property improving of directed energy deposited Al-Zn-Mg-Cu alloy modified with various Si and ZrO_2 contents, Mater. Character. 2022;188: 111896.

[271] L. X. Li, K. Ding, H. Zhang, D. D. Gu, In-situ synthesis of aluminum matrix nanocomposites by selective laser melting of carbon nanotubes modified Al-Mg-Sc-Zr alloys, J. Alloys Compd. 2021;891:162047.

[272] L. Y. Jiang, T. T. Liu, C. D. Zhang, M. C. Li, T. Ma, W. H. Liao, Preparation and mechanical properties of CNTs-AlSi10Mg composite fabricated via selective laser

melting, Mater. Sci. Eng. A 2018;734: 171-177.

[273] W. J. Wu, C. F. Gao, Z. Q. Liu, K. H. Wong, Z. Y. Xiao, Laser powder bed fusion of crack-free TiN/Al7075 composites with enhanced mechanical properties, Mater. Lett. 2021;282:128625.

[274] G. Li, Y. H. Huang, X. W. Li, C. Guo, Q. Zhu, J. Lu, Laser powder bed fusion of nano-titania modified 2219 aluminium alloy with superior mechanical properties at both room and elevated temperatures: The significant impact of dilute, Addit. Manuf. 2022;60:103296.

[275] S. Y. Zhou, Y. Su, H. Wang, J. Enz, T. Ebel, M. Yan, Selective laser melting additive manufacturing of 7xxx series Al-Zn-Mg-Cu alloy: cracking elimination by co-incorporation of Si and TiB_2, Addit. Manuf. 2020;36:101458.

[276] Y. K. Xiao, Z. Y. Bian, Y. Wu, G. Ji, Y. Q. Li, M. J. Li, Q. Lian, Z. Chen, A. Addad, H. W. Wang, Effect of nano-TiB_2 particles on the anisotropy in an AlSi10Mg alloy processed by selective laser melting, J. Alloys Compd. 2019;798:644-655.

[277] P. P. Yuan, D. D. Gu, D. H. Dai, Particulate migration behavior and its mechanism during selective laser melting of TiC reinforced Al matrix nanocomposites, Mater. Des. 2015;82:46-55.

[278] W. E. King, A. T. Anderson, R. M. Ferecz, N. E. Hodge, C. Kamath, S. A. Khairallah, Overview of modelling and simulation of metal powder bed fusion process at Lawrence Livermore National Laboratory, Mater. Sci. Technol. 2015;31:957-968.

[279] T. T. Sun, H. Z. Wang, Z. Y. Gao, Y. Wu, M. L. Wang, X. Y. Jin, C. L. Alex Lung, P. D. Lee, Y. N. Fu, H. W. Wang, The role of in-situ Nano-TiB_2 particles in improving the printability of noncastable 2024Al alloy, Mater. Res. Lett. 2022;10:656-665.

[280] Q. Z. Wang, X. Li, N. Kang, X. L. Wen, Y. Cao, J. L. Lu, D. J. Peng, J. Bai, Y. X. Zohu, M. EI Mansori, W. D. Huang, Effect of laser additive manufacturing on the microstructure and mechanical properties of TiB_2 reinforced Al-Cu matrix composite, Mater. Sci. Eng. A 2022;840: 142950.

[281] S. Zhu, S. Q. Song, Y. Chen, F. Zhao, W. X. Yang, Z. W. Li, Y. S. Shi, S. F. Yu, Effect of in-situ Al2O3 on tensile strength and ductility of AlSi10Mg alloy fabricated by selective laser melting, Mater. Lett. 2022;308A:131108.

[282] Y. K. Xiao, H. Chen, Z. Y. Bian, T. T. Sun, H. Ding, Q. Yang, Y. Wu, Q. Lian, Z. Chen, H. W. Wang, Enhancing strength and ductility of AlSi10Mg fabricated by selective laser melting by TiB_2 nanoparticles, J. Mater. Sci. Technol. 2022;109:254-266.

[283] X. H. Liu, Y. Z. Liu, Z. G. Zhou, K. D. Wang, Q. K. Zhan, X. J. Xiao, Grain refinement and crack inhibition of selective laser melted AA2024 aluminum alloy via inoculation with TiC-TiH_2, Mater. Sci. Eng. A 2021;813:141171.

[284] https://www.elementum3d.com/wp-content/uploads/2022/01/A1000-RAM10-Data-Sheets-2021-04-16.pdf, accessed on 26th. Sep. 2022.

[285] https://www.elementum3d.com/wp-content/uploads/2022/01/A2024-RAM2-Data-Sheets-2021-04-19.pdf, accessed on 19th. Oct. 2022.

[286] https://www.elementum3d.com/wp-content/uploads/2022/01/A2024-RAM10-Data-Sheets-2021-04-02.pdf, accessed on 19th. Oct. 2022.

[287] https://www.elementum3d.com/wp-content/uploads/2022/07/A6061-RAM2-Web-Data-Sheets-2022-07-26-2.pdf, accessed on 10th Sep. 2022.

[288] https://www.elementum3d.com/wp-content/uploads/2022/01/A7050-RAM2-Data-Sheets-2021-04-15.pdf, accessed on 24th Oct. 2022.

[289] https://www.elementum3d.com/wp-content/uploads/2022/05/A7075-RAM2-Data-Sheets-2021-04-15.pdf, accessed on 18th Jan. 2023.

[290] S. M. Ma, Y. Li, W. B. Kan, J. L. Zhang, M. L. Wang, L. Wang, Y. Wu, H. W. Wang, Z. Chen, Enhancement of grain refinement and heat resistance in TiB_2-reinforced Al-Cu-Mg-Fe-Ni matrix composite additive manufactured by electron beam melting, J. Alloys Compd. 2022;924:166395.

[291] X. L. Wen, Q. Z. Wang, Q. Mu, N. Kang, S. Sui, H. O. Yang, X. Lin, W. D. Huang, Laser solid forming additive manufacturing TiB_2 reinforced 2024Al composite: Microstructure and mechanical properties, Mater. Sci. Eng. A 2019;745:319-325.

[292] P. Jie, Y. B. Liu, F. X. Li, Q. J. Sun, Realization of synergistic enhancement for fracture strength and ductility by adding TiC particles in wire and arc additive manufacturing 2219 aluminum alloy, Compos. B. Eng. 2021;219:108921.

[293] G. Langelandsvik, O. Ragnvaldsen, J. E. Flam, O. M. Akselsen, H. J. Roven, Wire and arc additive manufacturing with TiC-nanoparticle reinforced AA5183 alloy,

MATEC Web of Conference 2020;326:07002.

[294] S. Q. Yan, L. Chen, A. Yob, D. Renshaw, K. Yang, M. Givord, D. Liang, Multifunctional metal matrix composites by friction stir additive manufacturing, J. Mater. Eng. Perform. 2022;31:6183-6195.

[295] M. M. EI-Sayed Seleman, S. Ataya, M. M. Z. Ahmed, A. M. M. Hassan, F. H. Latief, K. Hajiaoui, A. E. Ei-Nikhaily, M. I. A. Habba, The additive manufacturing of aluminum matrix nano Al_2O_3 composites produced via friction stir deposition using different initial material conditions, Materials 2022;15:2926.

[296] H. B. Xie, J. L. Zhang, F. L. Li, G. Q. Yuan, Q. Zhu, Q. L. Jia, H. J. Zhang, S. W. Zhang, Selective laser melting of SiCp/Al composites: Densification, microstructure, and mechanical and tribological properties, Ceramics Inter. 2021;47:30826-30837.

[297] H L. Liao, H. H. Zhu, G. Xue, X. Y. Zeng, Alumina loss mechanism of Al_2O_3-AlSi10Mg composites during selective laser melting, J. Alloys Compd. 2019;785:186-295.

[298] https://www.elementum3d.com/wp-content/uploads/2022/01/A1000-AM-Data-Sheets-2021-04-15.pdf, accessed on 25th. Sep. 2022.

[299] https://www.3dsystems.com/materials/aluminium-alloy-alsi12, accessed on 24th Oct. 2022.

[300] https://www.eos.info/en/additive-manufacturing/3d-printing-metal/dmls-metal-materials/aluminium-al, accessed on 24th Oct. 2022.

[301] https://www.slm-solutions.com/fileadmin/Content/Powder/MDS/MDS_Al-Alloy_AlSi9Cu3_0219_EN.pdf, accessed on 19th. Apr. 2023.

[302] https://www.eos.info/03_system-related-assets/material-related-contents/metal-materials-and-examples/metal-materialdatasheet/aluminium/material_datasheet_eos_aluminium_al2139-am_02-23_en.pdf, accessed on 19th. Apr. 2023.

[303] https://www.apworks.de/scalmalloy, accessed on 24th Oct. 2022.

[304] https://www.metals4printing.com/wp-content/uploads/datasheets/eng/Al-Base/m4p_Datasheet_StrengthAl_EN.pdf, accessed on 10th Sep. 2022.

[305] https://www.metal-am.com/articles/additive-manufacturing-of-aluminium-parts-

by-directed-energy-deposition-possibilities-and-challenges/, accessed on 12th Oct. 2022.

[306] https://www.3dprintingmedia.network/airbus-receives-federal-ecodesign-award-pioneering-3d-printed-partition/, accessed on 17th June 2022.

[307] https://www.eos.info/01_partsandapplications/case_studies_applications_parts/_case_studies_pdf/ en_cases/cs_m_aerospace_ruag_en.pdf, accessed 10th Sep. 2022.

[308] https://3dprintingindustry.com/news/STELIA Aerospace use WAAM build an airplane fuselage-3D Printing Industry, accessed on 27th, Mar. 2023

[309] https://www.3dprintingmedia.network/mercedes-benz-trucks-introduces-first-ever-metal-3d-printed-spare-parts/, accessed on 17th June 2022.

[310] https://www.3dprintingmedia.network/bmw-starts-lean-series-production-bmw-i8-roadster-metal-3d-printed-parts/, accessed on 17th Jun 2022.

[311] https://www.3dprintingmedia.network/aluminum-3d-printed-blades-push-chinese-speed-skating-athletes-to-two-medals/, accessed on 17th Jun 2022.

[312] https://3dprintingindustry.com/news/optomec-advances-aluminum-directed-energy-deposition-ded-additive-manufacturing-171579/, Accessed on 15th Oct. 2022.

[313] Y. X. Du, D. D. Gu, L. X. Xi, D. H. Dai, T. Gao, J. H. Zhu, C. L. Ma, Laser additive manufacturing of bio-inspired lattice structure: forming quality, microstructure and energy absorption behavior, Mater. Sci. Eng. A 2020;773:138857.

[314] K. K. Wong, K. C. Leong, Saturated pool boiling enhancement using porous lattice structures produced by selective laser melting, Int. J. Heat Mass Trans. 2018;121: 46-63.

[315] J. Broughton, Y. K. Joshi, Comparison of single-phase convection in additive manufactured versus traditional metal foams, J. Heat Transfer. 2020;142:082201.

[316] J. Q. Gong, K. W. Wei, M. N. Liu, W. J. Song, X. Y. Li, X. Y. Zeng, Microstructure and mechanical properties of AlSi10Mg alloy built by laser powder bed fusion/direct energy deposition hybrid laser additive manufacturing, Addit. Manuf. 2022;59:103160.

[317] M. S. Pham, C. Liu, I. Todd, J. Lertthanasarn, Damage-tolerant architecture materials inspired by crystal microstructure, Nature 2019;565:305-311.

[318] U. Gebhardt, T. Gustmann, L. Giebeler, F. Hirsch, J. K. Hufenbach, M. Kästner,

Additively manufactured AlSi10Mg lattices–Potential and limits of modelling as-designed structures, Mater. Des. 2022;220:110796.

[319] D. C. Hofmann, S. Roberts, R. Otis, J. Kolodziejska, R. P. Dillon, K. O. Suh., A. A. Shapiro, Z. K. Liu, J. P. Borgonia, Developing gradient metal alloys through radial deposition additive manufacturing, Sci. Rep. 2014;4: 5357.

[320] E. Cerri, E. Ghio, G. Bolelli, Effect of the distance from build platform and post-heat treatment of AlSi10Mg alloy manufactured by single and multi-laser selective laser melting, J. Mater. Eng. Perform. 2021;30:4981-4992.

[321] D. F. Du, L. Wang, A. P. Dong, W. T. Yan, G. L. Zhu, B. D. Sun, Promoting the densification and grain refinement with assistance of static magnetic field in laser powder bed fusion, Int. J. Mach. Tool Manufact. 2022;183:103965.

[322] C. L. Tan, R. S. Li, J. L. Su, D. F. Du, Y. Du, B. Attard, Y. X. Chew, H. O. Zhang, E. J. Lavernia, Y. Fautrelle, J. Teng, A. P. Dong, Review on field assisted metal additive manufacturing, Int. J. Mach. Tool Manufact. 2023;189:104032.

[323] B. Aydogan, A. O'Neil, H. Sahasrabudhe, Microstructural and mechanical characterization of stainless steel 420 and Inconel 718 multi-material structures fabricated using laser directed energy deposition, J. Manuf. Proc. 2021;68:1224-1235.

[324] M. Ansari, E. Jabari, E. Toyserkani, Opportunities and challenges in additive manufacturing of functionally graded metallic materials via powder-fed laser directed energy deposition: A review, J. Mater. Technol. 2021;294:117117.

[325] D. C. Hofmann, S. Roberts, R. Otis, J. Kolodziejska, R. P. Dillon, R. P. Suh, A. A. Shapiro, Z. K. Liu, J. P. Borgonia, Developing gradient metal alloys through radial deposition additive manufacturing, Sci. Rep. 2014;4:5357.

[326] P. Moghimian, T. Poirié, M. H. Korayem, J. A. Zavala, J. Kroeger, F. Marion, F. Larouche, Metal powders in additive manufacturing: A review on reusability and recyclability of common titanium, nickel and aluminum alloys, Addit. Manuf. 2021;43: 102017.

[327] T. Ullsperger, D. M. Liu, B. Yürekli, G. Mattäus, L. Schade, B. Seyfarth, H. Kohl, R. Ramm, M. Rettenmayr, S. Nolte, Ultra-short pulsed laser powder bed fusion of Al‐Si alloys: Impact of pulse duration and energy in comparison to continuous wave

excitation, Addit. Manuf. 2021;46:102085.

[328] J. L. Lu, X. Lin, N. Kang, Y. Cao, Q. Z. Wang, W. D. Huang, Keyhole mode induced simultaneous improvement in strength and ductility of Sc modified Al-Mn alloy manufactured by selective laser melting, Mater. Sci. Eng. A 2021;811: 141089.

[329] Z. Q. Wang, Z. Z. Zhang, K. Demir, G. X. Gu, Machine learning for advanced additive manufacturing, Matter 2020;3:1541-1556.

[330] W. Xu, M. Brandt, S. Sun, J. Elambasseril, Q. Liu, K. Latham, K. Xia, M. Qian, Additive manufacturing of strong and ductile Ti-6Al-4V by selective laser melting via in situ martensite decomposition, Acta Mater. 2015;85:74-84.

[331] S. B. Gao, Z. H. Hu, M. Duchamp, P. S. R. Krishnan, S. Tekumalla, X. Song, M. Seita, Recrystallization-based grain boundary engineering of 316L stainless steel produced via selective laser melting, Acta Mater. 2020;200:366-377.

[332] C. Pauzon, M. Buttard, A. Després, B. Chehab, J. J. Blandin, G. Martin, A novel laser powder bed fusion Al-Fe-Zr for superior strength-conductivity trade-off, Scr. Mater. 2022;219:114878.